

UNIVERSITÀ DEGLI STUDI DI NAPOLI FEDERICO II



FACOLTA' DI INGEGNERIA

Dipartimento di Ingegneria dei Materiali e della Produzione

**TESI DI DOTTORATO IN INGEGNERIA DEI MATERIALI
E DELLE STRUTTURE (XXIV CICLO)**

**“MULTISCALE AND MULTIPHYSIC FEM BASED
NUMERICAL APPROACHES IN MECHANICS OF
COMPOSITE MATERIALS”**

TUTOR

Ch.mo Prof. Giuseppe Mensitieri

Ch.mo Prof. Massimiliano Fraldi

CANDIDATO

Arsenio Cutolo

Preface

Composite materials are ideal for structural application where high strength-to-weight and stiffness-to-weight ratio are needed. Most of modern technologies require material offering peculiar combinations of several properties that cannot be found in traditional materials as metals, ceramics and polymers.

The study of composite material actually involves many topics, such as manufacturing processes, non linearity constitutive behavior, strength of materials and micromechanics. The progress in technologies has allowed the development of analytical and numerical procedures that are nowadays essential to characterize the behavior of materials. This work addresses several finite element approaches that have been adopted to simulate the behavior of several composite structures.

In particular, in the first chapter, the anisotropic constitutive behavior of ALCANTARA[®] tissue is modeled introducing both linear anisotropic laws and non-linear hyperelastic model, the latter by the definition of Helmholtz free energy and set up specific microstructure tensor.

The modeling of non-linear constitutive behavior permits to simulate the characteristics of both manmade composite material, where the optimum mechanical performance are searched, and organized biological composite structures, where the optimization structural process is adopted. It is well now that, on account of the presence of solid and fluid constituents at micro-scale level, many biological soft tissues exhibit an overall macroscopic non linear elastic or poro-elastic mechanical behavior too. In this respect, in the second chapter, the biomechanics of corneal structure is modeled through a FE multiphysic approach (thermo-mechanical) in order to simulate its viscoelastic behavior in the outcome of Conducted Keratoplastic surgery (*Fraldi et al. 2010*).

A new multi-scale, three-dimensional finite element model of the cord rubber lamina, based on a hybrid analytical/numerical approach, has been developed in the third chapter. Unlike the aforementioned orthotropic approach that are commonly adopted

in modeling unidirectional laminae, the capability of this model relies on the possibility of simulating the tension-twisting coupling of the cord and, in turn, of the overall composite, which determines a peculiar stress state in the interfacial zone and matrix. Cord behavior has been first modeled by using Costello's analytical model, which accounts for tension-twisting coupling and relates the cord constitutive behavior to the hierarchical structure of the cord itself. Finally, on the basis of this analytical model, a homogenized cylindrical cords model, embedded in a rubber matrix, have been implemented in the FEM code.

In conclusion, in the light of the scientific and practical interest in the mechanical response of polymeric thin films utilized for food packaging, the mechanisms governing the delamination phenomena observed experimentally in multilayer films during HPP have been investigated in order to pave the way for optimal design of packaging structures. To make this, both analytical and Finite Element (FE) analyses of the process of HP treatment of pouches made of multilayer films and containing tap water have been performed.

INTRODUCTION TO COMPOSITE MATERIALS

Characteristic and classification of composite materials [1]	1
Fibrous Composite Materials	2
Laminated Composite materials	2
Particulate Composite Materials	2
Combination of Composite Materials	2
Fundamental Composite Material Terminology [2]	3
Mechanical behavior of composite materials [1]	5
References	6
CHAPTER I: HYPERELASTIC MODELING OF ALCANTARA PANNEL[®] TISSUE	
Introduction	7
The Modeling hypothesis and experimental confirmations	8
The Linearity of stress-strain relations	8
Orthotropic behavior of the Pannel [®]	10
The stiffness tensor definition for Orthotropic materials	10
Generalized Hooke's law	10
Stress-Strain relations between technical moduli and components of elastic tensor.	12
Stress-Strain relations for a lamina of arbitrary orientation	14
Thermodynamic approach for Poisson ratio in orthotropic materials	15
Elastic moduli of orthotropic Pannel [®] tissue	16
Determination of Young's moduli: linear-elastic case	16
Experimental result of the Poisson moduli	16
Shear modulus calculation and stiffness matrix of Pannel	18
Uniaxial tests simulation by Finite Elements analysis under linear orthotropic elasticity and high strains.	21
Anisotropic models in finite elasticity: specialization in the Pannel [®] case	26
Stress-strain tests for hyperelastic materials	26
Explicit definition of Helmholtz' free energy for orthotropic hyperelastic case	27
Stress-strain engineering curves' analytic determination for uniaxial stress tests in longitudinal and crosswise direction.	28

Calibration of Helmholtz hyperelastic model on the Pannel [®] tissue	30
Uniaxial tests simulation by Finite Elements analysis under anisotropic hyperelasticity and high strains.	30
Conclusions	30
References	31
CHAPTER II: FEM MULTIPHYSIC APPROACHES ON THE BIOMECHANICS OF CORNEAL TISSUE	
Introduction	32
Material and Methods	34
The biomechanics of the human cornea	34
Viscoelastic characterization of the corneal tissue	36
The conductive keratoplasty	39
FE modeling and analysis	41
Mechanical Results and discussion	45
Discussion of analysis outcomes	45
The influence of micro-structural anisotropy	52
Multiphysic characterization of Human Cornea	55
State of art on the thermo-mechanical characterization of corneal tissue	55
FE Conductive Keratoplastic simulation: thermo-mechanical approach.	57
Thermal denaturation of collagenous tissue.	58
FE modeling of corneal thermal damage accumulation	59
Coupled Mechanical response during CK surgery (Modelling of non linear mechanical response during thermal damaging)	62
Thermo-Mechanical Results	65
Conclusion	68
References	70
CHAPTER III: MODELLING CORD-RUBBER COMPOSITES FOR TIRE APPLICATION	
Introduction	75
An Overview of tire technology and components	77
Industry standards: size and dimensions	78

Rubber compound	79
Reinforcement materials	80
Cord-rubber Composite Modeling	81
Matrix modeling: Non-linear elasticity	82
Corded reinforcement: textile ‘cord’	83
Effects of intrinsic trigonality and helicoidal interface in twisted cord-rubber composites: a multi scale homogenization approach	85
Micro scale level: Costello’s model	85
Non-linear Costello’s model	92
Meso scale level: Equivalent trigonal cylindrical model	95
Macro scale level: cord-rubber structure	98
FEM Simulation and results	101
Title: A sensitivity analyses on fiber density	105
Conclusion	108
References	110

CHAPTER IV: MECHANICAL RESPONSE OF FOOD PACKAGING POLYMERIC BI-LAYER FILMS UNDER HIGH PRESSURE

Introduction	112
Experimental findings and problem statement	115
Sensitivity analyses and qualitative results based on exact solutions	120
Two-layer film with spatially varying pressure symmetrically applied on the top and bottom sides	121
Spurious bending in a bi-layer hollow cylinder filled with water and subject to external pressure	124
External Pressure and incompressible fluid filled the compound hollow cylinder	125
Bending moment acting on the object ends	126
FE simulations of actual food package under high pressure and comparison with experimental evidences	128
FE analyses of the PP/PET, PP/OPA and PP/PA food packages under increasing pressures	128
Wrinkling effects and strain gradients in PP/PET food packages under severe pressures	135
Conclusion	137

INTRODUCTION TO COMPOSITE MATERIALS

Characteristic and classification of composite materials [1]

The word *composite* in the term *composite material* means that two or more material are combined on a macroscopic scale to form a useful third material. The key is the macroscopic examination of a material wherein the components can be identified by the naked eye.

The definition of a composite material is flexible and can be augmented to fit specific requirements. A composite material is considered to be one that contains two or more distinct constituents with significantly different macroscopic behavior and a distinct interface between each constituent (on the microscopic level). This includes the continuous fiber laminated composites of primary concern herein, as well as a variety of composites not specifically addressed.

The advantage of composite materials is that, if well designed, they usually exhibit the best qualities of their components or constituent and often some qualities that neither constituent possesses:

- Strength
- Stiffness
- Corrosion resistance
- Weight
- Fatigue life
- Temperature depend behavior
- Thermal insulation thermal conductivity

Naturally not all of this properties are improved at the same time nor is there usually any requirement to do so. In fact, of the properties are in conflict with one other, e.g., thermal conductivity with thermal insulation Composite materials have been in existence for many centuries. No record exists as to when people first started using composites. Some of the earliest records of their use date back to the Egyptians, who are credited with the introduction of plywood, and the use of straw in mud for strengthening bricks.

Composite materials can be classified through their material coupled. Four commonly accepted types of composite materials are:

1. Fibrous composite materials that consist of fibers in a matrix;
2. Laminates composite materials that consist of layers of various materials;
3. Particulate composite materials that are composed of particles in a matrix;

4. Combinations of some or all of the first three types.

These types of composite materials are described briefly below.

Fibrous Composite Materials

Long fibers in various forms are inherently much stiffer and stronger than the same material in bulk form. For example, ordinary plate glass fractures at stresses of only a few MPa (20 MPa), yet glass fibers have strengths of 2800 to 4800 MPa, in commercial available forms and about 7000 MPa in laboratory-prepared forms. Obviously, then, the geometry and physical makeup of a fiber are somehow crucial application. More properly, the paradox of a fiber having different properties from the bulk form is due to the more perfect structure of a fiber. In fiber, the crystal defects are aligned along the fiber axis. Moreover, there are fewer internal defects in fibers than in bulk material. For example, in materials that have dislocations, the fibers form has dislocation than the bulk form.

Laminated Composite materials

Laminated composite materials consist of layers of at least two different materials that are bonded together. Lamination is used to combine the best aspects of the constituent layers and bonding material in order to achieve a more useful material. The properties that can be emphasized by lamination are strength, stiffness, low weight, corrosion resistance, wear resistance, thermal insulation, etc. Such claims are best represented bimetals, clad metals, laminate glass, plastic-based laminates and laminates composite materials.

Particulate Composite Materials

Particulate composite materials consist of one or more material suspended in a matrix of another material. The particles can be either metallic or non metallic as can the matrix. There are different combinations as *nonmetallic particles in nonmetallic matrix composite material and nonmetallic particles in metallic matrix composite material*.

Combination of Composite Materials

Numerous multiphase composite materials exhibit more than one characteristic of the various classes, fibrous, laminated, or particulate composite materials, just discussed. For example, reinforced concrete is both particulate and fibrous. Also, laminated fiber-reinforced composite materials are obviously both laminated and fibrous composite materials. Thus, any classification system is arbitrary and imperfect. Nevertheless, the system should serve to acquaint the reader with the broad possibilities of composite materials. Laminated fiber-reinforced material are a hybrid

class of composite materials involving both fibrous composite materials and lamination techniques. Here, layers of a fiber-reinforced materials are bounded together with the fiber directions of each layer typically oriented in different direction to give different strengths and stiffnesses of the laminate in various directions. Thus, the strengths and stiffnesses of the laminated fiber reinforced composite materials include rocket motor cases, boat hull, aircraft wing panels and body section, tennis rackets, etc.

Fundamental Composite Material Terminology [2]

Some of the more prominent terms used with composite materials are defined below:

Lamina. A lamina is a flat (or sometimes curved) arrangement of unidirectional (or woven) fibers suspended in a matrix material. A lamina is generally assumed to be orthotropic, and its thickness depends on the material from which it is made. For example, a graphite/epoxy (graphite fibers suspended in an epoxy matrix) lamina may be on the order of 0.127 mm thick. For the purpose of analysis, a lamina is typically modeled as having one layer of fibers through the thickness. This is only a model and not a true representation of fiber arrangement. Both unidirectional and woven lamina are schematically shown in **figure 1.1**

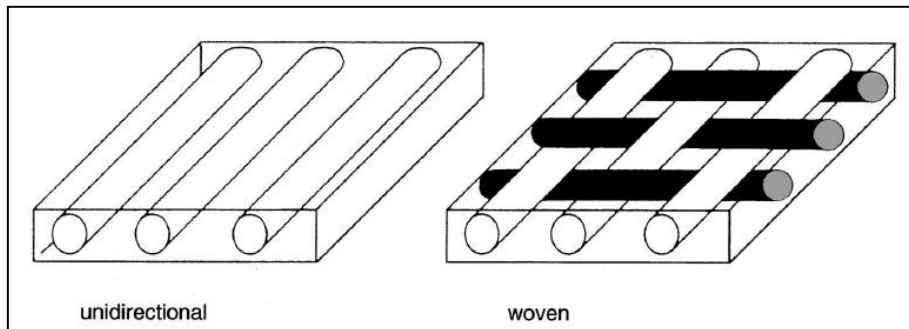


Fig 1.1. Schematic representation of unidirectional and woven composite lamina

Reinforcements. Reinforcements are used to make the composite structure or component stronger. The most commonly used reinforcements are boron, glass, graphite (often referred to as simply carbon), and Kevlar, but there are other types of reinforcements such as alumina, aluminum, silicon carbide, silicon nitride, and titanium.

Fibers. Fibers are a special case of reinforcements. They are generally continuous and have diameters ranging from 3-200 μm . Fibers are typically linear elastic or elastic-perfectly plastic and are generally stronger and stiffer than the same material in bulk form. The most commonly used fibers are boron, glass, carbon, and Kevlar.

Matrix. The matrix is the binder material that supports, separates, and protects the fibers. It provides a path by which load is both transferred to the fibers and redistributed among the fibers in the event of fiber breakage. The matrix typically has a lower density, stiffness, and strength than the fibers. Matrices can be brittle, ductile, elastic, or plastic. They can have either linear or nonlinear stress-strain behavior. In addition, the matrix material must be capable of being forced around the reinforcement during some stage in the manufacture of the composite. Fibers must often be chemically treated to ensure proper adhesion to the matrix. The most commonly used matrices are carbon, ceramic, glass, metal, and polymeric. Each has special appeal and usefulness, as well as limitations. A typical classification present in literature of matrix is shown below:

1. *Carbon Matrix.* A carbon matrix has a high heat capacity per unit weight. They have been used as rocket nozzles, ablative shields for reentry vehicles, and clutch and brake pads for aircraft.
2. *Ceramic Matrix.* A ceramic matrix is usually brittle. Carbon, ceramic, metal, and glass fibers are typically used with ceramic matrices in areas where extreme environments (high temperatures, etc.) are anticipated.
3. *Glass Matrix.* Glass and glass-ceramic composites usually have an elastic modulus much lower than that of the reinforcement. Carbon and metal oxide fibers are the most common reinforcements with glass matrix composites. The best characteristics of glass or ceramic matrix composites is their strength at high service temperatures. The primary applications of glass matrix composites are for heat-resistant parts in engines, exhaust systems, and electrical components.
4. *Metal Matrix.* A metal matrix is especially good for high-temperature use in oxidizing environments. The most commonly used metals are iron, nickel, tungsten, titanium, magnesium, and aluminum. There are three classes of metal matrix composites:

Class I. The reinforcement and matrix are insoluble (there is little chance that degradation will affect service life of the part).

Class II. The reinforcement/matrix exhibit some solubility (generally over a period of time and during processing) and the interaction will alter the physical properties of the composite.

Class III. The most critical situations in terms of matrix and reinforcement are in this class. The problems encountered here are generally of a manufacturing

5. *Polymer Matrix.* Polymeric matrices are the most common and least expensive. They are found in nature as amber, pitch, and resin. Some of the earliest composites were layers of fiber, cloth, and pitch. Polymers are easy to process,

offer good mechanical properties, generally wet reinforcements well, and provide good adhesion. They are a low-density material. Because of low processing temperatures, many organic reinforcements can be used. A typical polymeric matrix is either viscoelastic or viscoplastic, meaning it is affected by time, temperature, and moisture. The terms thermoset and thermoplastic are often used to identify a special property of many polymeric matrices.

Laminate. A laminate is a stack of lamina, as illustrated in Fig 2.1, oriented in a specific manner to achieve a desired result. Individual lamina are bonded together by a curing procedure that depends on the material system used. The mechanical response of a laminate is different from that of the individual lamina that form it. The laminate's response depends on the properties of each lamina, as well as the order in which the lamina are stacked.

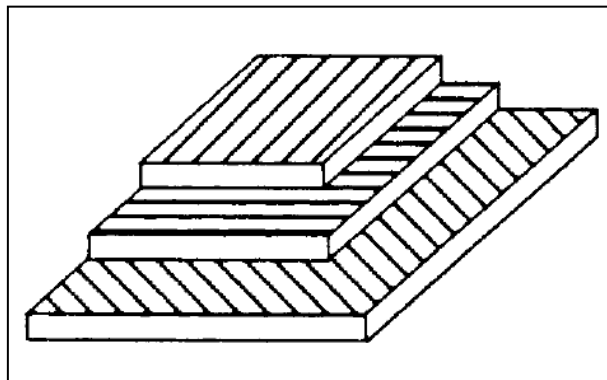


Fig. 2. schematic of laminated composite.

Mechanical behavior of composite materials [1]

Composite materials have many mechanical behavior characteristics that are different from those of more conventional engineering materials. Some characteristics are merely modifications of conventional behavior; others are totally new and require new analytical and experimental procedures.

Most commonly engineering materials are both homogeneous and isotropic:

A *homogeneous* body has uniform properties throughout, i.e., the properties are independent of position in the body; An *isotropic* body has material properties that are the same in every direction at a point in the body, i.e., the properties are independent of orientation at a point in the body.

In contrast, composite materials are often both *inhomogeneous* and *nonisotropic*.

An *inhomogeneous* body has nonuniform properties over the body, i.e., the properties depend on position in the body. An *anisotropic* body has material properties that are

different in all direction at a point in the body. Thus, the properties depend on orientation at a point in the body.

Some composite materials have very simple forms of inhomogeneity. Because of the inherently heterogeneous nature of composite materials, they are conveniently studied from two points of view: micromechanics and macromechanics. The first studies the composite materials behavior wherein the interaction of the constituent materials is examined on a microscopic scale to determine their effect on the properties of the composite material. Macromechanics is the study of composite material behavior wherein the material is presumed homogeneous and the effect of the constituent materials are detected only as averaged apparent macroscopic properties of the composite material.

Use of the two concept of macromechanics and micromechanics allow the tailoring of a composite material to meet a particular structural requirement with little waste of material capability. The ability to tailor a composite material to its job is one of the most significant advantages of a composite material over an ordinary material. Perfect tailoring of a composite material yields only the stiffness and strength required in each direction, no more. In contrast, an isotropic material is, by definition, constrained to have excess strength and stiffness in any direction other than that of the largest required strength or stiffness. The inherent anisotropy (most often only orthotropy) of composite materials leads to mechanical behavior characteristic that are quite different from those of conventional isotropic materials.

References

- [1] Jones RM (1999) Mechanics of Composite Materials. Taylor e Francis
- [2] Staab GH (1999) Laminar Composites. Butterworth-Heinemann

Equation Chapter 1 Section 1

CHAPTER I

HYPERELASTIC MODELING OF ALCANTARA PANNEL® TISSUE

Introduction

ALCANTARA® is an innovative material obtained from the combination of an advanced spinning process (low-denier, bi-component sea-island type fiber) and other textile and chemical production processes (needling, grinding, impregnation, extraction, finishing, dyeing), it is carried out in accordance with absolutely unique procedures. It combines softness, elegance, and rich color with high resistance to wear and tear and incredible ease of maintenance. It is perfectly suited to innovative, prestigious applications in interior design, car upholstery, fashion, and clothing accessories. ALCANTARA® is a no-woven composite material resulting from a complex chemical and textiles technological processes. Although it appears macroscopically as homogeneous, the observation of tissue under an electron microscope (**Figure 1**), detects a microstructure of fibers distribution and their orientation that the material retains from the several processes of tissue manufacture. The mechanical test conducted on Pannel® highlight a markedly anisotropic behavior of structures, where it exhibits a non linear stress-strain behavior in high level of deformation, thermoelastic properties and stress relaxation viscoelastic phenomena.

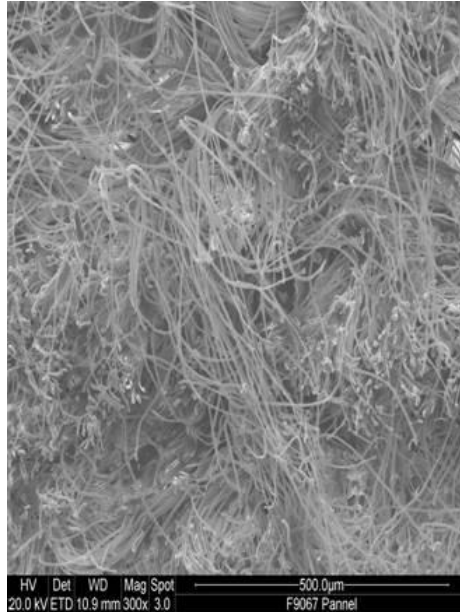


Figure 1.1: Microstructure of fibers distribution observed in electron microscope tissue image

In this chapter, with reference to experimental tests results and using continuum theory, will be explain the formulation of a linear orthotropic model of Pannel[®], describing individual component of the tensor of elasticity and then validating the theoretical results by comparison with laboratory tests. Successively this mechanical model will be generalized into the non-linear hyperelastic model by the definition of Helmholtz free energy and introducing specific microstructure tensors. On the base of discussion will be neglects both the effect of temperature on the mechanical properties of the medium that the contribution of the viscoelastic material.

The Modeling hypothesis and experimental confirmations

The hypothesis of the linear modeling are:

1. The Linearity of stress-strain relations
2. The Orthotropic behavior of the tissue

The Linearity of stress-strain relations

The uniaxial experimental tests conducted under quasi static load and large deformation (0%-65%), have showed a typical non linear response of the hyperelastic materials. Tensile properties may vary with specimen preparation and with speed and environment of testing. In fact to characterize the anisotropic behavior of the tissue, the samples were carved with different direction: The test were conducted in longitudinal (0°), diagonal (45°) and transversal (90°) directions, where longitudinal

direction was considered as *conduct roll direction*. The experimental were performed according to the *ASTM D-638* test method, that it covers the determination of the tensile properties of unreinforced and reinforced plastics in the form of standard dumbbell-shaped test specimens when tested under defined conditions of pretreatment, temperature, humidity, and testing machine speed. In picture below (Figure 2) have shown the experimental tensile test results for each direction:

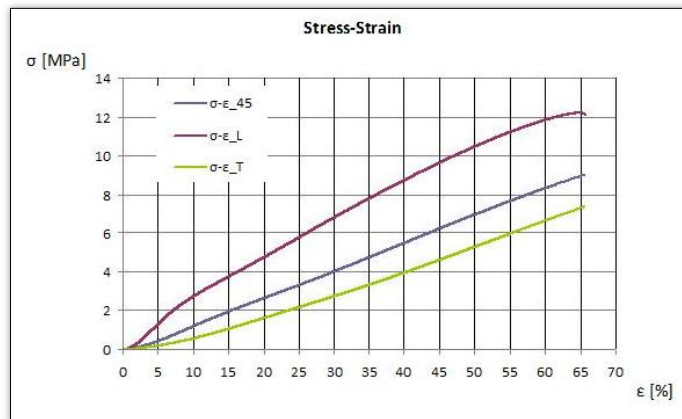


Figure 1.2: experimental tensile test results

As showing in the picture, the non linear tensile response of tissue has different behavior at the initial deformation $0\% - 10\%$ and the large deformation ($\epsilon > 50\%$). In the first case the non linearity is due to several factors, primarily to the starting of the tensile test than to the reorganization of the micro-structures. The composite materials exhibit this behavior at initial deformation, which is called the *toe-region*. The large deformation behavior is a typical response showed by the material brought at break. In this parts of chapter we want to consider the response of the tissue in large deformation range $10\% - 50\%$ which is representative of the operating conditions of the material. in this range the response of the tissue can be approximated by linear response as showed in the picture (Figure 3).

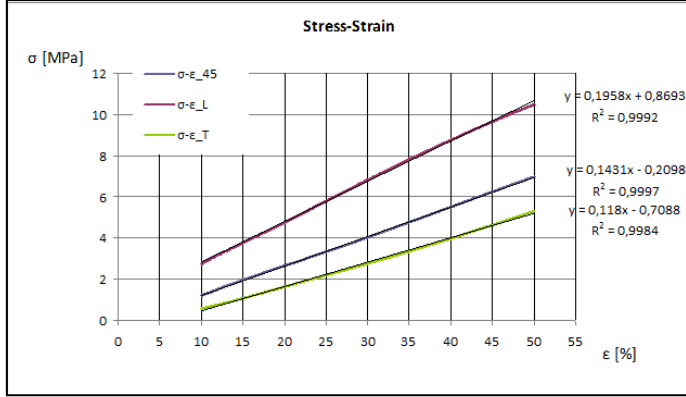


Figure 1.3: linear approximation of the tissue in large deformation

For the purposes of modeling the elastic behavior of the Pannel[®] in the range of deformation of interest 10%–50% , the assumption of linearity of the stress-strain response can thus be considered realistic and supported by experimental evidence.

Orthotropic behavior of the Pannel[®]

Taking into consideration the influence of the micro-structure of the tissue on the its tensile response, the mechanical behavior of the Pannel[®] can be modeled as anisotropic. In fact the off axis tests allowed us to build the different stress-strain curves showed in the picture above and in this case the homogeneous micro-structural organization of the reinforcing fibers suggest to model the behavior of the Pannel[®] as orthotropic. The principal directions of the material will therefore be represented by a cartesian coordinate system with the three axes parallel to the longitudinal direction respectively, **L** (the direction of development roll), **T** (orthogonal to L and belongs to the median of the sample) and, parallel to the thickness tissue specimen and orthogonal to the mean plane of the same.

The stiffness tensor definition for Orthotropic materials

Generalized Hooke's law

The most general linear relationship between the independent components of the stress, and the dual components of deformation, is called the *generalized Hooke's law* and is written as follows:

$$\sigma_{ij} = E_{ijkl} \epsilon_{kl} \quad (1.1)$$

Where E_{ijkl} is the stiffness tensor and the relative Voigt notation contains $6 \times 6 = 36$ coefficients.

The additional requirement of elasticity is ensured by the existence of a strain potential φ . It assume the physical means of strain energy density function hence the reversibility of load-unload cycles and it is unconnected from the strain history (*Sadd, M.H, 2005*). With these assumptions can be wrote the following relation:

$$\frac{\partial \varphi}{\partial \varepsilon_{ij}} \equiv \sigma_{ij} = E_{ijkl} \varepsilon_{kl} \Rightarrow \frac{\partial^2 \varphi}{\partial \varepsilon_{ij} \partial \varepsilon_{kl}} = \frac{\partial \sigma_{ij}}{\partial \varepsilon_{kl}} = E_{ijkl} \quad (1.2)$$

The Schwartz's theorem involves the symmetry of stiffness tensor

$$\frac{\partial^2 \varphi}{\partial \varepsilon_{ij} \partial \varepsilon_{kl}} = \frac{\partial^2 \varphi}{\partial \varepsilon_{kl} \partial \varepsilon_{ij}} \Rightarrow E_{klij} = E_{ijkl} \quad (1.3)$$

and the reduction of elastic constants to 21 (monoclinic or triclinic materials).

The existence of various combinations of the different symmetry forms implies a corresponding classification of the anisotropy classes of the materials. In particular, two extreme cases of anisotropic elastic materials are the triclinic materials and the isotropic ones. The first material possesses no rotational symmetry or a plane of reflection symmetry, while the second material possesses infinitely many rotational symmetries and planes of reflection symmetry.

If the anisotropic plane reduces to three orthogonal plane the material is called orthotropic. The number of the independent elastic constants is 9 and the stiffness matrix assumes the following form:

$$\begin{bmatrix} \sigma_{11} \\ \sigma_{22} \\ \sigma_{33} \\ \sigma_{12} \\ \sigma_{13} \\ \sigma_{23} \end{bmatrix} = \begin{bmatrix} E_{1111} & E_{1122} & E_{1133} & 0 & 0 & 0 \\ E_{1122} & E_{2222} & E_{2233} & 0 & 0 & 0 \\ E_{1133} & E_{2233} & E_{3333} & 0 & 0 & 0 \\ 0 & 0 & 0 & E_{1212} & 0 & 0 \\ 0 & 0 & 0 & 0 & E_{1313} & 0 \\ 0 & 0 & 0 & 0 & 0 & E_{2323} \end{bmatrix} \begin{bmatrix} \varepsilon_{11} \\ \varepsilon_{22} \\ \varepsilon_{33} \\ \varepsilon_{12} \\ \varepsilon_{13} \\ \varepsilon_{23} \end{bmatrix} \quad (1.4)$$

In the in the state of *plane stress* $\sigma_{33} = \sigma_{13} = \sigma_{23} = 0$, as shown in Figure 4, the system equation above can be reduced to:

$$\begin{bmatrix} \sigma_1 \\ \sigma_2 \\ \sigma_3 \end{bmatrix} = \begin{bmatrix} E_{11} & E_{12} & 0 \\ E_{12} & E_{22} & 0 \\ 0 & 0 & E_{33} \end{bmatrix} \begin{bmatrix} \varepsilon_1 \\ \varepsilon_2 \\ \varepsilon_3 \end{bmatrix}, \quad \sigma = \mathbb{E} \varepsilon \quad (1.5)$$

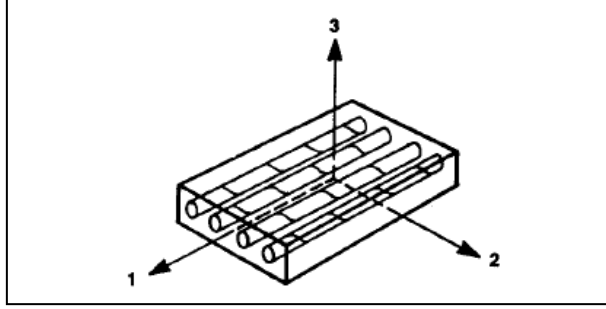


Figure 14: Unidirectionally reinforced lamina

Where

$$\begin{aligned} \sigma_1 = \sigma_{11}, \quad \sigma_2 = \sigma_{22}, \quad \sigma_3 = \sigma_{12}, \quad \varepsilon_1 = \varepsilon_{11}, \quad \varepsilon_2 = \varepsilon_{11}, \quad \varepsilon_3 = 2\varepsilon_{12} \\ E_{1111} = E_{11}, \quad E_{2222} = E_{22}, \quad E_{1122} = E_{12}, \quad E_{1133} = E_{13}, \quad E_{2233} = E_{23}, \quad E_{1212} = E_{33} \end{aligned} \quad (1.6)$$

Considering that the tensor \mathbb{E} is defined positive, it is possible to obtain the relations below

$$\begin{bmatrix} \varepsilon_1 \\ \varepsilon_2 \\ \varepsilon_3 \end{bmatrix} = \begin{bmatrix} S_{11} & S_{12} & 0 \\ S_{12} & S_{22} & 0 \\ 0 & 0 & S_{33} \end{bmatrix} \begin{bmatrix} \sigma_1 \\ \sigma_2 \\ \sigma_3 \end{bmatrix}, \quad \varepsilon = \mathbb{S}\sigma \quad (1.7)$$

Where the operator S_{ijhk} is called *compliance tensor*. The relation between elastic tensor and compliance tensor are defined by

$$E_{11} = \frac{S_{22}}{S_{11}S_{22} - S_{12}^2}, \quad E_{22} = \frac{S_{11}}{S_{11}S_{22} - S_{12}^2}, \quad E_{12} = \frac{S_{12}}{S_{11}S_{22} - S_{12}^2}, \quad E_{13} = \frac{1}{S_{33}}$$

Stress-Strain relations between technical moduli and components of elastic tensor.

In the plane stress condition, from the experimental tests results, it's possible calculate four elastic coefficients, called technical moduli. They are the Young's moduli in the longitudinal and transversal directions, E_L and E_T respectively, the Poisson coefficient ν_{LT} (or $\nu_{TL} = \nu_{LT} E_T E_L^{-1}$), and shear modulus in the stress plane; where this last one it's coincident with Lamè modulus. This technical modules can be obtained from three typical experimental test: two *monoaxial* tests and one *biaxial* or *pure shear* test. For the uniaxial longitudinal test, we have that:

$$\sigma_L = E_{11}\varepsilon_L + E_{12}\varepsilon_T, \quad \sigma_T = E_{12}\varepsilon_L + E_{22}\varepsilon_T \quad (1.8)$$

Or, in the deformation case:

$$\varepsilon_L = \frac{E_{22}}{E_{11}E_{22} - E_{12}^2} \sigma_L, \quad \varepsilon_T = -\frac{E_{12}}{E_{11}E_{22} - E_{12}^2} \sigma_L \quad (1.9)$$

From the definitions of Young's modulus and Poisson's ratio, we can determine the technical moduli:

$$E_L \equiv \frac{\sigma_L}{\varepsilon_L} = \frac{E_{11}E_{22} - E_{12}^2}{E_{22}}, \quad \nu_{LT} \equiv -\frac{\varepsilon_T}{\varepsilon_L} = \frac{E_{12}}{E_{22}} \quad (1.10)$$

whereas in the transversal direction we obtain

$$E_T \equiv \frac{\sigma_T}{\varepsilon_T} = \frac{E_{11}E_{22} - E_{12}^2}{E_{11}}, \quad \nu_{TL} \equiv -\frac{\varepsilon_L}{\varepsilon_T} = \frac{E_{12}}{E_{11}} \quad (1.11)$$

From the pure shear test we can write the relation below:

$$\sigma_{LT} = 2E_{33}\varepsilon_{LT} \Rightarrow G_{LT} \equiv \frac{\sigma_{LT}}{2\varepsilon_{LT}} = E_{33} \quad (1.12)$$

In this condition we rewrite the tensors

$$\mathbb{E} = \begin{bmatrix} \frac{E_L}{1-\nu_{LT}\nu_{TL}} & \frac{\nu_{LT}E_T}{1-\nu_{LT}\nu_{TL}} & 0 \\ \frac{\nu_{LT}E_L}{1-\nu_{LT}\nu_{TL}} & \frac{E_T}{1-\nu_{LT}\nu_{TL}} & 0 \\ 0 & 0 & G_{LT} \end{bmatrix}, \quad \mathbb{S} = \begin{bmatrix} \frac{1}{E_L} & -\frac{\nu_{LT}}{E_L} & 0 \\ -\frac{\nu_{LT}}{E_L} & \frac{1}{E_T} & 0 \\ 0 & 0 & \frac{1}{G_{LT}} \end{bmatrix} \quad (1.13)$$

Where the symmetry condition has been considered:

$$\frac{\nu_{LT}}{\nu_{TL}} = \frac{E_L}{E_T} \quad (1.14)$$

At last, considering the isotropic case relations, the Lamè's modulus can be obtained from the relations above:

$$G_{TT'} = \frac{E_T}{2(1+\nu_{TT'})} \quad (1.15)$$

Stress-Strain relations for a lamina of arbitrary orientation

In the previous section, the stress and strain were defined in the principal material coordinates for an orthotropic material. The principal direction of orthotropy often do not coincide with coordinate direction that are geometrically natural to the solution of the problem. For example a laminated plates with different laminae at different orientation (*Jones RM, 1999*). Thus, a relation is needed between the stresses and strain in the principal material coordinates and those in the body coordinates. Then, a method of trasforming stress.-strain relation from one system to another is also needed. At this point, we recall from elementary mechanics of materials the transformation equation for expressing stresses in an x-y coordinate system in terms of stresses in a 1-2 coordinate system,

$$\begin{bmatrix} \sigma_x \\ \sigma_y \\ \tau_{xy} \end{bmatrix} = [Q] \begin{bmatrix} \sigma_1 \\ \sigma_2 \\ \tau_{12} \end{bmatrix} = \begin{bmatrix} \cos^2 \theta & \sin^2 \theta & -2 \sin \theta \cos \theta \\ \sin^2 \theta & \cos^2 \theta & 2 \sin \theta \cos \theta \\ \sin \theta \cos \theta & -\sin \theta \cos \theta & \cos^2 \theta - \sin^2 \theta \end{bmatrix} \begin{bmatrix} \sigma_1 \\ \sigma_2 \\ \tau_{12} \end{bmatrix} \quad (1.16)$$

Where θ is the angle *from* the x-axis *to* the 1-axis Figure 5. Note especially that the transformation has nothing to do with the material properties but is merely a rotation of stress direction. Also, the *direction* of rotation is crucial.

Similarly, the strain-transformation equation are

$$\begin{bmatrix} \varepsilon_x \\ \varepsilon_y \\ \frac{\gamma_{xy}}{2} \end{bmatrix} = [Q] \begin{bmatrix} \varepsilon_1 \\ \varepsilon_2 \\ \frac{\gamma_{12}}{2} \end{bmatrix} = \begin{bmatrix} \cos^2 \theta & \sin^2 \theta & -2 \sin \theta \cos \theta \\ \sin^2 \theta & \cos^2 \theta & 2 \sin \theta \cos \theta \\ \sin \theta \cos \theta & -\sin \theta \cos \theta & \cos^2 \theta - \sin^2 \theta \end{bmatrix} \begin{bmatrix} \varepsilon_1 \\ \varepsilon_2 \\ \frac{\gamma_{12}}{2} \end{bmatrix} \quad (1.17)$$

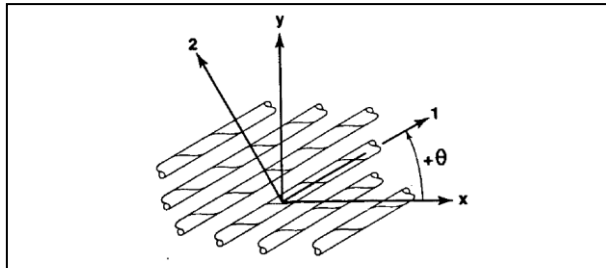


Figure 1.5: Positive rotation of principal material axes from x-y Axes

where we observe that strains do trasform with the same transformation as stresses if the tensor defintion of shear strain is used (which is equivalent to dividing the engineering shear strain by two). A so-called specially orthotropic lamina is as

orthotropic lamina whose principal material axes are aligned with the natural body axes:

$$\begin{bmatrix} \sigma_x \\ \sigma_y \\ \tau_{xy} \end{bmatrix} = \begin{bmatrix} \sigma_1 \\ \sigma_2 \\ \tau_{12} \end{bmatrix} = \begin{bmatrix} E_{11} & E_{12} & 0 \\ E_{12} & E_{22} & 0 \\ 0 & 0 & E_{33} \end{bmatrix} \begin{bmatrix} \varepsilon_1 \\ \varepsilon_2 \\ \gamma_{12} \end{bmatrix} \quad (2.2.107)$$

These stress-strain relation were introduced in the previous section and apply when the principal material direction of an orthotropic lamina are used as coordinates. The stiffness tensor and compliance tensor in the rotate coordinate system can be written through the relations

$$\mathbb{E}^\theta = \mathbf{Q} \mathbb{E} \mathbf{Q}^{-1}, \quad \mathbb{S}^\theta = \mathbf{Q} \mathbb{S} \mathbf{Q}^{-1} \quad (2.2.108)$$

The analytical expressions of \mathbb{E}^θ are reported below:

$$\begin{aligned} E_{11}^\theta &= E_{11} \cos^4 \theta + E_{22} \sin^4 \theta + 2 E_{12} + 2E_{33} \sin^2 \theta \cos^2 \theta \\ E_{22}^\theta &= E_{11} \sin^4 \theta + E_{22} \cos^4 \theta + 2 E_{12} + 2E_{33} \sin^2 \theta \cos^2 \theta \\ E_{33}^\theta &= E_{11} + E_{22} - 2E_{12} - 2E_{33} \sin^2 \theta \cos^2 \theta + E_{33} \sin^4 \theta + \cos^4 \theta \\ E_{12}^\theta &= E_{11} + E_{22} - 4E_{33} \sin^2 \theta \cos^2 \theta + E_{12} \sin^4 \theta + \cos^4 \theta \\ E_{13}^\theta &= E_{11} - E_{12} - 2E_{33} \sin \theta \cos^3 \theta - (E_{22} - E_{12} - 2E_{33}) \sin^3 \theta \cos \theta \\ E_{23}^\theta &= (E_{11} - E_{12} - 2E_{33}) \sin^3 \theta \cos \theta - (E_{22} - E_{12} - 2E_{33}) \sin \theta \cos^3 \theta \end{aligned} \quad (1.18)$$

Similarly can be calculated the expressions for compliance tensor.

Thermodynamic approach for Poisson ratio in orthotropic materials

It's important to note that if one assumes an orthotropic material, unlike the isotropic case, the forms of transverse contraction (Poisson modules), while retaining the same physical and geometric meaning, they must obey the classic case of easier isotropy. Mathematical restriction impose that the range of value for Poisson ratio is imposed by the positive elastic tensor, this last connected with the positive stain energy function, where we have that:

$$\{\forall \varepsilon_{ij} \neq 0, \quad \varphi := \frac{1}{2} E_{ijhk} \varepsilon_{ij} \varepsilon_{hk} > 0\} \Rightarrow \mathbb{E} \equiv [E_{ijhk}] = \text{def } \textit{positive}$$

which is equivalent to imposing that the determinant of the all minors of the elastic tensor operator (stiffness \mathbb{E} or compliance \mathbb{S}) are strictly positive. In the plane case and considering the symmetry condition $\nu_{LT} E_T = \nu_{TL} E_L$ we obtain the following limitations

$$E_L > 0, E_T > 0, G_{LT} > 0, \quad -\sqrt{\frac{E_L}{E_T}} < \nu_{LT} < \sqrt{\frac{E_L}{E_T}}$$

then

$$\{E_L > E_T = \alpha E_L, \alpha \in]0, 1[\subset \mathbb{R}^+\} \Rightarrow \nu_{LT} \in (-\alpha^{-1}, \alpha^{-1}) \supset]-1, 1[$$

This confirm that, for the plane case and for orthotropic material, the usual range $]-1, 1[$ of Poisson modules - that in the three-dimensional and isotropy case is further confined to the range $]-1, 1/2[$ - can be violated in general, making it eligible, both theoretically and experimentally, the values of the transverse contraction modules less -1 and/or greater the unit value.

Elastic moduli of orthotropic Pannel[®] tissue

Determination of Young's moduli: linear-elastic case

In the previous chapter it has discussed the legality of the orthotropic and linear elasticity response of the Pannel[®] tissue. This hypothesis have been confirmed by the linear fitting of the stress-strain curve in the picture above **figure N°** in the range of large deformations. Starting by the mathematical expression of linear regression curves, obtained by the fitting procedure, we can calculate the young's elastic moduli for each test type, obtaining the following values for longitudinal, **L**, diagonal, **D** $\theta = 45^\circ$ and transversal, **T**, directions respectively:

$$\forall \varepsilon \in (10\% - 50\%), \quad \{E_L = 19.58 \text{ MPa}, E_D = 14.31 \text{ MPa}, E_T = 11.80 \text{ MPa}\}$$

Experimental result of the Poisson moduli

Through the uniaxial experimental test, made on the Pannel tissue, it was possible to draw the evolution of Poisson ratio at several strain values, for longitudinal and transversal case

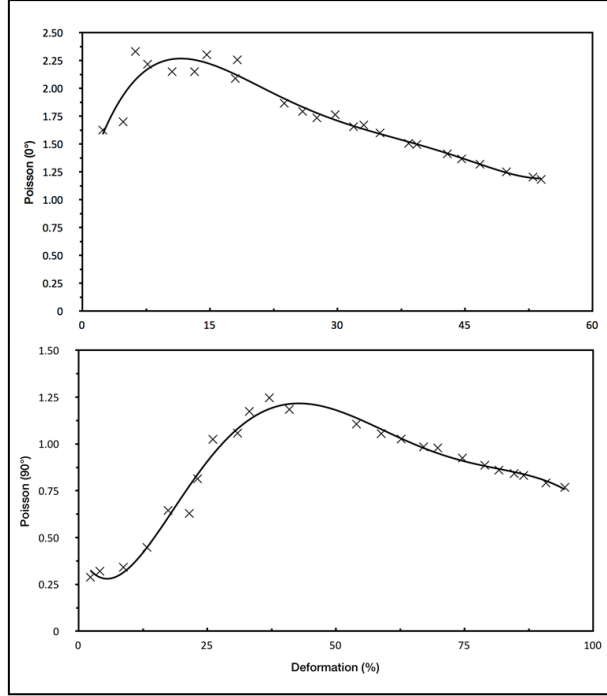


Figure 1.6: dependence of deformation value on Poisson ratio

The graphs on figure 6 highlight how the Poisson ratio values depend on deformation values, along longitudinal and transversal direction. In particular it's important to note that the Poisson ratio is both non linear and non monotonic while the deformation is constant. Furthermore, the values of the moduli vary on the range between 0.25 and about 2.25. This interval is not compatible with those established for the linear case by equation (22), in fact, substituting the numerical values of the technical moduli determined by relations (24) we have

$$\{-1.29 = -\sqrt{E_L E_T^{-1}} < \nu_{LT} < \sqrt{E_L E_T^{-1}} = 1.29\} \Rightarrow \sup \nu_{LT} < 2.25$$

We can state that orthotropic linear elastic model it cannot be used to model comprehensively the overall response of the material considered. In particular to model the rearrangement of micro-structure of the Pannel tissue, during the deformation, need more accurate micro-mechanical models and particular homogenization algorithms to model the overall macro-mechanical response of the structure. However in the sequel of chapter we consider only isochoric deformations then the Poisson modulus is fixed at $\nu_{LT} = 0.5$.

Moreover, although the effect of the values close to the end points of the mechanical compatibility of the Poisson modulus influence the components of stiffness tensor, the fixed value $\nu_{LT} = 0.5$ don't affect the Young's modulus value evaluated respect to θ .

Shear modulus calculation and stiffness matrix of Pannel

In this section will be presented the

- The calculus of shear modulus G_{LT} through the diagonal Young modulus E_D ;
- The stiffness matrix and compliance matrix of the orthotropic model of Pannel presented above.

To evaluate the shear modulus G_{LT} we refers to diagonal modulus E_D obtained through the uniaxial tensile test and the equations (18) and (20). With simple mathematical manipulation can be obtain the equation below:

$$E_\theta \equiv \{[\mathbb{S}^\theta]_{11}\}^{-1} = 8\alpha E_L G_{LT} \times \\ \times \{G_{LT}[3(1+\alpha) - 2\alpha\nu_{LT} - 4(1-\alpha)\cos 2\theta + (1+\alpha + 2\alpha\nu_{LT})\cos 4\theta] + \alpha E_L(1 - \cos 4\theta)\}^{-1}$$

where $\alpha = E_T E_L^{-1}$.

In particular the value of E_θ when $\theta = \pi/4$ for $E_\theta = E_D$ is given by:

$$E_\theta|_{\theta=\pi/4} = E_D \Rightarrow G_{LT} = \frac{\alpha E_D E_L}{4\alpha E_L - E_D(1 + \alpha - 2\alpha\nu_{LT})} \quad (1.19)$$

Replacing the latter equation in equation (26) we obtain the Young's modulus as function of θ , which is numerically not sensitive to variation of the Poisson modulus. In the pictures below (Figure 7) are shown the trend of shear modulus in the polar coordinate system and the trend of shear modulus versus Poisson ratio (Figure 8), in which the elastic moduli have the value of (24), respectively.

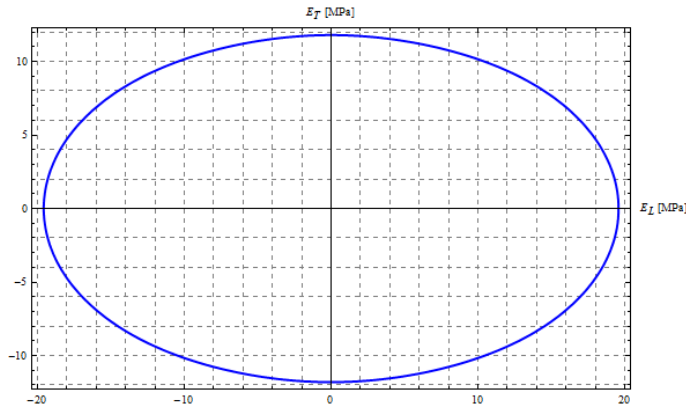


Figure 1.7: the trend of shear modulus in the polar coordinate system

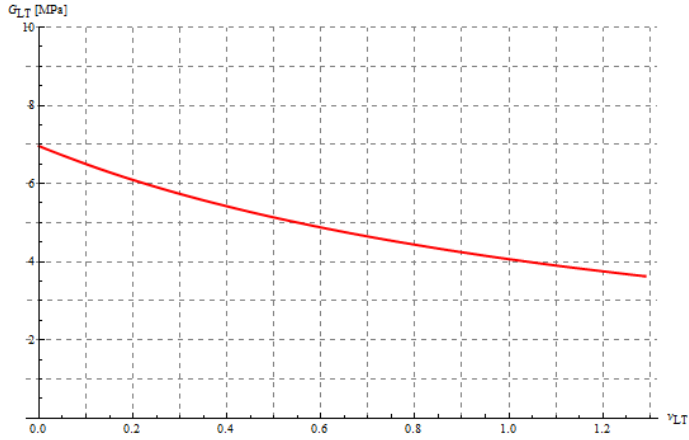


Figure 1.8: trend of shear modulus versus Poisson ratio

At last, is important to note that although the influence of ν_{LT} on the E_θ is negligible, the Poisson ratio values close to the end points of the mechanical compatibility, may enhance the profiles and intensity of the components of the stiffness tensor, E_θ see (Figure 9).

Regarding the second goal of this section, once determined the expressions of the all elastic moduli, the construction of the stiffness and deformability matrices of the Pannel can be obtained through the relations in (18) and using the equation in (20).

Whit equation (14) and through mathematical manipulation , can be wrote the expression of the tensors \mathbb{E} and \mathbb{S} in the principal symmetry coordinate system of the material.

$$\mathbb{E}^{Pannel} [MPa] = \begin{bmatrix} 23.05 & 6.95 & 0 \\ 6.95 & 13.89 & 0 \\ 0 & 0 & 5.13 \end{bmatrix}, \quad \mathbb{S}^{Pannel} [MPa^{-1}] = \begin{bmatrix} 0.0511 & -0.0255 & 0 \\ -0.0255 & 0.0847 & 0 \\ 0 & 0 & 0.1948 \end{bmatrix} \quad (1.20)$$

In the table below (Table A) are reported the expression of technical elastic moduli.

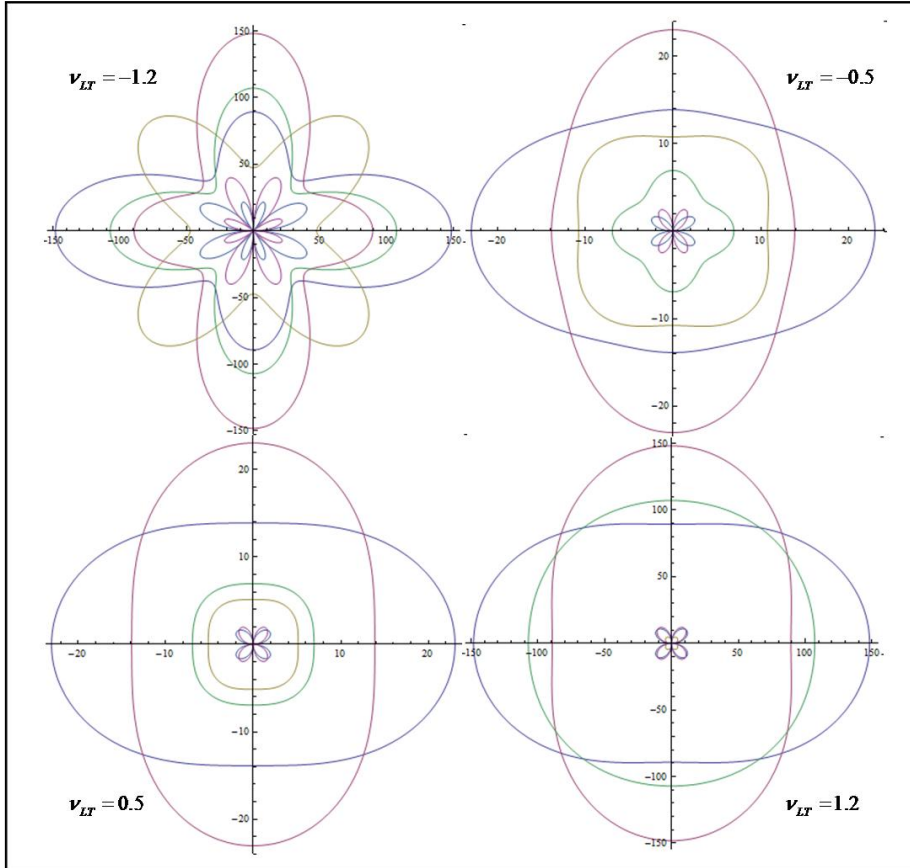


Figure 1.9: the influence of ν_{LT} on the E_{θ}

Technical elastic moduli of Pannel[®]					
(Ortotropic linear elastic model)					
E_L [MPa]	E_T [MPa]	E_D [MPa]	G_{LT} [MPa]	ν_{LT}	$\nu_{TL} = \nu_{LT} E_T E_L^{-1}$
19.58	11.80	14.31	5.13	0.5	0.3

Table A: Technical elastic moduli of Pannel[®]

Uniaxial tests simulation by Finite Elements analysis under linear orthotropic elasticity and high strains.

The results obtained from the FEM modeling of a Pannel® ALCANTARA sample under uniaxial load condition are going to be showed in this paragraph. The loads are separately applied in the three testing directions (longitudinal, crosswise and 45° diagonal respectively), assuming to be valid for the material the linear orthotropic elastic relationship formerly obtained, and making the analysis under static load and high strain conditions.

The geometric model has been designed in ANSYS®, following the ASTM D 638 02a (Standard Test Method for Tensile Properties of Plastics) standard test method (*ASTM International*, 2003), generally used for characterizing the plastic reinforced materials' reaction to traction. Then the sample's shape is of the "dog-bone" type and the particular dimensional specifications are quoted in Figure 10-a (left side).

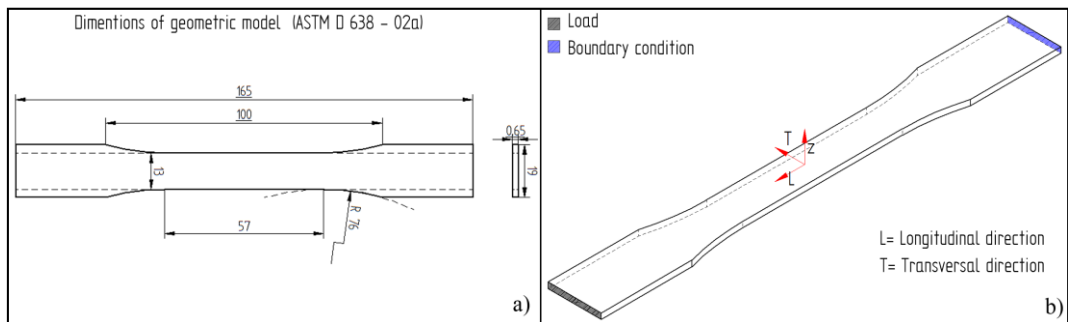


Figure 1.10 Specimen's geometry

According to the experimental results, It has been proved in the previous sections that Pannel® ALCANTARA shows a mostly linear behavior in a 10-50% strain range, thus a linear orthotropic stress-strain reaction is expected in the above mentioned strain range. Evidently, as it's going to be explained hereafter, this linear description will atone a sort of pre-stress, due to strain storage during the initial stage, associated to the high reaction's non-linearity in the early first stage. The FEM model's discretization has been realized by utilizing 8 nodes plane elements (PLANE182) and quadratic form functions on the sides; it is able to calculate either plane stress and plane-strain (ANSYS®). In addition, the finite element PLANE182 allows to implement an anisotropic relationship either linear and hyperelastic, and to analyze big displacement and big strains. Figure 11 shows the discretized model with 2922 elements and 3124 nodes, in particular it shows the resulting mesh regularity, obtained to reduce energy errors associated to concentrated stress gradient.

About orthotropic elastic modules, they have been referred to the linear model formerly obtained in this Report. In particular, in the case of plane stress, this relationship is described from equation Eq.1.5.

Whose explicit expression of the elasticity tensor, as the Cartesian reference system matches the material's principal reference system of symmetry, has already the explicit form in the first matrix on the left of Eq. 1.20.

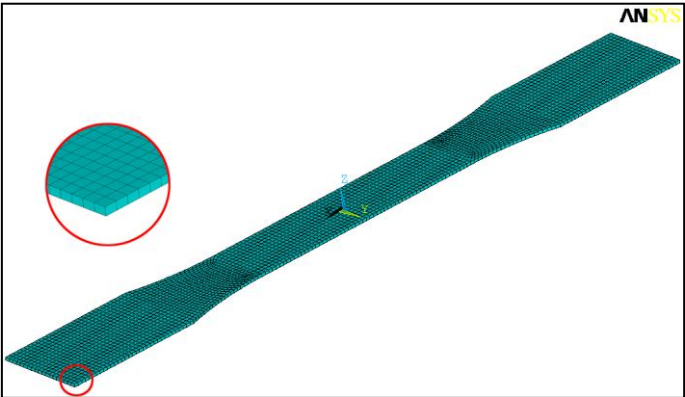


Figure 1.11: specimen FE model

On the model, static analysis have been done to simulate uniaxial traction tests along the axis angled of 0°, 45° and 90° respectively than the sample's longitudinal direction (figure 10-b) and effectuated either under small and big displacements, in order to point out eventual differences in the implemented model's reaction.

In order to retrace the procedure followed in the experimental tests effectuated upon ALCANTARA® samples, the model has been constrained in one tip by a perfect joint, whilst in the opposite one, a uniform displacement has been forced, which is related to a maximum engineering displacement equal to 40%, thus measured as sample's elongation rate in the same direction as the load one. The output tensional condition (fig.10), because of the sample section's variation, naturally has got a spatially non-uniform distribution and so, to calculate the overall sample's stress-strain reaction, it has been rated the normal tension $\bar{\sigma}_L$ average value, homogenized above n elements laying in the model's middle section.

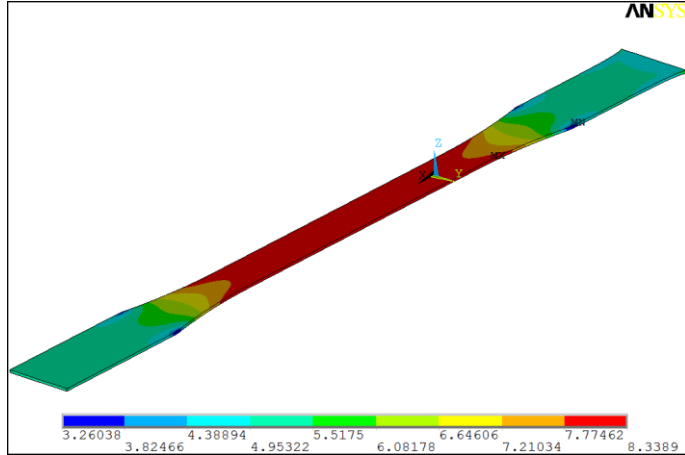


Figure 1.12: Longitudinal stress distribution

The homogenized tension values have been rated by the following formula

$$\langle \sigma_L \rangle = \bar{\sigma}_L = \frac{1}{\sum_{i=1}^n v_i} \sum_{i=1}^n v_i \cdot \sigma_{Li} \quad (1.21)$$

Where v_i and σ_{Li} represent the i -ith element's volume and longitudinal tension, respectively.

By this way, it's been possible to reproduce the stress-strain curves in the considered strain range, in the three different imposed uniaxial load conditions.

The following graphs shows the FEM analysis results, obtained by the activation of either geometrical non-linearity condition (big displacement, and strains – in red) and linear one (green), compared to the related experimental curves (blue.) In particular, the Figures 13, 14 and 15 show that results in the respective cases of uniaxial traction in the longitudinal, crosswise and 45° diagonal direction.

It's possible to point out from this curves obtained from the numerical non-linear simulations and from the experimentally obtained ones that all of them show nearly constant stress-shift compared to the strain, due to the heavily non-linear behavior of the stress-strain profiles in the first strain range (0-10%). Indeed, that difference is completely recoverable if the same FEM simulations are made entering an input pre-stress that atones material's micro-structural rearrangement.. By this way it's possible to find out a very good fitting of numerical results with experimental ones, as shown in the Figures 16, 17 and 18 for the three different examined cases.

Finally, it's important to put in evidence that –as it results from the green curves in the Figures 13–14 and 15, it's impossible to ignore the big displacement and strain's condition: the linearization of Green-Lagrange tensor implies a stress increase than the

nominal one experimentally measured and thus a tension overrate, increasing as the sample's strain does.

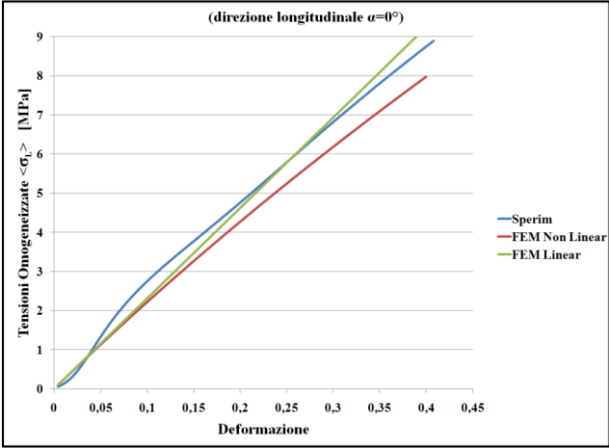


Figure 1.13

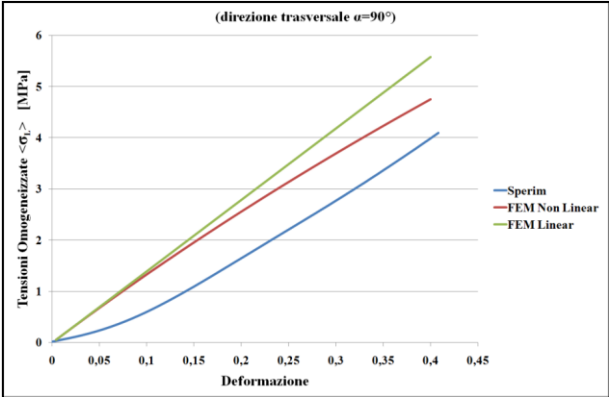


Figure 1.14

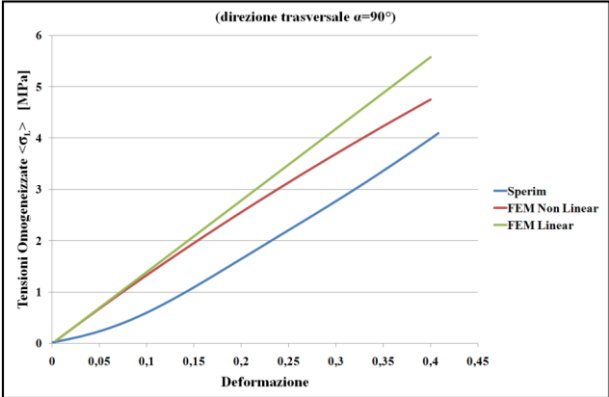


Figure 1.15

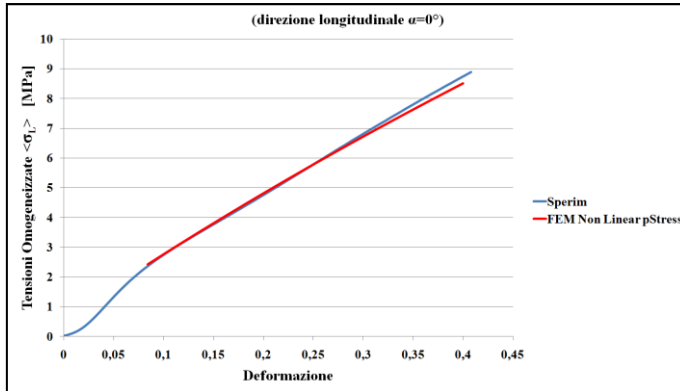


Figure 1.16

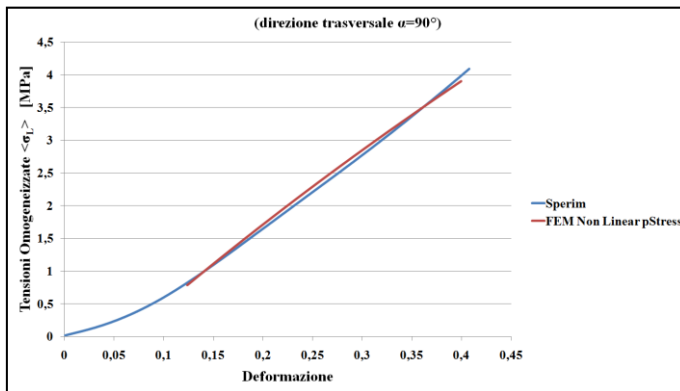


Figure 1.17

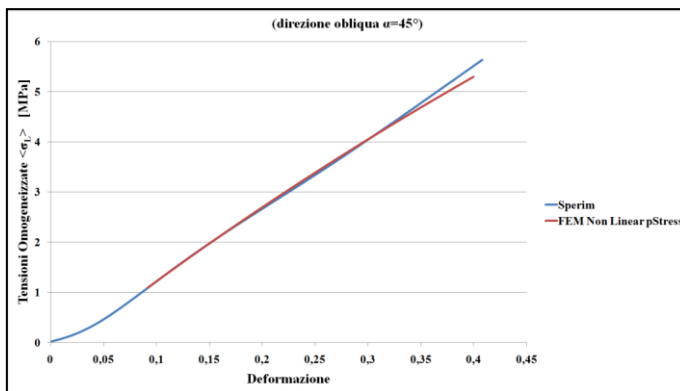


Figure 1.18

Anisotropic models in finite elasticity: specialization in the Pannel® case

Stress-strain tests for hyperelastic materials

Let's assume a reference configuration Ω_0 of a continuum in *stress-free conditions*.

The strain can be described by the following function:

$$\chi : \Omega_0 \rightarrow \mathbb{R}^3, \quad \mathbf{X} \in \Omega_0 \rightarrow \mathbf{x} = \chi(\mathbf{X}) \in \Omega$$

Where \mathbf{X} is a general material point in the undeformed configuration of the solid, and \mathbf{x} represents the same material point in the deformed, or current, configuration, Ω . The transformation is regulated by the strain gradient

$$\mathbf{F}(\mathbf{X}) = \frac{\partial \chi}{\partial \mathbf{X}}, \quad J = \det \mathbf{F}(\mathbf{X}) > 0 \quad (1.22)$$

Using the Cauchy-Green right tensor

$$\mathbf{C} = \mathbf{F}^T \mathbf{F} \quad (1.23)$$

It's possible to obtain the expression of the Green-Lagrange strain tensor as follows

$$2\mathbf{E} = (\mathbf{C} - \mathbf{I}) \quad (1.24)$$

Where \mathbf{I} is the second order identity tensor. In the main reference system, it is also obtained that:

$$c_{ii} = 2e_{ii} + 1 = \lambda_i^2, \quad c_{ij} = [\mathbf{C}]_{ij}, \quad e_{ij} = [\mathbf{E}]_{ij} \quad (1.25)$$

where λ_i are the main *stretches*, whose physical meaning allows to deduce the expression of the corresponding strain engineering components:

$$\varepsilon_i = \lambda_i - 1 = l_i l_{i0}^{-1} - 1 \quad (1.26)$$

l_i and l_{i0} being a material fiber's lengths, measured in the i-ith direction respectively in the deformed configuration and in the starting one.

Once defined the continuum kinematics by the different strain measures (1.24), (1.25), (1.26), it is possible to obtain the stress \mathbf{S} postulating the existence of a strains' potential, and then introducing Helmholtz free energy in the following form

$$\Psi = \Psi(\mathbf{E}, \mathbf{M}_n) = \Psi(\mathbf{E}, \mathbf{M}_1, \dots, \mathbf{M}_N), \quad n \in \mathbb{N} \quad (1.27)$$

where

$$\mathbf{M}_n = \mathbf{m}_n \otimes \mathbf{m}_n \quad (1.28)$$

Represents a second order symmetric tensor and \mathbf{m}_n is the general unit vector defining the n microstructure's orientation in charge of the eventual material's macroscopic anisotropy. By this way, the strain tensor –Piola-Kirchhoff second tensor– is univocally determined by the relationship:

$$\mathbf{S} = \frac{\partial \Psi}{\partial \mathbf{E}} \quad (1.29)$$

The equations (1.24), (1.27) and (1.29) define an hyperelastic material, and the relationship (36) defines the tensor variable's form that determines in turn the means' anisotropy.

Explicit definition of Helmholtz' free energy for orthotropic hyperelastic case

Pannel[®] tissue, as a consequence of several chemical-physical and production processes, shows a heavily anisotropic behavior, related to a substantial orthotropic, as shown by the uniaxial stress tests and, in particular, by the stress-strain curves experimentally obtained (Figure 2).

Referring to the tensor \mathbf{M}_n form (1.28) and assuming the presence of two micro-structural fibers statically directed in order to be mutually orthogonal Figure 19

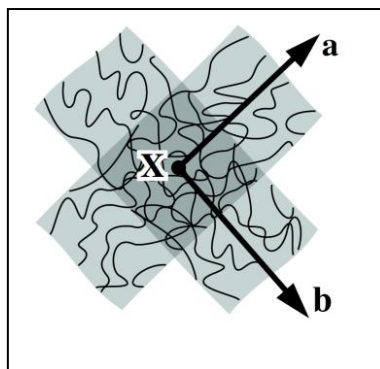


Figure 1.19

it's possible to reduce the tensor variables' number to just two, as follows:

$$\mathbf{M}_1 \equiv \mathbf{M}^{\parallel} = \mathbf{a} \otimes \mathbf{a}, \quad \mathbf{M}_2 \equiv \mathbf{M}^{\perp} = \mathbf{b} \otimes \mathbf{b} \quad (1.30)$$

Where

$$\mathbf{a} = [\cos \alpha, \sin \alpha, 0]^T, \quad \mathbf{b} = [\cos \beta, \sin \beta, 0]^T, \quad \beta = \alpha + \pi/2$$

And α represents the general inclination that the first fiber family angles with the longitudinal tissue axis (roll-unrolling direction), assumed equal to zero for the considered case.

The independence on referring system required by the strain energy density Ψ , leads to narrow the functional form (1.27) to the isotropic function form of the string tensor \mathbf{E} and of the two micro-structural tensor \mathbf{M}^{\parallel} and \mathbf{M}^{\perp} , thus considering variable the following usually invariant quantities

$$I_1^{\parallel} = \mathbf{C} : \mathbf{M}^{\parallel}, \quad I_2^{\parallel} = \mathbf{C}^2 : \mathbf{M}^{\parallel}, \quad I_1^{\perp} = \mathbf{C} : \mathbf{M}^{\perp}, \quad I_2^{\perp} = \mathbf{C}^2 : \mathbf{M}^{\perp} \quad (1.31)$$

Assuming polynomial a Helmholtz' free energy structure in the invariants (1.31) and limiting to quadratic and cubic terms (*Gasser and Holzapfel, 2000; Holzapfel et al., 2000*), it results:

$$\begin{aligned} \Psi(I_1^{\parallel}, I_2^{\parallel}, I_1^{\perp}, I_2^{\perp}) = & k_1(1 - I_1^{\parallel})^2 + k_2(1 - I_1^{\parallel}) \times (1 - I_2^{\parallel}) + \\ & + k_3(1 - I_1^{\perp})^2 + k_4(1 - I_1^{\perp}) \times (1 - I_2^{\perp}) + k_5(1 - I_1^{\parallel}) \times (1 - I_1^{\perp}) \end{aligned} \quad (1.32)$$

Where k_i are parameters, of the same dimensions as tensions', experimentally determinable.

Stress-strain engineering curves' analytic determination for uniaxial stress tests in longitudinal and crosswise direction.

In order to establish the value of k_i parameters in the (1.32) for Pannel[®] tissue, it is necessary to refer to the stress-strain curves experimentally derived from uniaxial stress tests in longitudinal and crosswise direction, considering the whole considered (engineering) string range (Figure.2)

In order to do it, referring to a Cartesian reference system $\{0, x_1, x_2, x_3\}$, matching either the main symmetry reference system and the stress-strain one, in plane stress case, reconstruct the stress state by utilizing the equation (1.29) and the free energy expression (1.32), remembering from (1.24) that $\mathbf{E} = (\mathbf{C} - \mathbf{I})/2$:

$$\begin{aligned}
\sigma_{11} &= \frac{\partial \Psi}{\partial e_{11}} = 8k_1 e_{11} + 2k_2 \{4e_{11}(1+2e_{11}) - [1 - (1+2e_{11})^2]\} + 4k_5 e_{22} \\
\sigma_{22} &= \frac{\partial \Psi}{\partial e_{22}} = 8k_3 e_{22} + 2k_4 \{4e_{22}(1+2e_{22}) - [1 - (1+2e_{22})^2]\} + 4k_5 e_{11} \\
\sigma_{33} &= \frac{\partial \Psi}{\partial e_{33}} = 0
\end{aligned} \tag{1.33}$$

Where $\sigma_{ii} = [S]_{ii}$ are the main components of the stress tensor and the direction x_3 is assumed as orthogonal to the stress plane. In order to obtain the analytic relationship for the two uniaxial stress cases in longitudinal direction (along x_1 axis) and crosswise direction (along x_2 axis) related to the experimental tests, it's necessary to rate the relationship between the main strain components e_{11} e_{22} that annul the σ_{22} tension, in the case of uniaxial stress in x_1 direction, and complementarily the tension σ_{11} in the case of uniaxial stress in x_1 direction. Which involves the following algebraic equations (derived from (1.33)) to be solved:

$$\begin{aligned}
\sigma_{22} = 0 &\Rightarrow e_{22} = \frac{-(k_3 + 2k_4) + \sqrt{(k_3 + 2k_4)^2 - 6k_4 k_5 e_{11}}}{6k_4} \\
\sigma_{11} = 0 &\Rightarrow e_{11} = \frac{-(k_1 + 2k_2) + \sqrt{(k_1 + 2k_2)^2 - 6k_2 k_5 e_{22}}}{6k_2}
\end{aligned} \tag{1.34}$$

Substituting the first of (1.34) to the σ_{11} stress expression in (1.33) and twice the second of (1.34) to σ_{22} in (1.33), stress-strain relationships $\sigma_L - \varepsilon_L$ and $\sigma_T - \varepsilon_T$ are obtained respectively for the longitudinal and crosswise case as follows

$$\begin{aligned}
\sigma_L &= \frac{72k_2 k_4 e_L^2 + 24k_4 (k_1 + 2k_2) e_L + 2k_5 [-(k_3 + 2k_4) + \sqrt{(k_3 + 2k_4)^2 - 6k_4 k_5 e_L}]}{3k_4} \\
\sigma_T &= \frac{72k_2 k_4 e_T^2 + 24k_2 (k_3 + 2k_4) e_T + 2k_5 [-(k_1 + 2k_2) + \sqrt{(k_1 + 2k_2)^2 - 6k_2 k_5 e_T}]}{3k_4}
\end{aligned} \tag{1.35}$$

Where, from (1.25) and (1.26), the Green-Lagrange strain components $e_L \equiv e_{11}(\sigma_{22} = 0)$ and $e_T \equiv e_{22}(\sigma_{11} = 0)$ are linked to the related engineering strain components' expressions ε_L and ε_T by the relationships:

$$e_L = \frac{(1 + \varepsilon_L)^2 - 1}{2}, \quad e_T = \frac{(1 + \varepsilon_T)^2 - 1}{2} \quad (1.36)$$

Calibration of Helmholtz hyperelastic model on the Pannel[®] tissue

The analytical form of stress-strain laws $\sigma_L - \varepsilon_L$ and $\sigma_T - \varepsilon_T$ for hyperelastic materials can be obtained to replacing the equations (1.36) into the relations (1.35). The k_i parameters of Helmholtz's model can be calculated through a fitting procedure on the experimental results, obtaining the data reported in the table below:

Hyperelastic parameters of analytical model (Orthotropic hyperelastic model)					
k_i [MPa]	k_1	k_2	k_3	k_4	k_5
	3.895	-0.465	0.597	0.115	0.016

In the figure 20 are shown both the analytical curves (solid line) and the output of experimental results (dots) of the uniaxial stress-strain test, along longitudinal and transversal directions respectively. It's possible to deduce the good agreement of theoretical predictions with the results of laboratory.

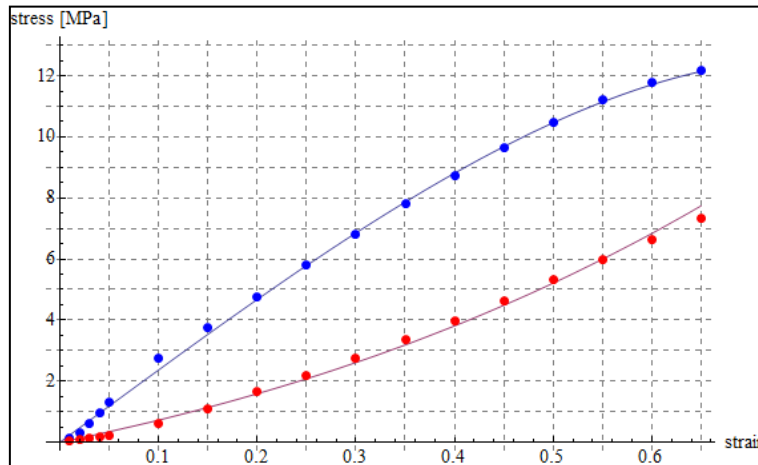


Figure 1.20: analytical curves (solid line) and the output of experimental results (dots)

Uniaxial tests simulation by Finite Elements analysis under anisotropic hyperelasticity and high strains.

Conclusions

The first part of this chapter focused on the construction of a linear elastic orthotropic model for the understanding of the mechanical behavior of tissue Pannel[®].

The linear and orthotropic hypothesis have been discussed in the opening paragraphs and there were related to the experimental result into the range of deformation of practical interest that is the high deformation range 10% – 50% .

The numerical simulations are carried out by using a Finite Element code (ANSYS[®]), with which it was possible to validate the theoretical model and to quantify the affect of the non-linear material behavior, in the tensile uniaxial tests. The second part of chapter describe the definition of hyperelastic behavior to modeling the stress-strain response of Pannel[®]. This model is derived from the framework of the theory of nonlinear elasticity (Finite Hyperelasticity). In particular, starting with the free energy of Helmholtz, was found the formal structure of the *strain energy density* as a function of the invariants both of the Green-Lagrange tensor than the microstructural tensor. The latter deriving from a generalization of the *Holzapfel-Gasser Ogden mode*. The parameter calibration were made from the experimental stress-strain curves, showing a good approximation between experimental and analytical results.

References

- ANSYS 10.0 User's Manual (2009) ANSYS, Inc. Canonsburg, PA 15317, USA.
- ASTM International Committee (2003) Composite Materials: Testing and Design. Danvers MA
- Gasser TC and Holzapfel GA (2000) Rate-independent elastoplastic constitutive modeling of biological soft tissues: Part I. Continuum basis, algorithmic formulation and finite element implementation. Int. J. Solids and Structures
- Holzapfel GA, Gasser TC, and Ogden RW. (2000) A new constitutive framework for arterial wall mechanics and a comparative study of material models. J. Elasticity
- Jones RM (1999) Mechanics of Composite Materials. Taylor e Francis
- Sadd, MH (2005), Elasticity: Theory, Applications and Numerics, Elsevier Butterworth–Heinemann , Burlington, MA

Equation Chapter (Next) Section 1

CHAPTER II

FEM MULTIPHYSIC APPROACHES ON THE BIOMECHANICS OF CORNEAL TISSUE

Introduction

Over the past decade, surgical techniques based on excimer lasers have been extensively used for treatment of refractive errors in human eyes. Several procedures (LASIK, PRK, LASEK, etc) have been developed to correct nearsightedness, farsightedness and astigmatism by removing thin layers of biologic tissue, thus modifying the surface curvature of the cornea. These techniques have advanced rapidly and laser in situ keratomileusis (LASIK) surgery has emerged as one of the most commonly performed procedures. In particular, with the aid of automated control by computers, the LASIK has become reliable and its outcome predictable. However, the disadvantages of these surgical procedures reside in the fact that intervention location is at the corneal centre and therefore the operation zone is on the visual axis. This may affect visual acuity with the possibility of night vision problems including halos, starbursts, and other undesirable phenomena. Moreover, if the surgery fails the laser ablation of corneal tissue may generate irreversible effects and it can be extremely difficult to compensate for the loss.

Consequently, refractive treatments operating on peripheral cornea such as Conductive Keratoplasty (CK) and Intra-Corneal Ring (ICR) have gradually attracted much attention, in particular for the correction of farsightedness, which is far more problematic than nearsightedness because a steepening versus a flattening of corneal surface is required. From a technical standpoint, the Conductive Keratoplasty is based on the delivery of a precise amount of radiofrequency energy through a probe inserted into the stromal tissue.

CK generates heat in the cornea because stromal tissue provides resistance to the flow of the current, which results in controlled heating and collagen coagulation. The process is self-limiting because resistance to the flow of the current increases with the increasing dehydration of collagen and the CK treatment spots, which may vary from eight to thirty-two according to the degree of correction required, reach a temperature consistent with optimal shrinkage. A cinching effect is thus obtained that increases the curvature of the central cornea, yielding the desired result. Although the procedure is

far less invasive and risky than ablative ones, the postoperative follow-up shows that the initial degree of refractive correction tends to decrease of 20% in 24 months' time (McDonald et al. 2005; Esquenazi et al. 2006)) so that the predictability of the outcome cannot be considered completely satisfactory.

In order to shed some extra light on the reasons of this regression and to help to understand the still unclear mechanisms responsible of the phenomenon, the present study proposes a Finite Element Method (FEM) based numerical simulation of the mechanical response of the cornea to CK, with the aim of determining the role played by some key geometrical and mechanical factors.

Simulations of surgical procedures by means of numerical approaches have been commonly adopted to understand the tissue response and to develop new surgical techniques to varying degrees of success. To this scope, the FEM has been employed to simulate the incisions for astigmatism correction and evaluate the depth, length and position of each incision (Lanchares et al. 2008). By following a similar approach, Pandolfi et al. (Pandolfi et al. 2006, 2009) simulated the surgical outcome on myopic and astigmatic eyes, evaluating the dioptric power in the postoperative. However, to the best of authors' knowledge, no previous FE models and analyses have been devoted to CK and to the influence on the refractive correction of both the viscoelastic properties of the cornea and of the induced stress status. Additionally, since surgical simulations must rely on a suitable representation of the mechanical response of soft tissues subject to surgical manipulations, to achieve a meaningful reproduction of the phenomena pertinent finite element models need to be employed. In fact, validating these models for specific tissues still remains a challenge and in the present work carefully conducted human cornea tests (Zeng et al. 2001) have been chosen to corroborate the elastic and the viscoelastic constitutive laws.

The chapter is organised as follows: In the first part of chapter, a FE modelling of the cornea, accounting for its viscoelastic behaviour, is accurately set up according to the available experimental data in the current literature; then, by introducing suitable boundary conditions and prescribing heat sources at the intervention spots, a steady-state thermo-mechanical simulation of the Conductive Keratoplasty intervention is carried out and the numerical results are validated with respect to the standard clinical nomograms; successively, the evolution of the obtained correction is evaluated over time with respect to the viscoelastic properties of the corneal tissue and a comparison between the resulting stress field and the one normally present on account of the Intra-Ocular pressure (IOP) is performed.

In the second part, in order to simulate the thermal behavior of corneal tissue during the heating process, and subsequently viscoelastic mechanical response of structures, a coupled thermo-mechanical transient analysis has developed.

In addition, with reference to the currently adopted surgical nomograms for refractive corrections ranging from 0.75 to 2.25 Diopters, a sensitivity analysis is performed with the aim of evaluating the capability of the computational model to predict the expected clinical results. Thus, interventions involving eight, sixteen or twentyfour spots are analysed.

Material and Methods

The biomechanics of the human cornea

The human cornea is a highly porous soft tissue filled by biological fluids that protects the internal layers of eye, keeps its shape and conveys the light rays to the retina. Its thickness ranges from 1 to 0.8 mm from the cornea-sclera junction to the centre, 80% of its mass being constituted by water. From an anatomic-histological point of view the cornea is made of five layers: the epithelium, the Bowman's membrane, the stromal tissue, the Descemet's membrane and the endothelium (Pinsky and Datye 1991). The corneal stroma represents 90% of the whole cornea and has an average thickness of 600 μm (about 550 μm and 650 μm in correspondence of the apex and at the limbo, respectively). It is constituted of about 300-500 parallel lamellae, made of collagen fibrils soaked in a waterproteoglycans substance: the presence of these constituents and their percentages confer to the whole structure a marked viscoelastic behavior, while the different orientation of fibrils suggests a local anisotropy (Newton and Meek 1998; Nguyen et al. 2008).

In the last years, many efforts have been made to understand the biomechanics of the corneal tissue and several experimental tests have been conducted both in the short and in the long-term ranges such as inflation, tensile, creep and stress relaxation tests. A number of numerical simulations have also been carried out and several ad hoc equations have been used to describe the response of different corneal tissues (Fung 1993; Zeng et al. 2001). Inflation tests have been used to evaluate the change of stiffness with increasing intraocular pressure and the creep behavior, while a hyperelastic response has been related to the age of corneal tissue (Elsheikh 2008). In several cases animal corneas have been employed, given the difficulty in obtaining human corneas (Hoeltzel et al. 1992). For this reason, the differences in mechanical properties of human and porcine corneae have been analysed and similar stress-strain relationship has been found, albeit the long-term stress-relaxation behavior can be markedly different (Zeng et al. 2001). Specific inflation tests have been performed on

corneal porcine specimens subject to internal pressure increases, highlighting a typical soft tissue nonlinear behaviour, that is a matrix-regulated phase followed by a collagen-regulated phase (Anderson et al. 2004).

Many studies have been aimed to derive the mechanical behavior of cornea directly from its stromal structure, each lamella being formed of collagen fibrils embedded within extracellular matrix rich in proteoglycans, glycoproteins and keratocytes (Boote et al. 2005). However, the hierarchical structure of the cornea at different scales, a fact common to many biological tissues, makes the development of reliable numerical models difficult and different approaches have been proposed in literature. In many cases corneal tissue has been assumed to behave as a nearly isotropic incompressible material with Poisson's ratio about $\frac{1}{2}$. Some authors have attempted to describe the human eye as an exponentially stiffening membrane and made reference to a nonlinear elastic and isotropic material (Fernández et al. 2006; Xie et al. 2008). Hyperelastic constitutive laws, derived from inflation tests on porcine cornea specimens, have been also adopted in some numerical models of cornea (Anderson et al. 2004) and others authors have considered an anisotropic corneal micro-structure on account of the lamellae of the stroma. In particular, Li et al. (2006) assumed the cornea as made of a composite material and invoked constitutive equations for laminated composite shells, with the lamellae presenting a random orientation with gaussian distribution. As a matter of fact, a wide-angle X-ray scattering study had previously confirmed the anisotropic arrangement of the lamellae (Meek et al. 1987) and subsequent research works, again based on X-ray scatter have recently revealed that in central zone the fibrils are concentrated in the 45° sectors along the superior-inferior and nasal-temporal directions (Boote et al. 2005; Meek et al. 2009).

Additional investigations (Newton and Meek 1998) have established the presence of a circumferential annulus of collagen fibrils at the cornea-sclera interface and microstructural models exploiting these results have been subsequently implemented in FE analyses through the definition of two preferred material directions and by adopting energy approaches to model the collagen fibers-matrix composite behavior (Lanchares et al. 2008; Pandolfi et al. 2006; Pinsky et al. 2005; Nguyen et al. 2008). Very recently, some authors (Grytz and Meschke 2009a) have proposed an innovative strategy to model the physiological network of collagen fibrils at the cornea-sclera junction and developed an algorithm to predict the re-orientation based remodeling of crimped collagen tissue. Their results have shown effective matching both with experimental data from uniaxial test on rat tail tendons (Grytz and Meschke 2009b) and with experimental data from strip extensometry on porcine cornea (Anderson et al. 2004). Having examined all these previous studies and given the

chief scope of the present investigation, i.e. the analysis of the long term stability of the obtained correction, in order to focus the attention on the key parameters in a suitable and not gratuitous complicated mechanical modelling, in the present work the corneal tissue has been assumed to behave as a nearly isotropic viscoelastic incompressible material. This choice has been validated with reference to carefully conducted tests on human corneae (Zeng et al. 2001) and with the comparison of the FE results to orbscan corneal topography images (McDonald et al 2002).

From a geometrical point of view, the cornea has been modelled in several ways and approaches modelling the global eye ball (Crouch 2005), the sole cornea (Anderson et al. 2004; Xie 2008), assemblies of cornea, limbus and sclera (Lancharés et al. 2008) have all been pursued. Spherical, ellipsoidal or pseudospherical shapes, with different internal and external radii, have been proposed for cornea geometry (Fernández et al. 2006; Pinsky et al. 1991; Bryant et al. 1996). In particular Anderson et al. (2004) modelled both the whole eye and the sole cornea to evaluate the effects of some parameters related to the IOP and these results have been successively used on a spherical corneal-only FE model, to assess the IOPG (Goldmann Intra-Ocular Pressure) measures.

Pandolfi et al. (Pandolfi et al. 2009) modelled the cornea by introducing ellipsoidal curves in order to simulate the laser surgery outcome on myopic and astigmatic eyes. Fernández et al. (2006), employed a two-dimensional finite element, while three-dimensional FE models of the front part of the human eye have been created to simulate astigmatism correction by corneal incision (Lancharés 2008), where cornea, limbus and sclera have been involved and the eye model has been generated by assuming, as done by several other authors, symmetry with respect to the optical axis.

Viscoelastic characterization of the corneal tissue

It is well-known that, on account of the presence of solid and fluid constituents at the micro-scale level, many biological soft tissues exhibit an overall macroscopic viscoelastic or poro-viscoelastic mechanical behavior (Fung 1993; Cowin and Doty 2007). In living tissues, this material time-dependent response can interfere with biological time-dependent remodelling, growth and morphogenesis processes, which alter the tissue structure modifying its mechanical features over time (Cowin and Doty 2007). The actual overlapping of material and biological responses depends on the ratio between the characteristic times by which the two phenomena evolve, say stress relaxation and tissue micro-structure changes. As a consequence, from the mechanical point of view, a preliminary evaluation is needed for assessing the possibility of separating these effects. With the aim of investigating the role of corneal

viscoelasticity on refractive correction after CK operations, it is possible to make reference to mechanical models (Nguyen et al. 2008) essentially based on the Maxwell and the Kelvin-Voigt elementary ones (**Fig.2.1**).

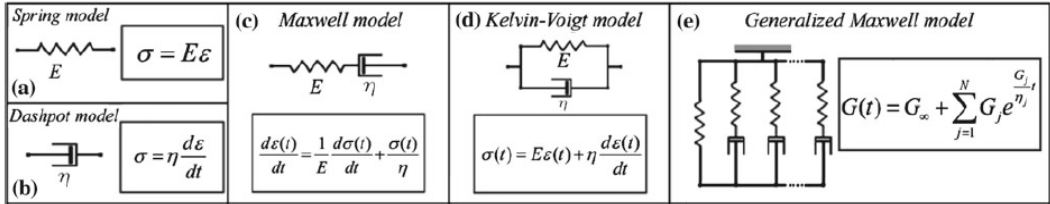


Fig. 2.1 Basic constitutive models equation

According to these models, any viscoelastic behavior of a given material results from a suitable combination of serial and parallel springs and dashpots, characterized by different Young moduli, E , and viscosities, η , respectively. These models, along with the well-known corresponding equations, are shown in Fig.2.1 where σ is the stress, ε the strain and t the time.

The most commonly adopted viscoelastic model is constituted by the so-called generalized Maxwell (or Maxwell-Wiechert) model (see Fig. 2.1), where the time dependent behavior of the material is accounted through a special mathematical expression, the Prony series, i.e.:

$$G(t) = G_{\infty} + \sum_{j=1}^N G_j e^{-\frac{G_j}{\eta_j} t} \quad (2.1)$$

where G represents the Lamè shear modulus (Chen 2000).

As stated in the previous Section, in order to avoid unnecessary complications, within the scope of the present investigation the corneal tissue has been considered as viscoelastic and isotropic and obeying to the stress-relaxation curve derived from available experimental results (Zeng et al. 2001), as shown in Fig. 2.2.

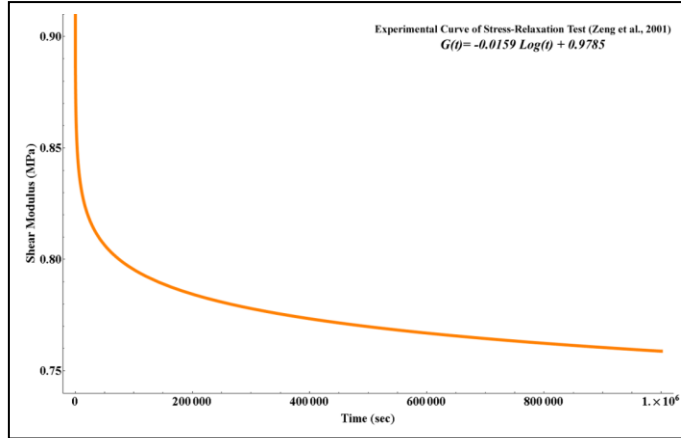


Fig. 2.2 Typical stress-relaxation curve of human cornea from experimental data

On the basis of these available experimental results, the time period of analysis has been extended to about 11 days after the surgery. The procedure followed to evaluate the *Prony* coefficients G_j, τ_j and K_j, τ_j for shear and bulk moduli is summarized in the flow-chart of Fig. 2.3.

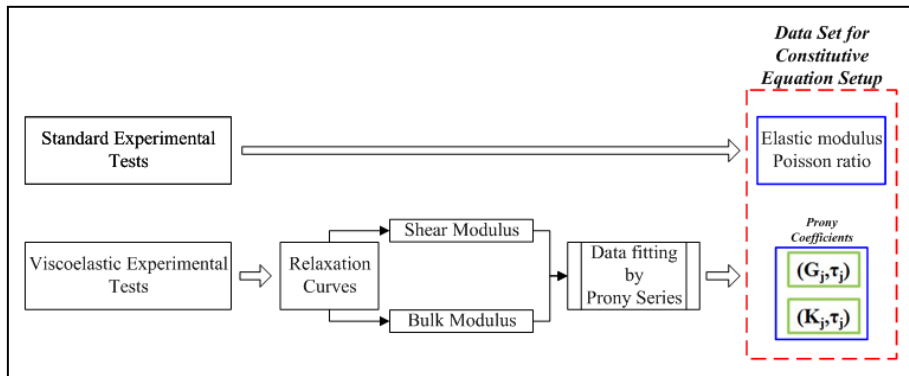


Fig.3 Set-up of data set for modelling the viscoelastic behavior in ANSYS®

The numerical analyses have been performed with the aid of the Finite Element based commercial package ANSYS® (ANSYS 2009), whose dataset for viscoelastic materials is built by entering the couples of Prony coefficients and Young modulus and Poisson ratio, in case of isotropy related to shear and bulk moduli by means of the classical formulae

$$2G(t) = E \times (1 + \nu)^{-1} \Big|_{t=0} \quad (2.2)$$

and

$$3K(t) = E \times (1 - 2\nu)^{-1} \quad (2.3)$$

with $\nu = 0.499$ to simulate a nearly incompressible material. The couples of Prony coefficients have been derived by means of a least square technique, employed to fit the experimental curve. Table 1 collects the input values in the FE code.

$G(t) = \sum_{j=1}^n G_j \text{Exp}\left(-t/\tau_j\right)$			$K(t) = \sum_{j=1}^n K_j \text{Exp}\left(-t/\tau_j\right)$		
j	G_j	τ_j	j	K_j	τ_j
1	0.760459		1	37.8176	
2	-16.3482	49519.7	2	655.507	89600.8
3	12.1045	35238.8	3	-1608.11	77392.2
4	18.2807	69056.4	4	-697.578	23398.6
5	1.56495	19267.7	5	-1725.99	43953.2
6	-15.774	91020.1	6	-2.12441	12937.6
7	6.55643	107265	7	193	17955.6
8	0.0545391	507.78	8	1285.31	31664.7
9	-6.2817	25913.2	9	1905.62	60049.1
Shear Modulus			Bulk Modulus		

Table 1 Prony coefficients

In order to validate the viscoelastic constitutive relationships prior to the analyses, the FE constitutive behavior has been checked against the experimental expression by Zeng (2001) by means of a specific procedure developed to simulate stress-relaxation tests on a benchmark cubic specimen under pure shear.

The conductive keratoplasty

As anticipated in the Introduction, the conductive keratoplasty is a non-ablative procedure based on the delivery of a precise amount of RF energy through a finely tipped stainless steel probe inserted into the peripheral cornea at premarked spots encircling the cornea outside the visual axis. The instrument tip pierces into about 80% of the corneal depth (McDonald 2005; Hersh 2005) and produces a rather homogenous and uniform cylinder of scar tissue.

More precisely, the analysis of the histology of a pig eye one week after CK treatment shows at each treatment spot a cylindrical footprint that extends to approximately 80% of the depth of midperipheral cornea (McDonald 2005). The treatment spots in the histopathological images of human corneae appear somewhat more homogenous and deeper (approximately 500 μm) than the cylindrical thermal footprint (Naoumidi et al. 2005), but it can be nevertheless related to this shape. The new configuration is accompanied by contraction (shrinkage) of collagen that changes the mechanical behaviour of the tissue. The intervention produces a “cinching” effect that decreases the radius of curvature of the central region of the cornea, depending on the number of

spots treated, by the number of rings treated and by their diameter (McDonald et al. 2002; Hersh 2005). This is shown in the scheme of Fig. 2.4, where D stands for dioptres. The consistency of the procedure relies upon several factors: the probe penetrates into the cornea and cannot pierce it, since an insulated Teflon-coated governor prevents a deeper treatment.

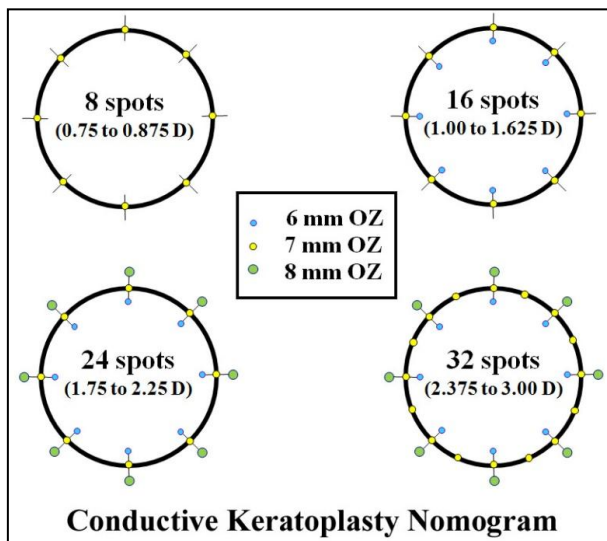


Fig. 2.4

Additionally, heat is not applied directly to the surface of the cornea but is generated within the tissue on account of the resistance of the stromal collagen fibres. The tissue is raised to a certain temperature and kept so for a preset time, which causes the collagen fibres to shrink without totally denaturing the protein. Finally, the process is self-limiting. In fact, collagen exists in a triple helical form in which the peptide chains are stabilized by hydrogen bonds (Cowin and Doty 2007). Heat-induced denaturation of collagen is an irreversible rate-process wherein the native helical structure is transformed into a more random, coiled structure. The corneal collagen denaturation kinetics is known to depend highly on the temperature/time history (Brinkmann et al. 2000) and the potential to achieve maximal collagen denaturation is dependent on the type of target tissue (based on collagen content, density, fibre orientation, etc.), on the temperature and on the time (duration of treatment). Once maximal collagen denaturation has been achieved at any given target temperature, increasing the treatment time does not result in further collagen denaturation (Wall et al. 1999), and in this sense the CK process is completely selflimiting.

FE modeling and analysis

With the aim of analysing the post-operative evolution of the CK surgery, a suitable FE model has been created. On account of the findings from the previously cited works regarding the human eye, in the present study it has been judged that the modelling of the sole cornea would have sufficed to the scopes of the analysis. The shape of the cornea was generated by means of a rotation about the optical axis z of a corneal profile with varying thickness, following the path by Fernández et al. (2006). To this purpose an ad hoc ANSYS® procedure was developed and the solid model was successively meshed by means of 45,000 standard 8-nodes hexahedral elements and 53,557 nodes (Fig. 2.5) within a kinematically linear framework.

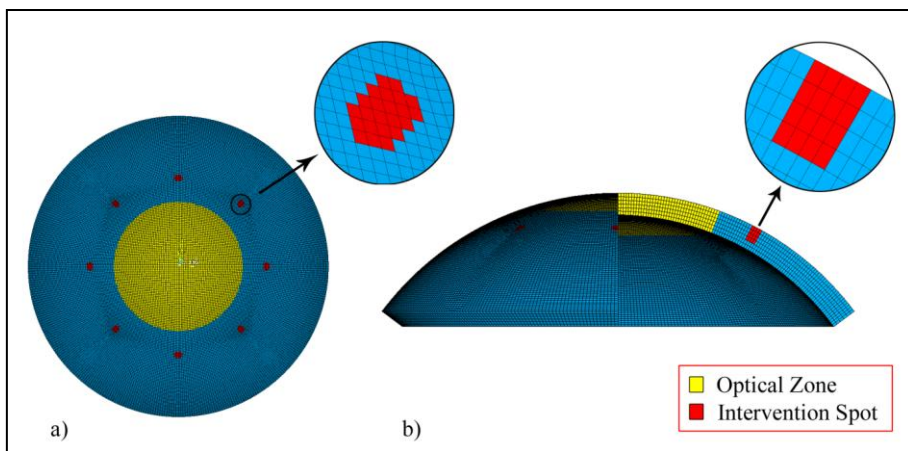


Fig. 2.5

In order to reduce the computational effort, only one quarter of the cornea was taken into consideration, relying upon appropriate boundary symmetry conditions on the x-y and the y-z planes (Fig. 2.6). The cornea-limbus transition (Elsheikh et al. 2006) was simulated by edge rollers inclined of about 37° with respect to the limbus plane, a value found appropriate by Anderson et al. (Anderson et al. 2004). Essentially, this means constraining a radial degree of freedom and preventing a circumferential expansion of the limbus. In fact, limbus is a quite rigid tissue and a circumferential expansion is not to be allowed.

In order to simulate accurately the CK surgical procedure and its subsequent effects, a geometry representing a pathological hyperopic condition of about 0.75 D, corresponding to an overall diopter power of about 50.27 D, was adopted (Lanchares et al. 2008). The reference configuration is the natural one, i.e. under IOP pressure. However, it must be pointed out that, despite its high flexural deformability, the membranal deformation of the cornea under IOP is not very significant, as shown both

by inflation tests (Elsheikh et al. 2008a) and FE models. In particular, Bryant and McDonnell (1996) evaluated different laws to describe the mechanical behaviour of corneal tissue by membrane inflation tests, increasing the IOP and varying its values in a fixed range and Pandolfi and Manganiello (2006) used their FE model to simulate the Bryant and McDonnell experiments, applying a uniform pressure to the internal surface of cornea, ranging from 0 to 30 mmHg.

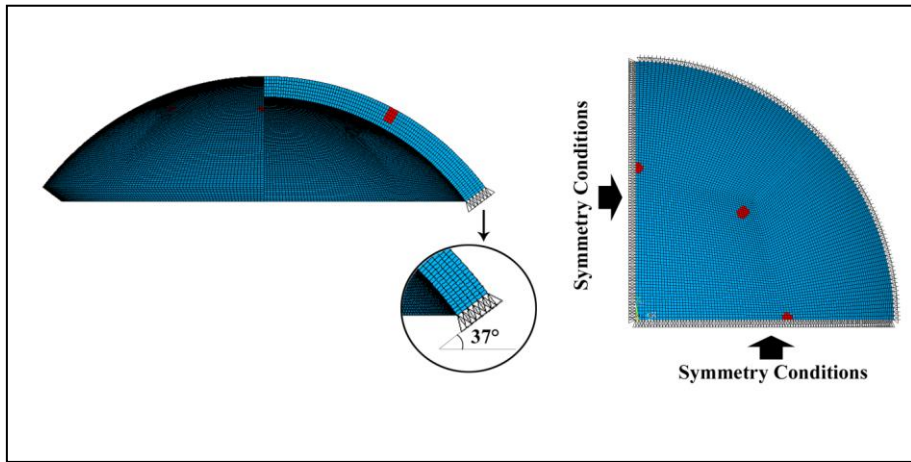


Fig.2.6

The thermal shrinking of collagen tissue has been replicated through an inelastic distortion applied to the elements at the intervention spots and kept constant. In this manner, an equivalent representation of the thermal lesions was achieved by means of an adequate setting of the distortions.

According to the CK nomogram used in surgical techniques, in the present study an annulus with eight intervention spots, which is normally employed for the correction of a defect ranging from 0.75 to 0.875 D (see Fig. 2.4) was first taken into consideration. Figures 2.5 and 2.6 show the position of the annulus and the symmetry conditions assumed for the FE model.

In order to pre-emptively estimate the magnitude of the displacements associated to the required steepening of central cornea, according to the number of points indicated in the nomogram, an analytical procedure along the line of reasoning of Wang et al. (2007) has been employed and the value of the fictitious thermal load has been established.

With reference to Fig. 2.7, say R_i the radius in the initial configuration. The relative dioptric power can be calculated by means of the Munnerlyn expression (Munnerlyn et al. 1988), i.e.

$$D_i \cong \frac{n-1}{R_i(x)} \quad (2.4)$$

where n is the corneal refractive index $n = 1.377$.

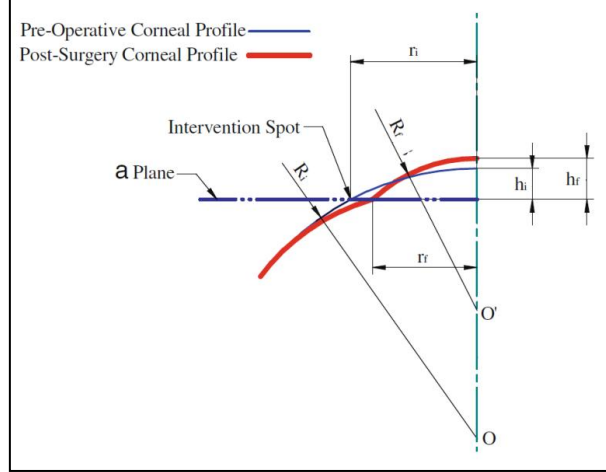


Fig.2.7 Pre- and Post-Operative corneal profiles

By considering the corneal caps above the α plane passing through the spots annulus before and after deformation, it is assumed that both are spherical and that their area remains the same, so that

$$S_{pre} = S_{post} \quad (2.5)$$

Where $S_{pre} = 2\pi R_i h_i$ and $S_{post} = 2\pi R_f h_f$

It follows that

$$h_f = h_i \frac{R_i}{R_f} \quad (2.6)$$

h_f being the height of the deformed spherical cup. In this expression R_f (radius of the deformed spherical cup) can be calculated by Eq. 2.4 by imposing $D_f = D_i + 0.875$ where 0.875 D is the upper bound of the corrected dioptric power following an eight-spots CK treatment and

$$h_i = R_i - \sqrt{R_i^2 - r_i^2} \quad (2.7)$$

The mean circumferential strain results

$$\bar{\varepsilon}_{\theta\theta} = \frac{C_f - C_i}{C_i} = \frac{2\pi(r_f - r_i)}{2\pi r_i} \quad (2.8)$$

where $r_f = R_f - \sqrt{R_f^2 - h_f^2}$

Since it can be set $C_f = C_i + 8L\varepsilon_{\theta\theta}$, where $\varepsilon_{\theta\theta}$ is the local strain at the elements representing the intervention spots, whose length is L , it follows

$$\varepsilon_{\theta\theta} = \frac{2\pi \bar{\varepsilon}_{\theta\theta} r_i}{8L} \quad (2.9)$$

So that the estimated value of the required thermal load, ΔT , is

$$\varepsilon_{\theta\theta} = \alpha_T \Delta T \quad (2.10)$$

where α_T is the thermal expansion coefficient.

According to the surgery, the footprint of the CK lesion in the modelled cornea has been extended to about 80% of its depth as shown in Fig. 2.8 where the stress field at a treatment spot in the FE model is compared to the image of the experimental readings in a pig corneal tissue.

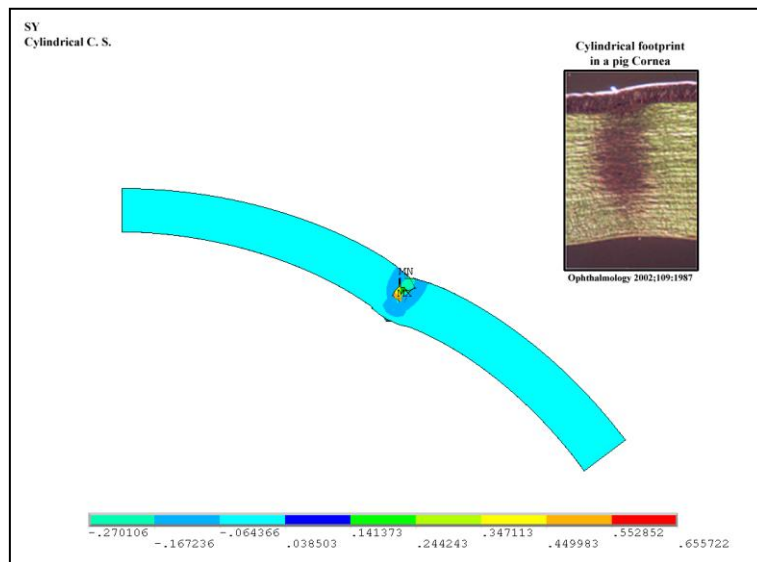


Fig.2.8

The changes in the cornea curvature and in the relative diopter power have been evaluated as follows. The displaced positions of the nodes in the visual zone (about 6 mm diameter) have been interpolated at each time step, i , by means of a best fitting process through the symbolic code MATHEMATICA[®] (Wolfram 2003), thus obtaining a profile function $P^{(i)}(r)$. Successively, the local curvature $C^{(i)}(r)$ and the mean curvature radius $\bar{R}^{(i)}$ of the selected zone have been evaluated through the following formulae

$$C^{(i)}(r) = \frac{\partial^2 P^{(i)}(r)}{\partial r^2} \left[1 + \left(\frac{\partial P^{(i)}(r)}{\partial r} \right)^2 \right]^{-\frac{3}{2}} \quad (2.11)$$

and

$$\bar{R}^{(i)} = \frac{1}{\Gamma} \int_0^\Gamma R^{(i)}(r) dr = \frac{1}{\Gamma} \int_0^\Gamma \frac{1}{C^{(i)}(r)} dr \quad (2.12)$$

where Γ is the span of the visual arc.

Successively, the resulting diopter power has been calculated using the Munnerlyn expression, Eq. 4.

Mechanical Results and discussion

Discussion of analysis outcomes

As stated before, the objective of the present study has been to investigate the post operative stability of the imposed dioptric correction and to this purpose first the effects of stress relaxation or creep phenomena around each intervention spot on account of the viscoelastic constitutive behavior of corneal tissue have been analysed. Both von Mises equivalent stresses and strains have been evaluated, as shown in picture below (**Fig. 9.**)

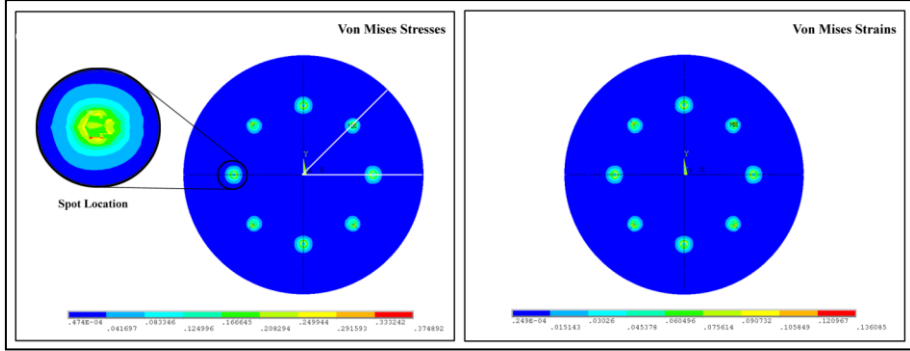


Fig. 2.9 Numerical results. von Mises equivalent stresses [MPa] (*left*) and strains (*right*)

For each time-step i of the non linear analyses, von Mises stresses and strains have been computed and their overall mean value has been then derived as follows

$$\bar{\sigma}^{(i)} = \frac{1}{\sum_{j=1}^N V_j} \sum_j^N \sigma_j^{(i)} V_j, \quad \bar{\varepsilon}^{(i)} = \frac{1}{\sum_{j=1}^N V_j} \sum_j^N \varepsilon_j^{(i)} V_j, \quad (2.13)$$

where N is the total number of elements over which the average values are calculated, i is the generic time-step, V_j represent the j -th volume element and $\sigma_j^{(i)}$ and $\varepsilon_j^{(i)}$ are the von Mises stresses and strain related to the j -th element, respectively.

In Fig. 2.10, top, a plot of the mean stress and strain intensity at 0.8 mm around the intervention spots versus time is shown, and a relaxation can be observed in the tissue, which confirms previous observations (Esquenazi et al. 2006). The evolution of Von Mises strains highlights first a swift decrease in value, followed by a slow increase given by the creep behaviour. These results suggest that the viscoelastic response of the cornea tissue, in conditions of stress relaxation, fades in a few days and does not contribute to the long term partial reversal of the imposed correction.

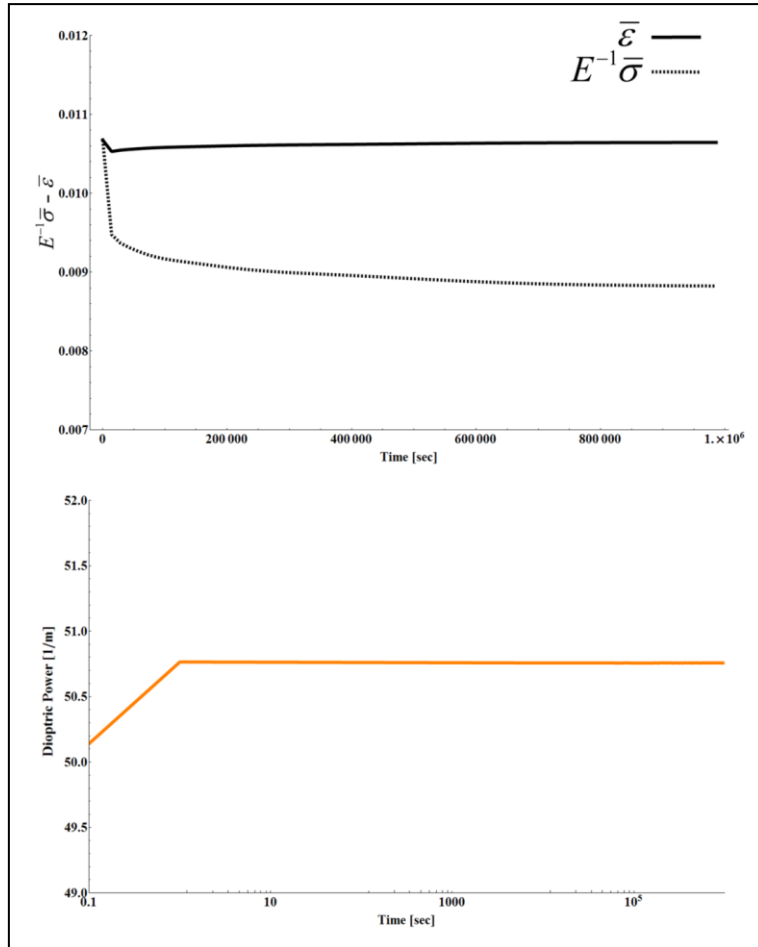


Fig. 2.10: Homogenized von Mises stresses and strains at the intervention spot versus time (*top*).
 Dioptric power versus time (*bottom*)

In Fig. 2.10, bottom, a plot of the dioptric power versus time is also shown and indicates that it tends to increase in the immediate post-operative period and successively stabilizes at a constant value. This finding reveals that in the long term the curvature of the visual zone is substantially unaffected by the relaxation of the corneal tissue and that in any case the initial trend due to the creep acts in the opposite way of the observed average decrement of 20% in 24 months' time. The result gives also reason from a mechanical standpoint for the immediate corneal steepening in rabbits corneae observed after CK by Esquenazi et al. (2006).

The attention has then been focused on the amplification of the stress field induced by the stress gradients which are kindled about the treatment spots by the CK distortions. As shown in the Fig. 2.11, the zones surrounding the treatment spots show a

considerable stress increase with respect to the stress induced by the normal intra-ocular pressure of 15-18 mmHg.

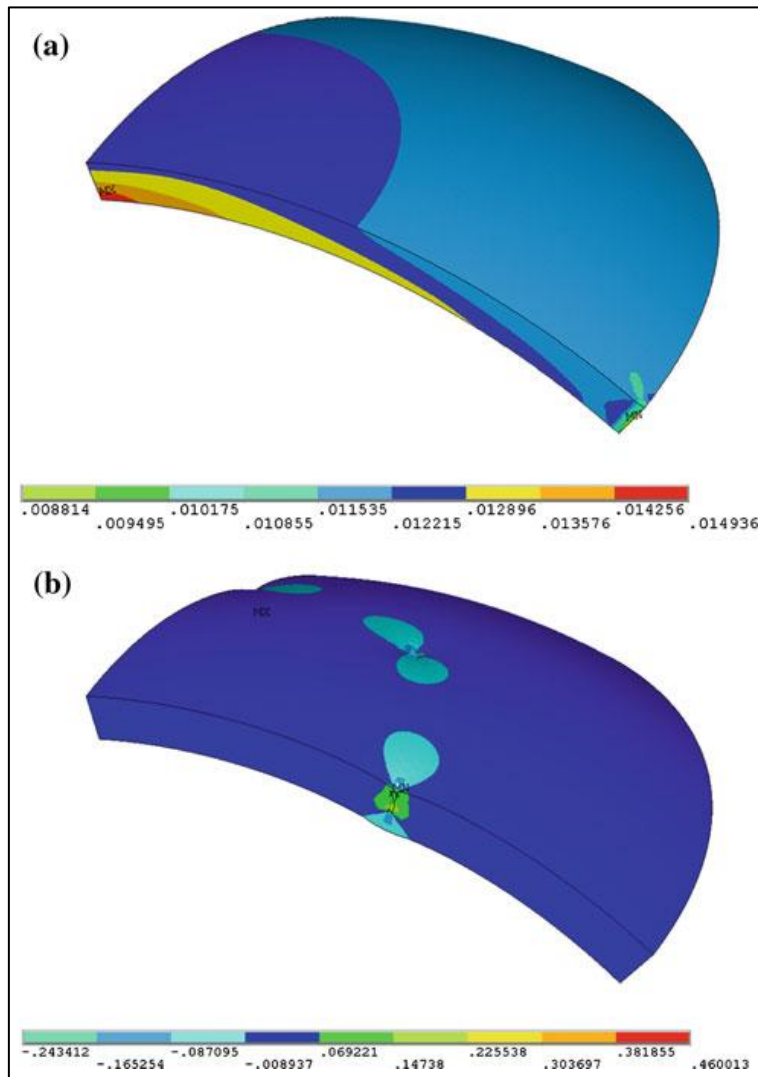


Fig. 2.11

This fact, that is a stress intensification which on average is more than twelvefold than the normal one, suggests that the wound-healing is very likely to play the major role in the commonly observed decrease of the initial degree of the refractive correction, on account of the replacement of myofibroblasts by normal keratocytes that do not have the capacity to resist tension (Esquenazi et al. 2006). It is worth noticing that the present study seems to be the first to provide a quantification of this stress amplification phenomenon on the basis of a straightforward and reliable modelling.

In fact, the accuracy of the FE analyses carried out is confirmed by comparison with experimental readings. Actually, as discussed by Mc Donald (2005): "[...] in the Slit-Lamp photograph of cornea, at 1 hour after CK treatment, are visible as small surface of leukomas, with the lines of tension or striae connecting the treatment of spot. These lines of tension are responsible for the tightening of the peripheral cornea and the subsequent steepening of the central cornea". Fig. 2.12 shows how the adopted FE model successfully captures the cinching effect among the intervention spots. Additionally, a comparison between the FE radial displacements, which depict the steepening of the central part of the cornea, and an orbscan postoperative topography of a CK-treated eye, confirms an accurate modelling of the phenomenon (Fig. 2.13).

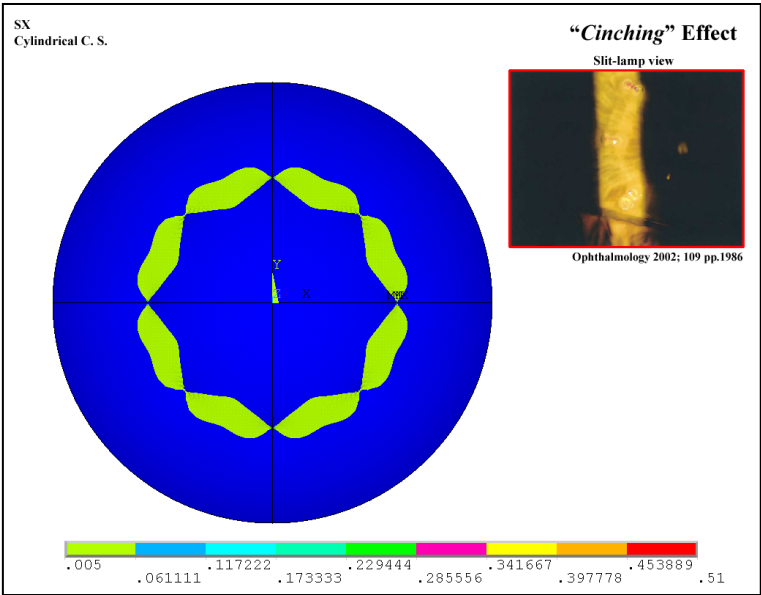


Fig. 2.12

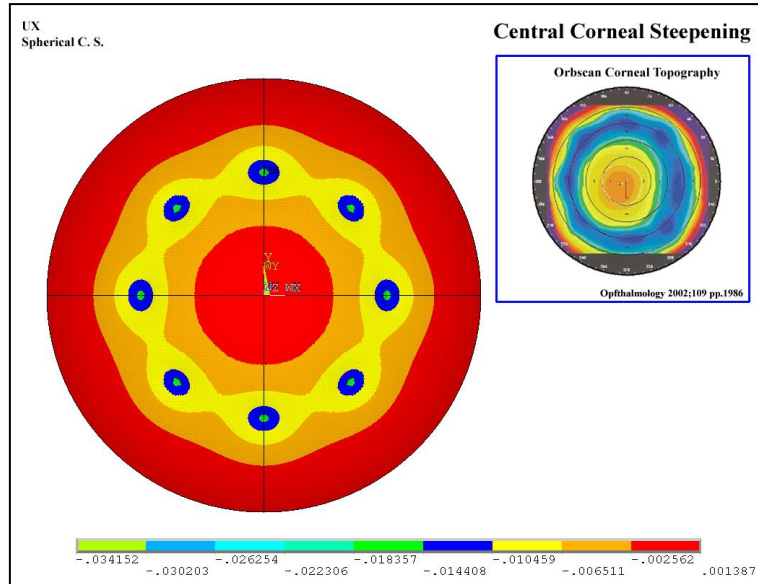


Fig. 2.13

The sharp increase in both the value of the stress field and of the gradient is evident in Fig. 2.14, where a comparison of von Mises stress field and gradient between physiological status (IOP) and post-CK intervention at the intervention annulus is shown.

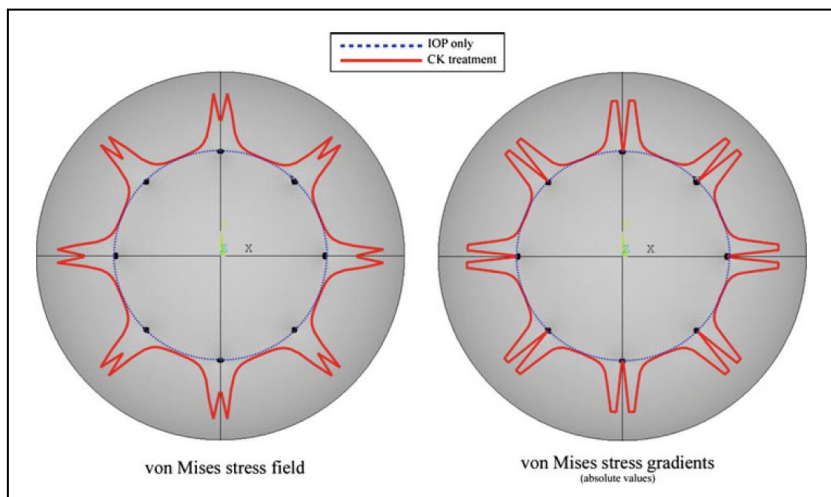


Fig. 2.14

Finally, Fig. 2.15 shows the results from the FE modelling of three different treatments, according to the nomogram of Fig. 2.4: an eight spots, a sixteen spots and a twenty-four spots intervention. In all these simulation the modelling of the lesion was kept the same. The amount of obtained correction is depicted in Fig. 2.16 and it is

evident that the results from the FE analyses are within the range of the clinical readings by McDonald et al. (2002).

Interestingly, the intensity of the stress field surrounding the lesions results of the same order of magnitude in all three cases, thus suggesting that on the whole from a mechanical standpoint the wound-healing and the associated decrease of the initial degree of the refractive correction is liable to be a local phenomenon. In other words, the fact that the observed decrease in correction is proportional to the initial degree of hyperopia seems to depend on the wound-healing at a large number of spots and not on a noticeably different value of the stress field.

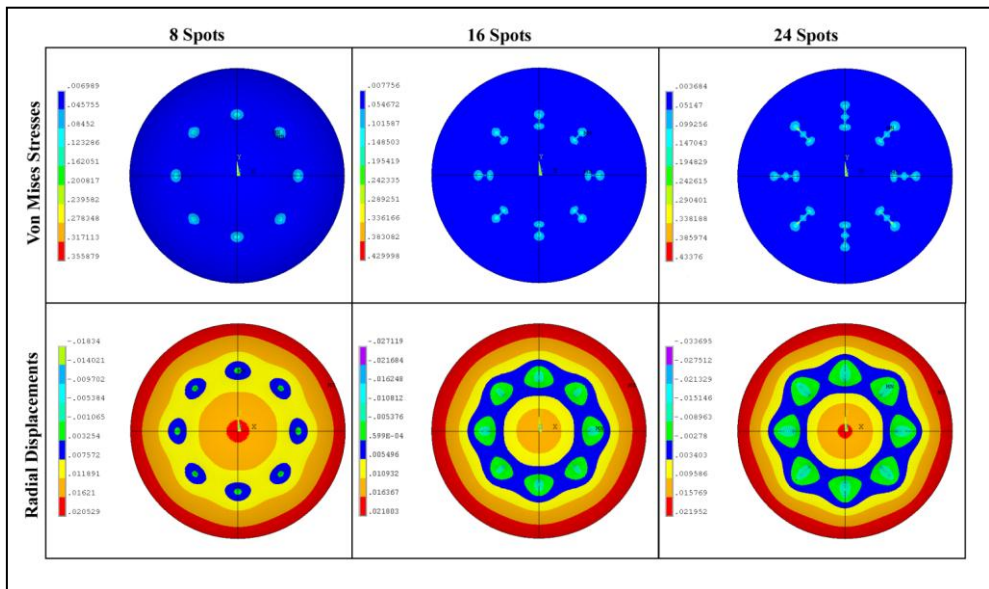


Fig. 2.15

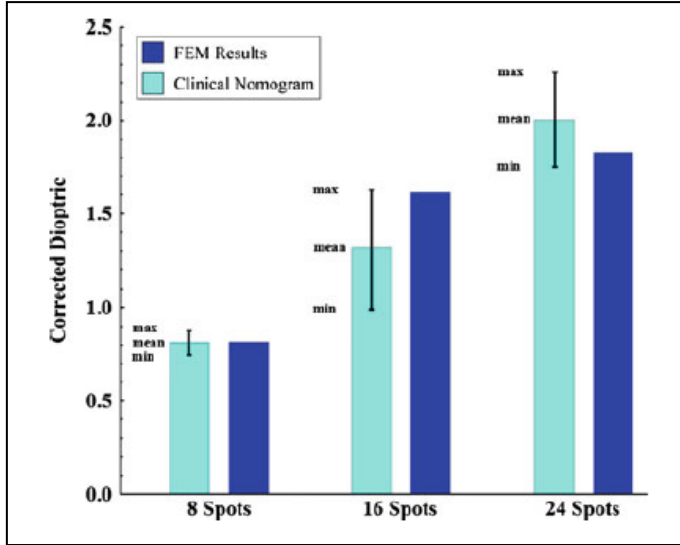


Fig. 2.16

The influence of micro-structural anisotropy

Notwithstanding the fact that anisotropy plays an important role in the characterisation of the corneal tissue, in order to show its scarce relevance with respect to the performed investigation, a comparison between the results of some analyses on a FE anisotropic model of cornea and the previous based on a FE isotropic model is shown. In particular, the way in which the anisotropic behavior of corneal tissue affects the FE analysis of an eight-spots CK intervention has been analysed.

As mentioned before, the corneal mechanical behaviour is to a certain extent affected by the organization of collagen fibrils into the corneal stroma.

With the aim of evaluating the sensibility to the corneal anisotropy of the adopted FE model, CK analyses have been conducted accounting for the trasverse-orthotropic mechanical characteristics used in previous works by Gefen A. et al. (2009). Considering the elastic moduli in a spherical coordinate system, constant values $E_{rr} = 4.5$ MPa and $E_{\varphi\varphi} = 2$ MPa have been assigned in the radial and meridian directions, respectively, while the longitudinal elastic moduli has been set as $E_{\theta\theta} = 2$ MPa at the center of the cornea with a gradual increase toward the periphery, until a value of 7 MPa in correspondence of the limbo-sclera junction. The values assigned to E_{rr} , $E_{\theta\theta}$, $E_{\varphi\varphi}$ are listed in Table 2. The shear modulus is set as $G_{ij} = 0.2$ MPa (Gefen A. et al. 2009).

Mechanical Properties of corneal tissue				
Material zones	Distance from the apex (mm)	$E_{\varphi\varphi}$ [MPa]	$E_{\theta\theta}$ [MPa]	E_{rr} [MPa]
1	0 - 3	2	2	4,5
2	3 - 4	2	3,5	4,5
3	4 - 5	2	5	4,5
4	5 - 6	2	7	4,5

*The orthotropic material properties refer to Gefen A. et al (2009)

Table 2 Material properties at different corneal zones (Gefen et al. 2009)

Fig. 2.17 shows the distribution of the elastic moduli in the FE model.

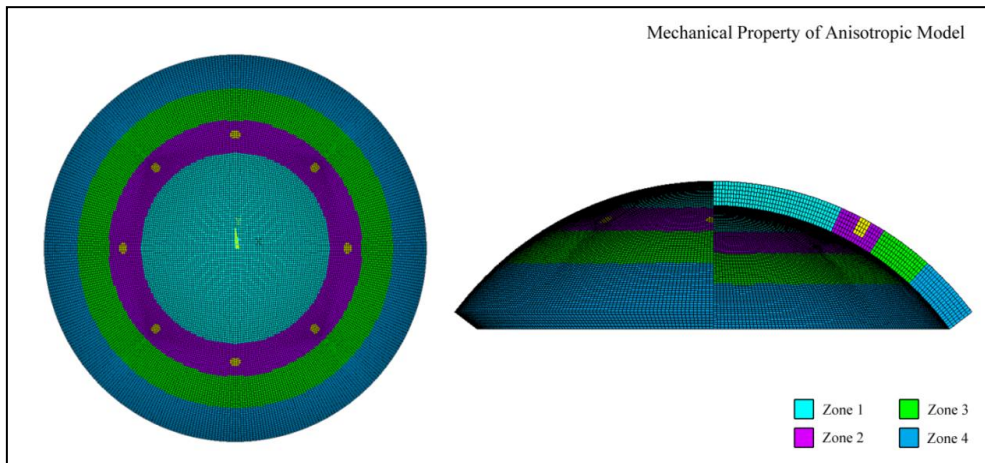


Fig. 2.17 Allocation of zones characterised by different mechanical properties

Following the same procedure of the isotropic case, the modification in the refractive power due to CK has been calculated in the elastic range. The comparison between the results from isotropic and orthotropic cases is reported in Table 3. R^{pre} and R^{post} are the mean radii pre and post CK simulation treatment respectively, whereas D^{pre} and D^{post} are the equivalent dioptric powers. δD is the corrected refractive power

8 Spots Treatment					
	R^{pre}	R^{post}	D^{pre}	D^{post}	δD
Isotropic	7,52129	7,40107	50,1243	50,9385	0,8142
Orthotropic	7,3731	7,256	51,1318	51,9570	0,8251

Table 3 Results from FE 8-spots treatment: *isotropic* versus *anisotropic* modelling

The percent error in the dioptric correction, ε_D results

$$\varepsilon_D = \frac{|\Delta D^{Iso} - \Delta D^{Ani}|}{\Delta D^{Iso}} = 1,3\% \quad (2.14)$$

where ΔD^{Iso} and ΔD^{Ani} are the corrected dioptric powers, as shown in Table 3.

Figures 2.18 and 2.19 show the radial displacement maps from the isotropic and anisotropic *8-spots* models, and the equivalent stress intensity in the tissue around the CK intervention spots, respectively.

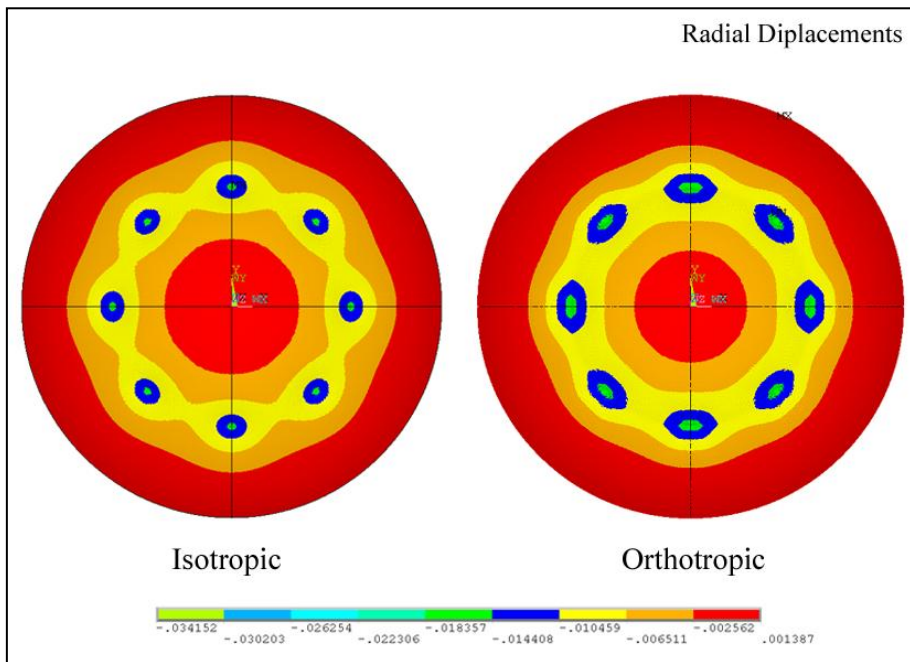


Fig. 2.18 Radial displacements [mm] of the corneal surface from FE: isotropic versus anisotropic modelling

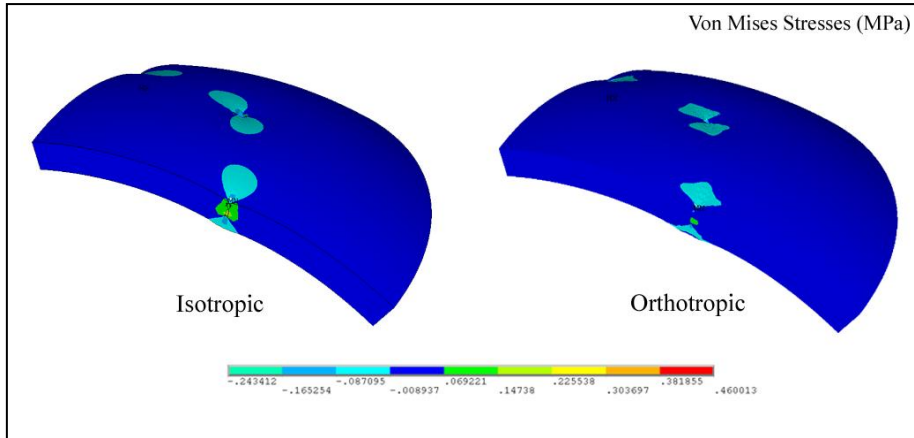


Fig. 2.19 von Mises equivalent stress fields [MPa] from FE: isotropic versus anisotropic modelling

The similarity in the observed behavior is such to suggest that the anisotropic behavior does not affect significantly the response to the CK and the viscoelastic analyses can be meaningfully conducted under the assumption of isotropy.

Multiphysic characterization of Human Cornea

State of art on the thermo-mechanical characterization of corneal tissue

As mentioned above, from the FEM simulation of CK procedure on the human corneal tissue, it has been shown that the viscoelastic properties of the cornea do not contribute to decrease the correction at all and affect the results in the first ten days after surgery to a degree of less than 5%. Several studies presented in the literature highlighted how the soft biological tissues, under no-physiological heating, could be damaged.

To comprise this issue in our model, a coupled thermo-mechanical analysis has been developed.

The mechanical properties of collagenous tissue and its constituent materials are important to take into account at the same time the morphology, the mechanical and thermal behavior. In this respect many efforts have been spent to understand both mechanical and thermal properties, and their rules on the thermal treatment of collagenous tissues.

Moreover the temperature influence on different properties of corneal tissue (thermal damage, hydration and tensile state levels) have been investigated. *Berjano et al.* (2005) assume that the temperature reached in the cornea during CK could overheat the tissue and could cause corneal necrosis leading to regression of the refractive effect achieved by the procedure. By means of FE simulation they studied the electro-thermal behavior of the cornea, highlighting that the maximum temperature exceeds

100° C (temperature of carbonization and perforation injuries), opposite to what *McDonald et al.* (2002) claim during CK treatment, that is the tissue resistance to electrical current flow generates a localized heat smaller than denaturation temperature value. Previously by similar approach *Berjano et al.* (2002) have investigated the influence of several physical parameters on the temperature distribution in the corneal tissue, comparing the dimension/size of CK intervention spot lesion with in-vitro experimental results on rabbit eye.

In this sense the simulation of CK thermal effect on corneal tissue, as shrinking of collagenous structures, the temperature distribution or relative damaging, requires detailed features on previous models. As a matter of fact, the effects of the overheat on biological tissue cannot be easily summarized because the shrinking of structures, the thermal damaging and the phase change appear too. As well established by the scientific community, the high temperatures in biological tissues are closely related with tissue damages and then with their mechanical properties (*Aksan and McGrath*, 2003).

Many efforts have been made to understand the above mentioned characteristics: for instance, water vaporization, changes in the electrical and thermal conductivities of corneal tissue have been taken into account by *Jo and Aksan*, (2010). In their FE model, starting from temperature distribution during CK treatment, they evaluated the accumulation of thermal damage in corneal tissue surrounding the probe inserted into the corneal stroma, to define the success or the failure of the CK therapy. Fluid-dynamical approaches are used to investigate how the presence of heat laminar flow, in the anterior chamber of eye, affect the temperature distribution in the corneal tissue, introducing the anisotropic corneal thermal conductivity (*Karampatzakis and Samaras*, 2010).

Since numerous therapies exploit the heat-induced denaturation of collagen structures to modify the mechanical behavior of tissues, many authors are working to describe the thermo-mechanical behavior of soft tissues. *Stylianopoulos et al.* (2008), introducing in their analytical model both thermal and mechanical variables, have developed a methodology for studying the subtle kinematics of thermal denaturation of collagen tissue and to predict the thermo-mechanical response of homogeneous collagenous tissue. *Baek S. et al* (2005) report the results for biaxial stress relaxation of collagenous tissue, highlighting changes in the viscoelastic behavior due to heating. Many others studied the relations between the thermal damage accumulation and mechanical response of collagenous tissue (*Aksan A ang McGrath JJ*, 2003, *Aksan A et al.*, 2005), but there are not specific FE modeling to describe the thermo-mechanical behavior of these tissues.

As mentioned above, in living tissues, this material time-depending response can interfere with biological time-depending remodelling, growth and morphogenesis processes, thus modifying the tissue structure and its mechanical features over time (Cowin and Doty 2007). The actual overlapping of material and biological responses depends on the ratio between the characteristic times by which the two phenomena evolve, namely stress relaxation and tissue micro-structure changes. Furthermore the temperature has a dramatic influence on rates of viscoelastic response of soft tissues too.

The human body regulates its temperature within a narrow range about 37°C, for above and below this body temperature cells and proteins tend to lose their structure and hence function. For this reason, there has tended to be little motivation over the years to study thermomechanics of soft tissues. Most of innovative medical applications have been motivated by two simple observation: supra-physiologic temperatures can kill cells (e.g. malignant cells) and they denature proteins (e.g. collagen, which shrinks when heated). The effects of heating collagen structures are dependent on the temperature at which they are heated. In fact moderate heating can resulting in a local unfolding within the protein that is reversed upon the restoration of normal temperatures, whereas severe heating results in a time-dependent irreversible and rapid transformation of the native triple-helix structure, into a more random (coiled) structure (Cowin and Doty 2007).

It has been shown that with exposure to thermal loading, the biomechanical characteristics of collagenous tissue are time-temperature and load dependent (Wall MS et al., 1999). Several works studied heat-induced shrinking both treated and normal corneal tissue whereas others investigated the influence of thermal history on the non-linear constitutive responses (Spoerl E et al 2004, Beak S et al. 2005). The viscoelastic behavior of collagenous tissues is independent of the temperature history around physiological temperature, but supra-physiological temperature triggers changes to quasi strain-rate independent behavior. (Brinkmann R et al. 2000; Beak S et al. 2005). As a consequence, from the thermo-mechanical point of view, a preliminary evaluation is needed for assessing the possibility of separating thermal with mechanical effects. With this aim in the next chapter is described a FE thermo-mechanical approach to characterize the response of corneal tissue during the Conductive Keratoplastic surgery.

FE Conductive Keratoplastic simulation: thermo-mechanical approach.

Starting by the corneal model utilized in the previous analyses and described in the previous paragraphs, in the following a simple FE coupled thermo-mechanical

procedure is described. The key idea is to simulate both the thermal effects during the surgical procedure, developing a transient heating and cooling phases, due to the radiofrequency current flows *McDonald et al.* (2002), and also a thermal damage accumulation function which will influence the mechanical behavior of corneal structures in post-operative evolution. The hypothesis of our model is to consider an elastic constitutive behavior of soft tissue as function of thermal damage, and a linear viscoelastic properties not affected by the heating history in the post-operative period. In the following, starting from treatment on the thermal denaturation of collagenous tissues, a FE approach to simulate both the thermal damage accumulation and its effects on the mechanical properties and mechanical response of the corneal structure are described.

Thermal denaturation of collagenous tissue.

Collagen is the major component of collagenous tissue, which it provides the principal structural and mechanical support in the tissue. Under a thermal load, with the increase of temperature, the heat-labile intra-molecular cross-links in collagen are gradually broken, and the collagen undergoes a transition from a highly organized crystalline structure to a random, gel-like state. This process is known as ‘thermal denaturation’, which appears accordingly as thermal shrinkage. With the thermal denaturation of collagen, there are not only structural changes, but also changes in collagen hydration which may involve release of water initially and, absorption of water later. Not surprisingly, thermal denaturation of a collagenous tissue can lead to remarkable changes in the mechanical, thermal, electrical, and optical properties. More studies have been published to describe the temperature dependent tissue denaturation, for example, cartilage and bone. The shrinkage of collagen due to macro scale thermal denaturation can be used as a convenient continuum metric of thermal damage. *Diller & Pearce* (1999) pointed out that the dimensionless indicator of damage Ω is the logarithm of the relative concentration of “reactants” (un-denatured collagen) in the collagen denaturation process:

$$\Omega(t) = \ln\left(\frac{C(0)}{C(t)}\right) \tag{2.15}$$

where $C(0)$ is the initial concentration and $C(t)$ is the concentration of un-denatured collagen remaining at time t .

Then, the degree of thermal denaturation $Deg(t)$, defined as the fraction of denatured collagen, can be calculated as:

$$Deg(t) = \frac{C(0) - C(t)}{C(0)} = 1 - \exp(-\Omega(t)) \quad (2.16)$$

As for the calculation of thermal damage, the Arrhenius burn integration proposed by *Henriques & Moritz* (1947) is widely used. They proposed that skin damage could be represented as a chemical rate process, which could be calculated by using a first order Arrhenius rate equation, whereby damage is related to the rate of protein denaturation (k) and exposure time (t) at a given absolute temperature (T). The measure of thermal injury was introduced and its rate k was postulated to satisfy:

$$k(T) = \frac{d\Omega}{dt} = A \exp\left(-\frac{E_a}{RT}\right) \quad (2.17)$$

Or, equivalently

$$\Omega = \int_0^t A \exp\left(-\frac{E_a}{RT}\right) dt \quad (2.18)$$

where t is the time after the starting of heating, A is a material parameter (*frequency factor*), E_a is the *activation energy*, and $R=8.314$ J/mol K is the universal gas constant. These parameters can be derived experimentally from DSC tests (*Xu A et al.*, 2008).

FE modeling of corneal thermal damage accumulation

The aim of this paragraph is to model the effects of heating and relative damaging during the Conductive Keratoplastic surgery. To this aim a coupled thermo-mechanical analysis has been implemented in ANSYS® finite element code.

In this case, the sole cornea model used in the previous analysis, was meshed by means of 3D Thermal solid elements *SOLID70* that allow to implement the coupled analysis: in fact the FE model used in thermo-mechanical analyses consists of about 30,000 8-node hexahedral elements and 35,000 nodes (figure 20).

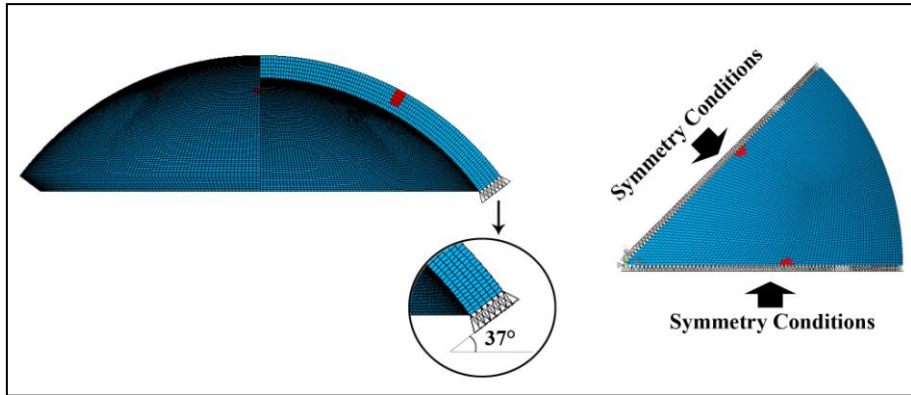


Fig. 2.20 FE model

As mentioned, many efforts have been made to understand both thermal and mechanical properties of collagenous tissue, but few works are concerned the effect of CK heating on the corneal tissue.

For example, *Berjano et al. (2002)* investigated the influences of certain physical parameters (such as the thermal conductivity of the cornea, the curvature of the cornea, and the insertion depth of the electrode into the cornea) on the maximum temperature reached in the tissue during RF heating with a non-penetrating probe. They also compared the size of the predicted thermal lesion in the cornea (assumed to correspond to the 100°C isotherm) to experimental measurements. Later on, their numerical model was used to predict the thermal damage in the cornea due to RF heating using a ring-shaped electrode (*Berjano et al., 2002*). More recently, *Jo and Aksan (2010)* have developing a 3-D FEM model that incorporates the cornea, the aqueous humor, and the RF electrodes to obtain the transient temperature distributions and the resultant thermal damage fields in the cornea during simulated CK procedures. The numerical model incorporated the effects of collagenous tissue denaturation, vaporization of water at 100°C, and the resultant changes in the electrical and thermal conductivities of the cornea tissue. The effects of clinical parameters (RF power setting and pulse duration) on the extent of thermal damage were investigated and the simulation predictions were compared to in vitro experimental results published previously by *Li and Aksan (2010)*.

Karampatzakis A and Samaras T. (2010) have developed a FE model of cornea, where they have considered the influence on the temperature distributions both of the blood perfusion and the metabolic heat generation rate.

In our work we have simplified the model, neglecting some heat generating variables that are not significant during RF heating (*Jo B and Aksan A, 2010*). We have considered the mean body temperature for the corneal tissue (about 37°C) and several

convection parameters are imposed both on the cornea-aqueous humor junction than on the cornea-air interface (Aksan A, 2010). On the lateral surface of model a null thermal flux has considered

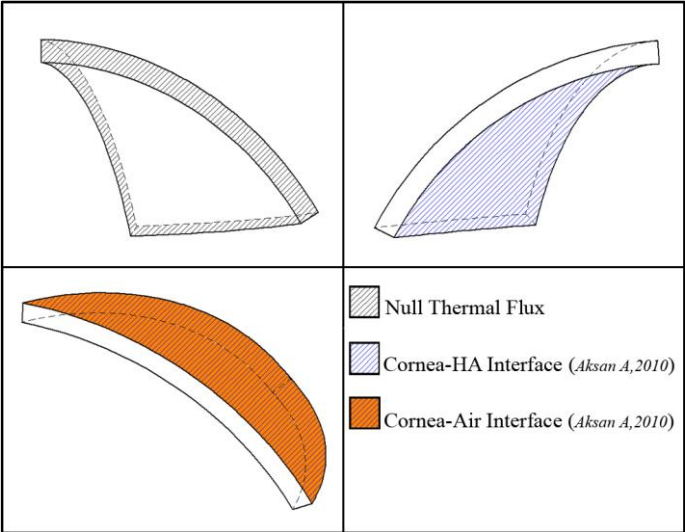


Fig. 2.21 Thermal boundary conditions

The thermal parameters used in FE analysis refer to work of Aksan A. el al (2010) and Kampmeier J. et al. (2000).

As mentioned above, we consider a transient thermal load applied on the CK surgical intervention spots (Fig. 2.5) in according to the curve showed below

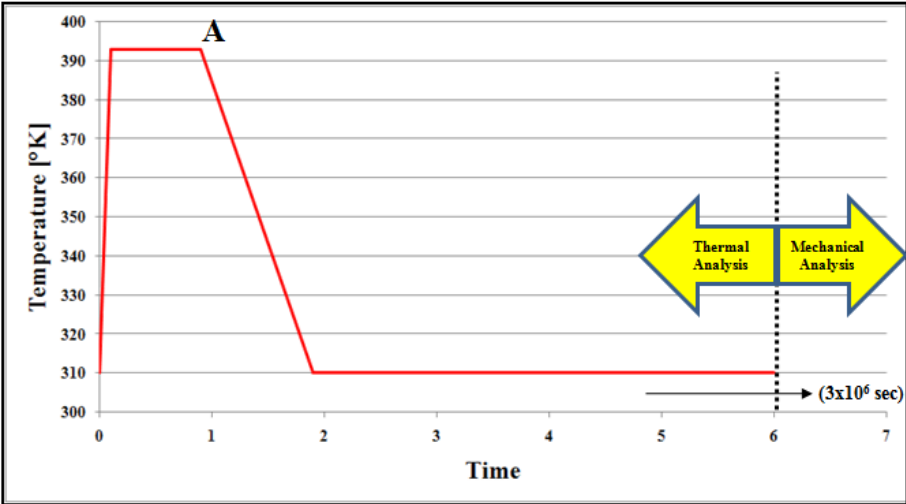


Fig. 2.22 Transient thermal load history

During the analyses, for each time step, the *thermal damage*, function of temperature distribution $T_i(\underline{x})$ and time t , was calculated by the relation below:

$$\Omega_i(\underline{x}) = \int_0^{\Delta t_i} f(T_i(\underline{x}), t) dt = \int_0^{\Delta t_i} A \exp\left(-\frac{E_a}{RT_i}\right) dt \quad (2.19)$$

By setting a stepped thermal load for each time step, the relation above can be rewritten:

$$\Omega_i = A \exp\left(-\frac{E_a}{RT_i}\right) \int_0^{\Delta t_i} dt = A \exp\left(-\frac{E_a}{RT_i}\right) \Delta t_i \quad (2.20)$$

The *thermal damage accumulation* at the end of CK treatment can be obtained by adding each Ω_i through the formula:

$$\Omega = \sum_{i=1}^n \Omega_i = \sum_{i=1}^n \int_{\Delta t_i} f(T_i(\underline{x}), t) dt . \quad (2.21)$$

The pictures below show the temperature distribution at $t = 0.9$ sec (point A in figure 2.22) and the thermal damage accumulation post thermal load history ($t \approx 6$ sec):

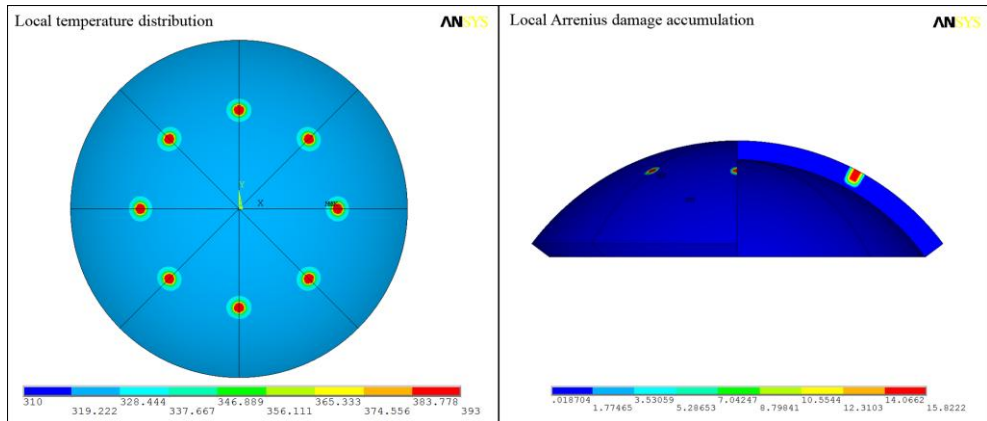


Fig. 2.23

Coupled Mechanical response during CK surgery (Modelling of non linear mechanical response during thermal damaging)

Respect to the mechanical analyses presented in the previous chapters regard the CK surgical intervention, in this paragraph the mechanical behavior of corneal structure coupled with the thermal analyses will be discussed. Starting from the thermal damage accumulation defined above, through an ad hoc ANSYS® procedure, a linear viscoelastic response of structure over the surgical time has been modeled.

To implement the viscoelastic constitutive behavior in the solver it was necessary to set-up on the one hand, the local elastic behavior and on the other hand, the local viscoelastic parameters (see figure 2.3).

For the viscoelastic properties we assume that it isn't temperature dependence, while the elastic response of tissue is strictly dependence on the heating or thermal damage. Accordingly by considering the thermo-mechanical experimental test performed on collagenous tissue by *Aksan and McGrath (2002)* it was possible to relate the Young modulus with the thermal damage accumulation.

From their experimental results it can be established that "with exposure to thermal loading, the collagenous tissue experiences an initial increase of about 20–40% in its tensile modulus (E), followed by an exponential decrease" where "the thermal loading history is represented by an Arrhenius type damage integral" Ω as shown in the picture below:

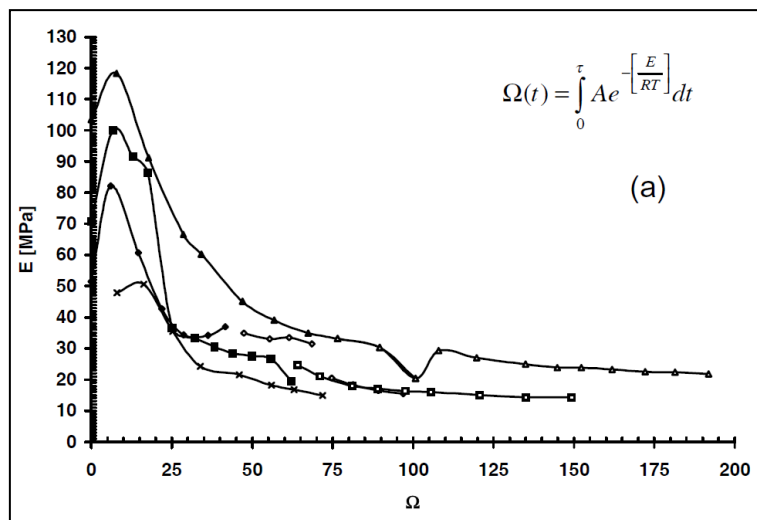


Fig. 2.24 Soft tissue tensile modulus versus damage accumulation

These results allow us to implement the procedures to obtain the Young modulus distribution into the corneal structure $E \Omega_i(x), t$, for each time step i -th.

To perform the viscoelastic non linear analysis, we consider an elastic response dependent on temperature distribution (instantaneous shrinkage achieved via heating), by setting an instantaneous thermal expansion coefficient as *Fraldi et al., (2010)*. In particular the corneal Young modulus distribution refers to maximum heating point, before the cooling phase $t = 0.9\text{sec}$. In the pictures below (figure 2.25) are reported

the Thermo-elastic distortion and the Young modulus distributions at same time step $t = 0.9\text{sec}$.

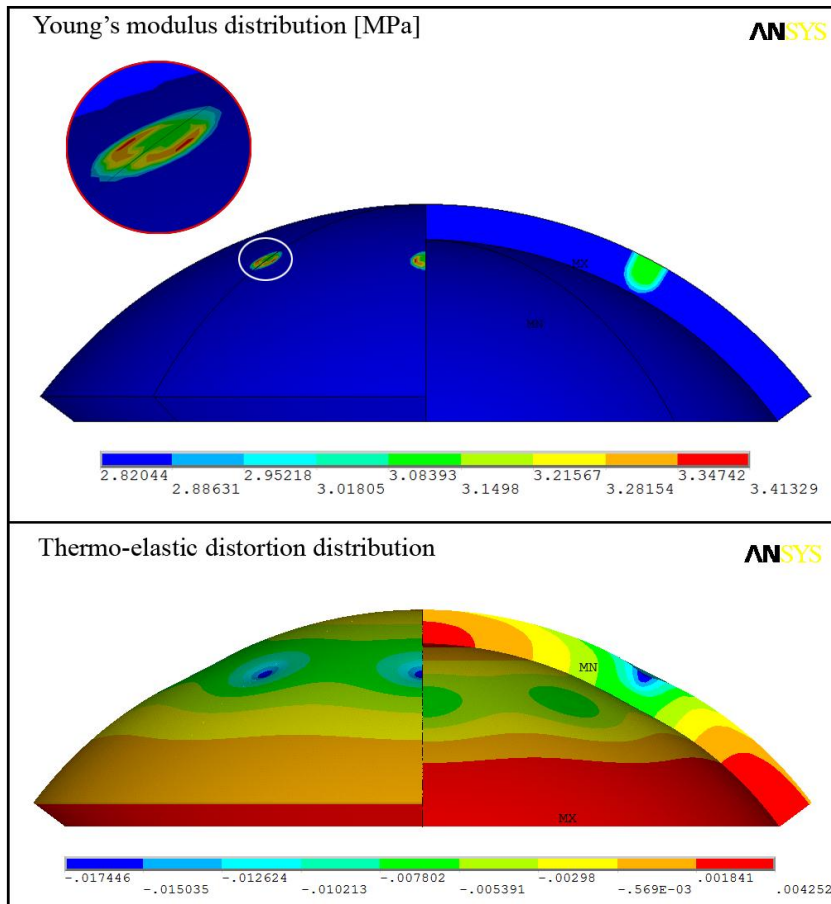


Fig. 2.25

The viscoelastic parameters has been set by the experimental relaxation test of *Zeng et al.*, (2001), see Table1. In order to reduce the computational effort, same boundary conditions, used in previous analyses, have been applied (*Fraldi et al.*, 2010).

The aim of this first coupled analysis, according to the CK nomograms used in surgical techniques, (figure 2.4) is to simulate only the correction defects ranging from 0.75 to 0.875 D applying an annulus with eight intervention spots. The relative dioptric power will be calculated by means of Murrelyn expression (*Murrelyn et al.*, 1988), in the post-operative time ranging from cooled phase to 24 Months' time (*McDonald*, 2005). For each time step i -th, the expression can be written by

$$D(x, t_i) = \frac{n-1}{R(x, t_i)} \quad (2.22)$$

Where n is the corneal refractive index ($n=1.377$) and the changes in the cornea curvature $C^{(i)}(x,t_i)$ and the relative radius $R^{(i)}(x,t_i)$ has been evaluated by means of the equations Eqq. 2.11-2.12.

Thermo-Mechanical Results

As stated before, the objective of this paragraph is to investigate if the thermo-mechanical analysis was capable to reveal particular physical phenomena not highlighted with the previous simple mechanical implementation.

Respect to the previous results, mainly the latter thermo-mechanical results modify the point of view on the rules of viscoelasticity in the post surgical periods, in fact the stress relaxation phenomena not fades in a few day, but it is smeared over the time.

In figure 2.26 a plot of the dioptric power correction () versus time is also shown and, contrarily with the previous statements (see figure 2.10 - *bottom*) , it indicates that it tends to increase in the immediate post-operative period and successively decay over the time.

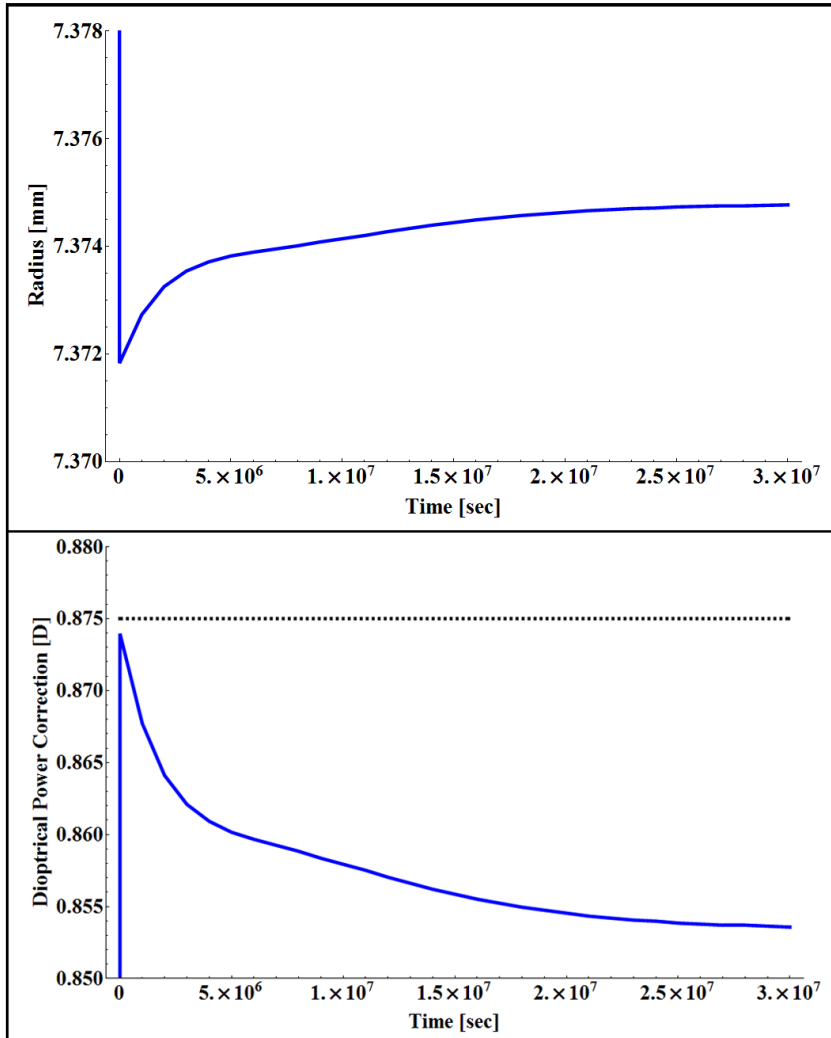


Fig. 2.26:

At the latter is associated an immediate corneal steepening, observed by *Esquinazi et al.* (2006) in the rabbits corneae, which however it changes in this case figure 2.25 (bottom).

The thermal effect due to the CK procedure and relative mechanical response of corneal structure, means that the stresses values into the cornea are on one hand, as previous analysis, greatly respect to the stress induced by the normal intraocular pressure of 15-18 mmHg, and on the other one are not localized in a neighborhood of the spots, but distributed in all corneal structure as shown in the figure 2.27.

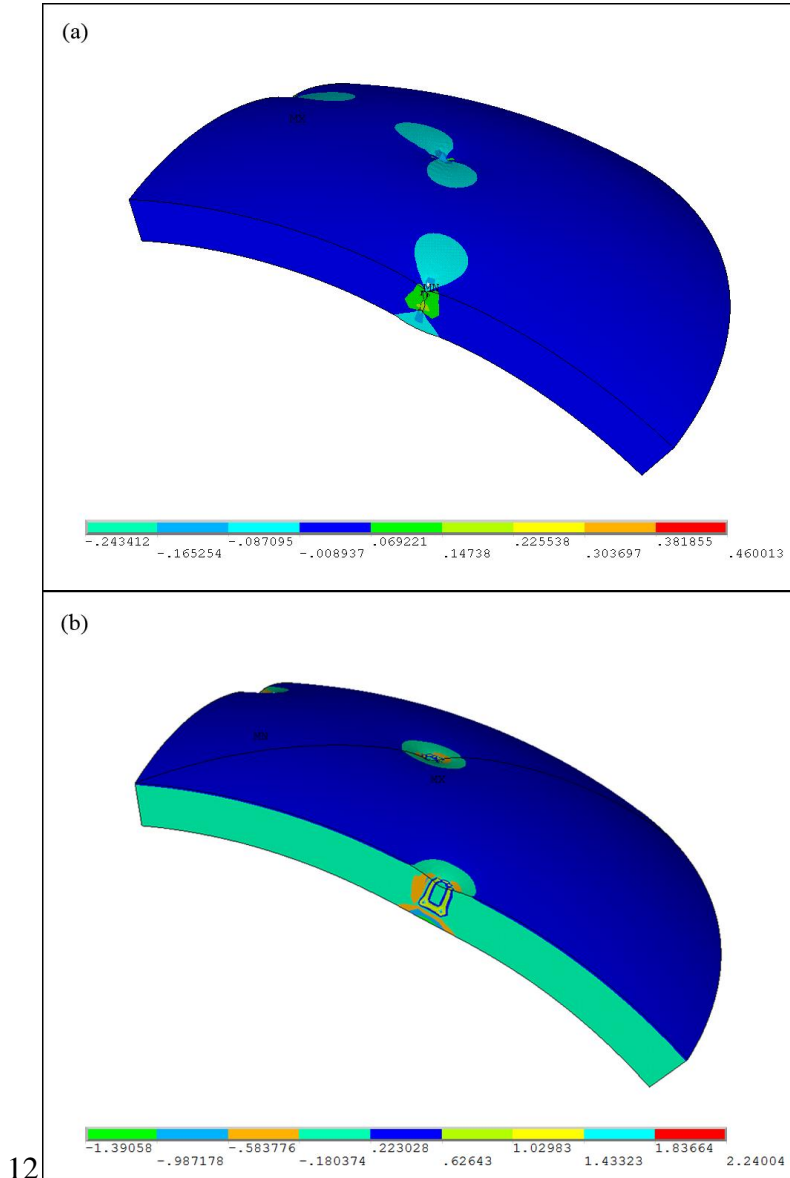


Fig. 2.27

Finally figure 2.28 shows the results from the FE modeling of the amount of achieved correction in the case of eight intervention spots (similarly previous mechanical case Fig. 2.16), and it is evident that it is within the range of the clinical readings by *McDonald et al.* (2002).

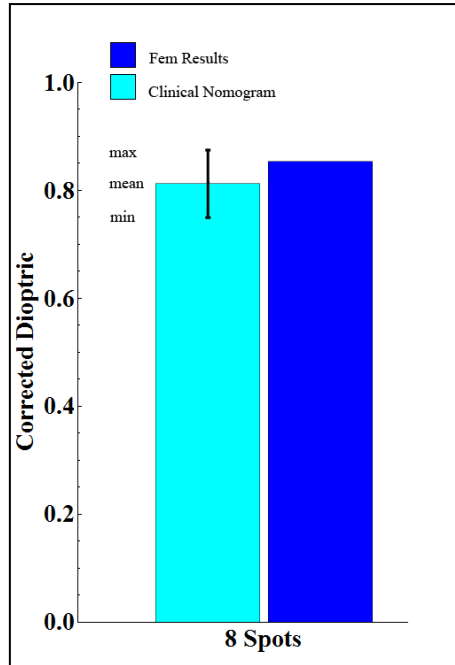


Fig. 2.28:

Conclusion

In this chapter a numerical analyses of the conductive keratoplasty on hyperopic eyes has been carried out, through a simple mechanical and a thermo-mechanical approaches, with the aim of investigating the decrease in the initial degree of refractive correction commonly reported in the post-operative follow-up. First the attention has been focused on exploring a possible influence of the viscoelasticity of the corneal tissue and stress gradients induced by the CK intervention on the stability of the correction, by avoiding unnecessary complications which might obscure the essential behavior of the mode; next the influence of thermal damaging of tissue has been simulated. The simulation has not been aimed to model the complex interactions among all the biological and mechanical factors involved in the phenomenon, but, as most models in physics, has intended to insulate the effect of viscoelastic behavior in both analysis types. Clinical and experimental findings confirm the qualitative behavior of the solution and the results suggest that the viscoelastic properties of the cornea are influenced by the heating tissue, and that it affects the surgical correction in the long term. In both simulations, the stress amplification in the zones surrounding the CK hints that the wound-healing is likely to play an important role in the commonly observed decrease in the initial degree of the refractive correction, too The study aims to contribute to some thermo-mechanical roots for the predictability of the outcome of an increasingly popular technique that, notwithstanding several

advantages with respect to ablative interventions, at present cannot be considered completely predictable and satisfactory.

References

- Aksan A, McGrath J J (2002) Effect of thermal damage on the mechanical properties of collagenous tissue. *Technology and Health Care* 10:292-296
- Aksan A, McGrath J J (2003) Thermo-mechanical Analysis of soft-Tissue Thermotherapy. *J Biomech Eng-T ASME* 123:700-708
- Aksan A, McGrath JJ, Nielubowicz DS (2005) Thermal Damage prediction for collagenous tissues part I: A clinically relevant numerical simulation incorporating heating rate dependent denaturation. *Biomech Eng-T ASME* 127:85-97
- Anderson K., Elsheikh A and Newson T (2004) Application of structural analysis to the mechanical behaviour of the cornea. *J. R. Soc. Interface* 1:3-15
- ANSYS 10.0 User's Manual (2009) ANSYS, Inc. Canonsburg, PA 15317, USA.
- Baek S, Wells PB, Rajagopal KR, Humphrey JD (2005) heat-Induced changes in the finite strain viscoelastic behavior of collagenous tissue. *J Biomech Eng-T ASME* 127:580-586
- Berjano E J, Saiz J and Ferrero J M (2002) Radio-frequency heating of the cornea: theoretical model and in vitro experiments *IEEE Trans. Biomed. Eng.* 49 196–205
- Berjano EJ, Ali JL and Saiz J (2005) Modeling for radio-frequency conductive keratoplasty: implications for the maximum temperature reached in the cornea. *Physiol. Meas.* 26: 157–172
- Boote C, Dennis S, Huang Y, Quantock A J, Meek K M (2005) Lamellar orientation in human cornea in relation to mechanical properties. *J. Struct. Biol.* 149:1-6
- Brinkmann R, Radt B, Flamm C, Kampmeier J, Koop N, Birngruber R (2000) Influence of temperature and time on thermally induced forces in corneal collagen and the effect on laser thermokeratoplasty. *J. Cataract. Refract. Surg.* 26:744–754
- Bryant M, McDonnell P (1996) Constitutive laws for biomechanical modeling of refractive surgery. *J. Biomech. Eng.* 118, 473–481.
- Chen T (2000) Determining a Prony Series for a Viscoelastic Material From Time Varying Strain Data. NASA/TM-2000-210123: ARL-TR-2206

- Cohen RS, Hookey CJ and McCrum NG (1976) Viscoelastic Creep of collagenous tissue. *J Biomech* 9:175-184
- Cowin, S C and Doty, S B (2007) *Tissue Mechanics*. Springer. Berlin.
- Crouch J R, Merriam J C, Crouch E R (2005) Finite Element Model of Cornea Deformation. *MICCAI 2005*, 3750: 591-598
- Diller KR and Pearce JA (1999) Issues in modeling thermal alterations in tissues. *Annals New York Academy of Science*, 888:153-164
- Elsheikh A, Alhasso D, Rama P (2008) Assessment of the epithelium's contribution to corneal biomechanics. *Exp. Eye Res.* 86:445-451
- Elsheikh A, Alhasso D, Rama P (2008) Biomechanical properties of human and porcine corneas. *Exp. Eye Res.* 86:783-790
- Elsheikh A, Brown M, Alhasso D, Rama P, Campanelli M, Garway-Heath D (2008)b Experimental assessment of corneal anisotropy. *J. Refractive Surg.* 24:2
- Elsheikh A, Wang D, Kotecha A, Brown M, And Garway-Heath D (2006) Evaluation of Goldmann Applanation Tonometry Using a Nonlinear Finite Element Ocular Model. *Ann. Biomed. Eng.* 34(10):1628-1640
- Esquenazi S, He J, Kim D B, Bazan N G, Bui V, Bazan E P (2006) Wound-healing response and refractive regression after conductive keratoplasty. *J. Cataract. Refract. Surg.* 32:480–486
- Fernández D C, Niazy A M, Kurtz R M, Djotyan G P And Juhasz T (2006) A finite element model for ultrafast laser–lamellar keratoplasty. *Ann. Biomed. Eng.* 34(1):169-183
- Fung Y C, *Biomechanics: mechanical properties of living tissues*. (1993) Springer-Verlag New York Inc. (2nd Ed)
- Gefen A, Shalom R, Elad d, Mandel Y, (2008) Biomechanical analysis of the keratoconic cornea. *Mech. Behav. Biomed. Mater.* 2:224-236

Grytz R, Meschke G (2009a) A computational remodeling approach to predict the physiological architecture of the collagen fibril network in corneo-scleral shells. *Biomech. Model. Mechanobiol.* DOI 10.1007/s10237-009-0173-2

Grytz R, Meschke G (2009b) Constitutive modeling of crimped collagen fibrils in soft tissues. *J. Mech. Behav. Biomed. Mater.* 2:522-533

Henriques FC and Moritz AR (1947) Studies of thermal injuries, the conduction of heat to and through skin and the temperatures attained therein. A theoretical and an experimental investigation. *A J Pathol*, 23:531-549

Hersh P S (2005) Optics of conductive keratoplasty: implications for presbyopia management. *Trans. Am. Ophthalmol. Soc.* 103:412-456

Hoeltzel D A, Altman P, Buzard K, Choe K (1992) Strip extensometry for comparison of the mechanical response of bovine, rabbit, and human corneas. *J. Biomech. Eng.* 114:202–215.

Jo B, Aksan A (2010) Prediction of the extent of thermal damage in the cornea during conductive keratoplasty. *J Therm Biol* 35: 167-174

Kampmeier J, Radt B, Birngruber R and Brinkmann R (2000) Thermal and Biomechanical Parameters of porcine cornea. *Cornea* 19(3):355-363.

Karampatzakis A, Samaras T (2010) Numerical model of heat transfer in the human eye with consideration of fluid dynamics of the aqueous humor *Phys Med Biol* 55:5653-5665

Lanchares E, Calvo B, Cristóbal J A, Doblare M (2008) Finite element simulation of arcuates for astigmatism correction. *J. Biomech.* 41:797-805

Li L, Tighe B (2006) The anisotropic material constitutive models for the human cornea. *J. Struct. Biol.* 153:223-230

McDonald M B (2005) Conductive keratoplasty: a radiofrequency-based technique for the correction of hyperopia. *Trans. Am. Ophthalmol. Soc.* 103:512-536

McDonald M B, MD, Hersh P S, Manche E E, Maloney R K, Davidorf J, Sabry M (2002) Conductive Keratoplasty for the Correction of Low to Moderate Hyperopia: U.S. Clinical Trial 1-Year Results on 355 Eyes. *Ophthalmology* 109:1978-89

Meek K M, Boote C (2009) The use of X-ray scattering techniques to quantify the orientation and distribution of collagen in the corneal stroma. *Prog. Retin. Eye Res.* 28:369-392

Meek KM, Blamires T, Elliot GF, Gyi TJ, Nave C (1987) The organisation of collagen fibrils in the human corneal stroma: a synchrotron x-ray diffraction study. *Curr. Eye Res.* 6:841-846.

Munnerlyn C, Koons S J , Marshall J, (1988). Photorefractive keratectomy: a technique for laser refractive surgery. *J. Cataract. Refract. Surg.* 14: 46-52.

Naoumidi T L, Pallikaris I G, Naoumidi I And Astyrakakis Ni. (2005) Conductive Keratoplasty: Histological Study of Human Corneas. *Am. J. Ophthalmol.* 140:984–992

Newton R H and Meek K M (1998) Circumcorneal annulus of collagen fibrils in the human limbus. *Invest. Ophthalmol. Vis. Sci.* 39:1125-1134

Nguyen T D, Jones R E, Boyce B L (2008) A Nonlinear Anisotropic Viscoelastic Model for the Tensile Behavior of the Corneal Stroma. *J. Biomech. Eng.* 130(4):041020

Pandolfi A and Holzapfel G A (2008) Three-Dimensional modeling and Computational analysis of the human cornea considering distributed collagen fibril orientation *J. Biomech. Eng.* 130 (6) 061006

Pandolfi A, Fotia G, Manganiello F (2009) Finite element simulations of laser refractive corneal surgery. *Eng. Comput.* 25:15-24

Pandolfi A, Manganiello F (2006) A model for the human cornea: constitutive formulation and numerical analysis. *Biomech. Model. Mechanobiol.* 5: 237-246

Pinsky P M, Van der Heide D, Chernyak D (2005) Computational modeling of mechanical anisotropy in the cornea and sclera. *J. Cataract. Refract. Surg.* 31:136-145

Pinsky P, Datye V (1991) A microstructurally-based finite element model of the incised human cornea. *J. Biomech. Eng.* 10:907–922.

Spoerl E, Wollensak G, Dittert DD Seiler T (2004) Thermomechanical behavior of collagen-cross-linked porcine cornea. *Ophthalmologica* 218:136-140

Stylianopoulos T, Aksan A, Barocasz V H, (2008) A structural, kinetic model of Soft Tissue Thermomechanics. *Biophys J* 94:717-725

Wall M S, Deng X, Torzilli P A, Doty S B, O'Brien S J and Warren R F (1999) Thermal modification of collagen. *J Shoulder Elbow Surg* 8:339-344

Wang X, Zhang J, Liu A, Zeng Y, Yuhua P (2007) Effect of different corneal curvature on corrected power of conductive keratoplasty. *IEEE/ICME*:1164-1167

Wolfram S (2003) *The Mathematica Book*. Wolfram Media. Champaign, USA

Xie J, Wang B, Ju Y and Wu S (2008) Analytic modeling and simulating of the cornea with finite element method. *MIMI 2007*: 304-311

Xu F., Seffen K A and Lu T J, (2008) Temperature-Dependent Mechanical Behaviors of Skin Tissue. *IAENG International Journal of Computer Science*, 35:1

Zeng Y, Yang J, Huang K, Lee Z, Lee X (2001) A comparison of biomechanical properties between human and porcine cornea. *J. Biomech.* 34:53

Equation Chapter (Next) Section 1

CHAPTER III

MODELLING CORD-RUBBER COMPOSITES FOR TIRE APPLICATION

Introduction

Most of modern technologies require materials offering peculiar combinations of several properties that cannot be found in traditional materials – at the same time – such as metals, ceramics and polymers. The idea of coupling different materials obtaining a combination with better properties than each component is very ancient: e.g., mixing straw and mud, our forebears got a very good material for building. In ‘composite materials’, the final combination reaches chemical-physics properties which cannot be found in the separated components; hence their versatility has made their use very frequent in several fields (aerospace, building, ship, automobile, biomedical, etc).

With the expression ‘flexible composites’ we identify composites based upon an elastomeric matrix, whose possible range of deformation is much larger than those of the conventional thermosetting or thermoplastic polymer-based composites. Then, their ability to sustain large deformation, with high load carrying capacity and fatigue strength, make flexible composites very used in pneumatic tire construction. Cord-rubber composites are complex elastomeric composites composed of:

- a. the low modulus rubber matrix, characterized by high extensibility;
- b. a twisted reinforcement (the ‘cord’) with much higher modulus and lower extensibility than the matrix;
- c. an adhesive film (named ‘dip’) which bonds the reinforcement to the matrix.

Such a combination is really effective when the structure needs a high stiffness in reinforcement direction and also flexibility in the plane perpendicular to cords. These properties are requested in tires, that need strength in the cord direction for holding air pressure, but also need to be flexible in order to provide a comfortable ride and cut down on fatigue from bumpy roads.

The performance features of pneumatic tires are mainly controlled by the anisotropic properties of the cord rubber composite: the low-modulus, high-elongation rubber

contains the air and provides abrasion resistance and road grip; the high-modulus, low-elongation cords carry most of the loads applied to the tire in service.

These materials have been studied since '50s: experimental characterization has been widely performed and models (both analytical and finite elements models) have been developed in order to get necessary information about the overall behavior of this material. However, this theoretical investigation has often been performed by using the classical lamination theory, used for orthotropic materials in the hypothesis of linear elastic behavior and for small deformations. This means that important features, such as viscoelasticity and the particular tension-twisting coupling of the cords, are very often neglected.

The aforementioned assumptions represent a limit to the design of tire structures, that requires the acknowledge of the overall behavior of this material. In particular, the main complexity in studying cord-rubber composites is due to non-linearity derived from:

- 1) materials nature (elastomeric matrix and polymeric cords, both showing non-linear viscoelasticity or non-linear elasticity);
- 2) cord geometry (it is not a continuum but a hierarchical structure, whose profile reorganizes in function of applied loads);
- 3) cord rearrangement (orientation) in each kind of tensional state, also in monoaxial tension.

Hence we are proposed to study the non-linear elastic behavior of cord-rubber composites. Phenomenological investigation needs to be supported by theoretical modeling, able to predict the overall behavior of the composite. Such a model, actually, is a powerful tool for the optimization of composite material and of the whole designed structure (in this case, tire and its components). In fact, since this model, we can easily predict composite (and, consequently, tire) response as a function of geometrical parameters (e.g. lamina geometry, cord spacing, cord and matrix content) and cord and matrix features (e.g. cord construction), without using time-consuming 'trial-and-error' strategies.

Concerning modeling activities, both analytical and Finite Elements Method (FEM) have been used to predict mechanical behavior of cord-rubber composites. Several approaches have been adopted for modeling the constitutive behavior of matrix and cord. In particular, our attention is focused on two main aspects: hyperelasticity of matrix compound and peculiar tension-twisting coupling of the reinforcement, modeled by using a customized, hybrid analytical-FEM methodology.

An Overview of tire technology and components

Cord-rubber composites represent a typical example of flexible composites, with an elastomeric matrix and a continuous, unidirectional and corded reinforcement. The development of this kind of materials has its own origins in car industry, since they are the main elements of plies, giving tire necessary stiffness for carrying the complex load system.

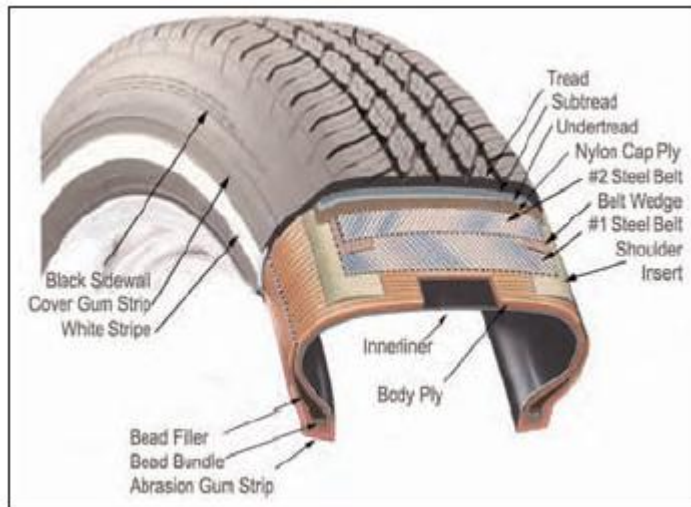


Fig 3.1: Components of a Radial tire

Tire performing features can be modulated by varying the orientation of plies.

Bias-ply tires have body ply cords that are laid at angles substantially less than 90° to the tread centerline, extending from bead to bead.

- ✓ *Advantage:* Simple construction and ease of manufacture;
- ✓ *Disadvantage:* As the tire deflects, shear occurs between body plies which generates heat. Tread motion also results in poor wear characteristics.

Radial tire have body ply cords that are laid radially from bead to bead, nominally at 90° to the centerline of the tread. Two or more belts are laid diagonally in the tread region to add strength and stability. Variations of this tire construction are used in modern passenger vehicle tire (see Figure 3.2).

- ✓ *Advantages:* Radial body cords deflect more easily under load, thus they generate less heat, give lower rolling resistance and better high-speed performance. Increased tread stiffness from the belt significantly improves wear and handling.
- ✓ *Disadvantages:* Complex construction increases material and manufacturing costs.

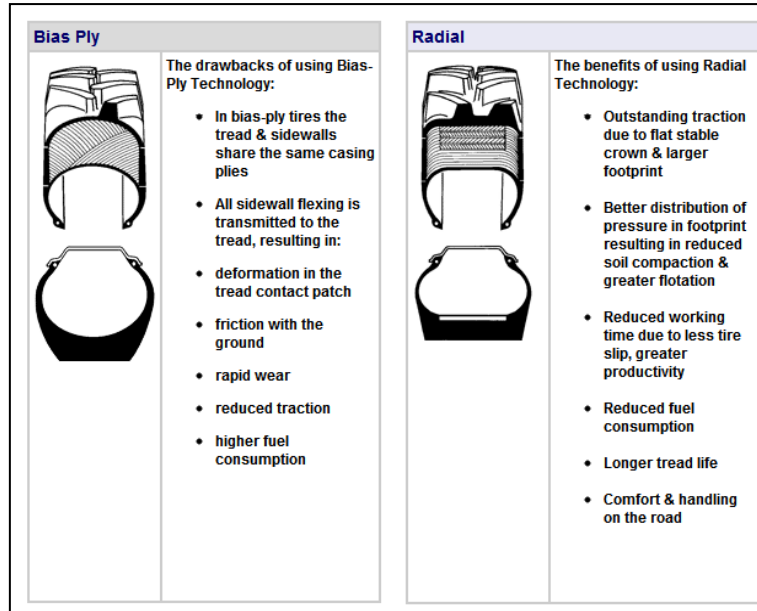


Fig. 3.2: Bias-ply tire vs. radial tire

In addition to these two types exists the *Belted bias tires*, as name implies, are bias tire with belts (also known as breaker plies) added in the tread region. Belts restrict expansion of the body carcass in the circumferential direction, strengthening and stabilizing the tread region.

- ✓ *Advantages:* Improved wear and handling due to added stiffness in the tread area.
- ✓ *Disadvantages:* Body ply shear during deflection generates heat; higher material and manufacturing cost.

Industry standards: size and dimensions

USA tire manufacturers participate voluntarily in an organization known as TRA, The **Tire and Rim Association**. It establishes and promulgates engineering standards for tires, rims, and allied parts (tubes, valves, etc.)

Participation and adherence to these standards assures interchangeability of component parts among different tire manufacturers. “*P-metric*” sizing was introduced as radial tire usage began to expand in North America in the early 1970s. Size nomenclature can be described as follows (see Figure 3.3). For a **P185/60R14** tire, the “P” indicates that it is for a “passenger” car (“T”, temporary; “LT”, light truck). (Note: European tire sizes typically do not utilize the P, T or LT symbols). The “185” is the nominal section width of the inflated, unloaded tire in millimeters. The “60” is the aspect ratio, or “series”. It gives the tire section height as a percentage of the section width. Lower aspect ratio tires, e.g., 45, 50, 55 series tires, are primarily used

Curatives: During vulcanization or curing, the polymer chains become linked, transforming the viscous compounds into strong, elastic materials. Sulfur along with accelerators and activators help achieve the desired properties

Material design property balance. Considering the many polymers, carbon blacks, silicas, oils, waxes and curatives, plus specialty materials such as colorants, adhesion promoters, and hardeners, the variety of compounds available seems endless. A typical car tire uses about 60 raw materials. However, the tire compounder quickly learns that adjusting one of the properties often affects other performance areas. The best tread compound for dry traction and handling might be lacking in wet/snow traction, chip/tear resistance, or fuel economy. Thus, compounds must be “engineered” or “balanced” to meet performance criteria for both the original equipment (OE) vehicle manufacturer and the aftermarket customer. . Adding to the complexity, the chosen compound must be cost-competitive and processable in manufacturing plants.

Reinforcement materials

A tire’s reinforcing materials - tire cord and bead wire - are the predominant load carrying members of the cord-rubber composite. They provide strength and stability to the sidewall and tread as well as contain the air pressure. The type and common usage are:

Nylon type 6 and 6.6 tire cords are synthetic long chain polymers produced by continuous polymerization/spinning or melt spinning. The most common usage in radial passenger tires is as cap, or overlay ply, or belt edge cap strip material, with some limited applications as body plies.

Advantages: Good heat resistance and strength; less sensitive to moisture.

Disadvantages: Heat set occurs during cooling (flatspotting); long term service growth.

Polyester tire cords are also synthetic, long chain polymers produced by continuous polymerization/spinning or melt spinning (*Ashish KS, 2008*). The most common usage is in radial body plies with some limited applications as belt plies.

Advantages: High strength with low shrinkage and low service growth; low heat set; low cost.

Disadvantages: Not as heat resistant as nylon or rayon.

Rayon is a body ply cord or belt reinforcement made from cellulose produced by wet spinning. It is often used in Europe and in some run-flat tires as body ply material.

Advantages: Stable dimensions; heat resistant; good handling characteristics.

Disadvantages: Expensive; more sensitive to moisture; environmental manufacturing issues.

Aramid is a synthetic, high tenacity organic fiber produced by solvent spinning. It is 2 to 3 times stronger than polyester and nylon. It can be used for belt or stabilizer ply material as a light weight alternative to steel cord.

Advantages: Very high strength and stiffness; heat resistant.

Disadvantages: Cost; processing constraints (difficult to cut).

Steel cord is carbon steel wire coated with brass that has been drawn, plated, twisted and wound into multiple-filament bundles. It is the principal belt ply material used in radial passenger tires.

Advantages: High belt strength and belt stiffness improves wear and handling.

Disadvantages: Requires special processing (see figure 1.16); more sensitive to moisture.

Bead wire is carbon steel wire coated with bronze that has been produced by drawing and plating. Filaments are wound into two hoops, one on each side of the tire, in various configurations that serve to anchor the inflated tire to the rim (*Beach D and Schroeder J, 2000*)

Cord-Rubber Composite Modeling

The aim of this paragraph is to examine, through a finite element analysis, the behavior of cord-rubber composite specimen under uniaxial tensile test. For this reason the next paragraphs not include an extensive discussion on the mechanical properties of rubber. In fact only few words will be spent to the implementation of mechanical behavior, of the incompressible and isotropic rubber into the simulator. Whereas attempts have been made to study the behavior of cord rubber composites by finite element methods as a complement to the experimental and analytical methods. In effect the prediction of the micromechanical properties and interface stresses is important for the general understanding of composites and can be very useful in the design and selection of a composite for a particular application. Since the micromechanical properties of these composites depend on the features of the constituent materials, for example, rubber elasticity and the twisted nature of the reinforcement, it is essential to include their behavior in the analysis models. The effects of orthotropic behavior of cords, cord reorientation, bimodular behavior and the large deformation of the rubber material were considered in the above FEM formulation. The approach we adopted for modeling cord rubber lamina finds a new collocation in the literature survey of analytical and FEM models, thanks to the introduction of a new hybrid analytical-FEM model.

Matrix modeling: Non-linear elasticity

Rubber is a fascinating material, with unique properties that make it an essential component of a pneumatic tire: it is soft, elastic, resistant to cutting and scraping, with a high coefficient of friction and low permeability to gases. We consider here what molecular features give rise to this remarkable combination of properties and how they affect tire performance.

All rubbery materials consist of long chain-like polymer molecules. The original elastomeric material (raw rubber) is basically a highly-viscous liquid but it can show elasticity because the long molecules are held together, at least temporarily, by being intertwined and entangled. The basic reaction in rubber processing is the joining of long molecules together by a few chemical bonds (crosslinks) to form a loose three-dimensional permanent molecular network. The shape becomes fixed and the material is transformed from a high-viscosity liquid into an elastic solid. This joining reaction is often termed “curing”, because the material is no longer a viscous sticky liquid, or “vulcanization” because it is usually carried out with reagents that introduce sulfur crosslinks between the molecules.

Rubber can often be treated as virtually incompressible in bulk because the modulus of bulk compression is quite high, about 2 GPa, comparable to that of liquids such as water, and much higher than the tensile modulus E , typically about 2 to 5 MPa. Consequently, the elastic shear modulus G is approximately equal to $E/3$, and Poisson’s ratio is close to one-half, about 0.499. Because rubber is highly extensible, small-strain elasticity theory using moduli E and G is inadequate to describe the response to large strains. Instead, a useful measure of response is the mechanical energy W stored in unit volume by a deformation.

However, even if the rubber compounds currently used in tires are seriously inelastic and attempting to describe their elastic properties with great precision is probably unwarranted, in our approach an hyperelastic constitutive behavior has been adopted.

Hyperelastic constitutive relations, expressed by definition through strain energy functions, are appropriate to model this incompressible material under quasi-static loading where deformations are not infinitesimal. Rivlin obtained a generic strain-energy-based model for incompressible hyperelasticity, commonly referred to (namely in ANSYS®) as the polynomial model, which takes the following form:

$$W = \sum_{i,j} C_{i,j} (I_1 - 3)^i (I_2 - 3)^j \quad (3.1)$$

The Neo-Hookean model, discussed by Treloar, can in fact be obtained from Rivlin’s general formulation with

$$W = C_{1,0} (I_1 - 3) \quad (3.2)$$

taking $C_{10} = 0.5nKT$, where k is the Boltzmann constant, N is the number of chains of molecules per unit volume and T is the absolute temperature.

Mooney's earlier work can also be expressed in terms of the previous equation, resulting in what is generally accepted today as the Mooney-Rivlin model. Finally, some outstanding contributions should also be mentioned, namely by Ogden, Arruda and Boyce as well as Gent who have each proposed hyperelastic models known by their respective names.

ANSYS[®] provides curve fitting tools to obtain material constants for hyperelastic models from the experimental data. The data can be fed to the FEA (Finite Element Analysis) software in the form of tab delimited stress-strain text files of the manipulated characterization data for uniaxial tension. Comparison between experimental data and a Mooney-Rivlin fitting (9 parameters) is shown in Figure. 3.4.

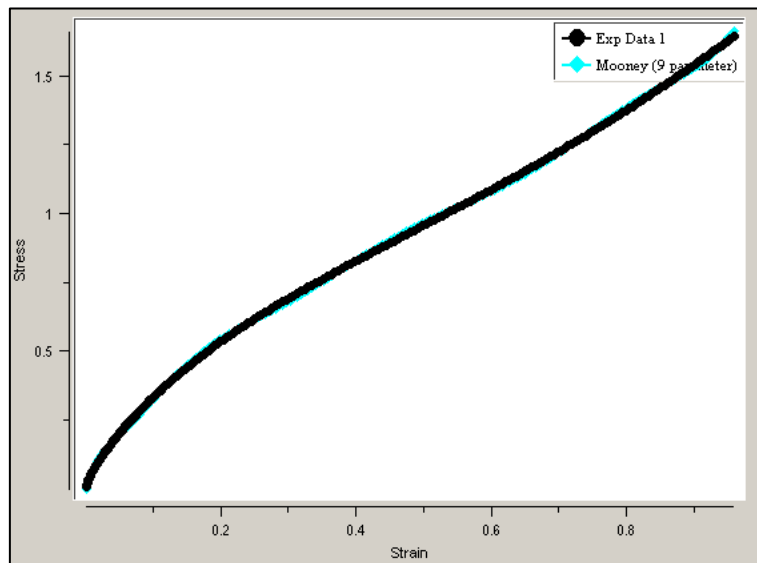


Fig 3.4: Stress-strain curve for rubber: comparison between experimental data (black) and Mooney-Rivlin model (light blue)

Corded reinforcement: textile ‘cord’

The main features of a pneumatic tire, such as the high specific mechanical properties, flexibility, dimensional and shape stabilities, are due to the typical reinforcement used in body plies. In fact, these are generally reinforced with steel or textile (polymeric) cords.

Textile corded reinforcement are complex structures made of hundreds filaments twisted and organized into substructures. Filaments are first twisted together in

bundles (yarn); yarns are then cabled together in helicoidally structures (on several levels) called cords (cfr. Fig.3.5).

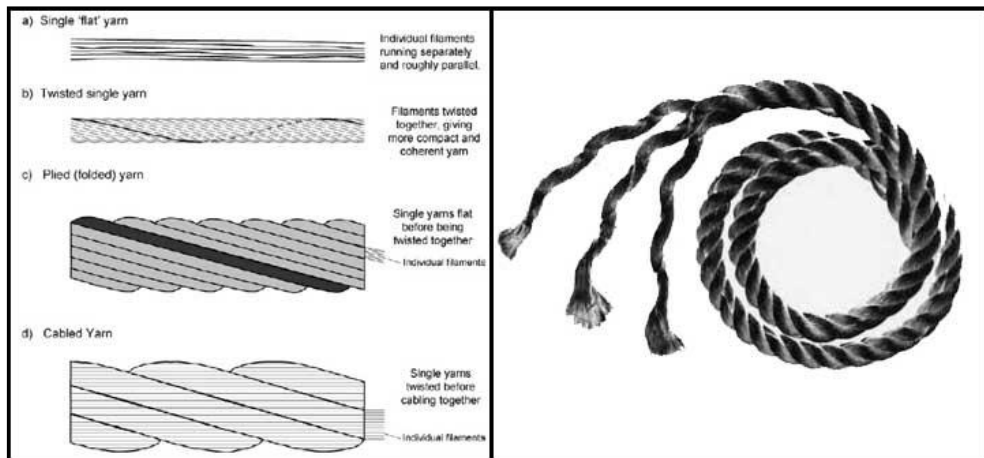


Fig. 3.5 Textile corded structures

The hierarchical twisted, corded structure exhibits high specific properties (e.g. axial stiffness and tensile strength) combined with a low flexural stiffness. This is achieved thanks to the high number of continuous filaments that cooperate in the overall structure. Furthermore, the main mechanical feature is the tension-twisting coupling that means that when such a structure undergoes an axial load, filaments are both stretched and rotated transversally to cord axis. Several pieces of literature (i.e. *Costello*) deal with the mechanical behavior of corded structures, in order to define a constitutive equation providing for this coupling as a function of filament material and structure construction (*twist level, twist angle, cord, yarn and filament radii*).

In the following, the cord modeling based on Costello's theory will be discussed.

Effects of intrinsic trigonality and helicoidal interface in twisted cord-rubber composites: a multi scale homogenization approach

Micro scale level: Costello's model

By the meanings of Costello strand approach, we preliminarily observe, composite at micro scale level to understand filament behaviour within the single yarn. A generic strand wire arrangement is shown in Figure 3.6. A global coordinate system is defined

$\mathbf{e}_1, \mathbf{e}_2, \mathbf{e}_3 \in \mathbf{R}^3$, where \mathbf{e}_3 axis lays on strand axis. Moreover, according to Love (Love, A E.H., 1944), another orthonormal local frame system $\mathbf{x}_1, \mathbf{x}_2, \mathbf{x}_3 \in \mathbf{R}^3$ called *principal torsion-flexure axes* has to be defined for every cross section of the wire.

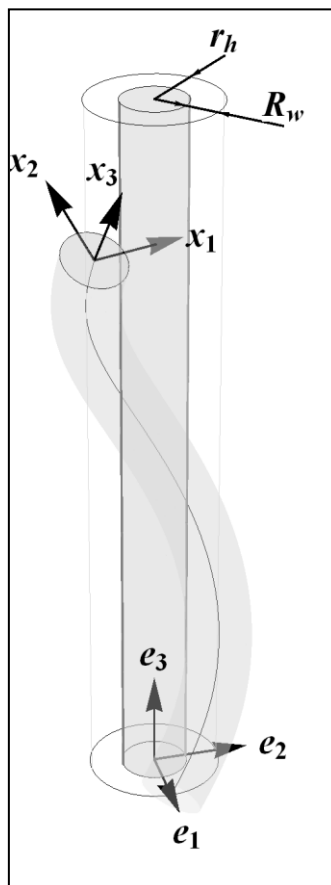


Fig. 3.6: Generic strand wire arrangement, global coordinate system and local frame system are also highlighted

These frames are defined by means of the tangent unit vector of the centreline of the wire \mathbf{x}_3 and by means of two additional unit vectors, \mathbf{x}_1 and \mathbf{x}_2 , that, together, with

the former unit tangent vector, constitute the orthonormal frame of the principal torsion and flexure axes. Specifically unit vector \mathbf{x}_2 is chosen to be normal to the bending plane of the helical wire centerline. In the current chapter a simple straight strand made up of 6+1 wires is adopted to introduce our methods Figure 3.7. The strand consists of six round section wires, radius R_w , wrapped helically around a core, radius R_c . External wires have same geometry and show same helical configuration. The helix angle is α with respect to the strand cross section, and the lay angle is $\beta = \pi/2 - \alpha$ with respect to strand axis, wire centerline helices have radius $r_h = R_c + R_w$. Such configuration represents the simplest wires arrangement in a strand, multiple layers through double or even multiple helix patterns often occur. Strand length is assumed long enough to avoid end sides influence. Radial contact condition is initially considered, it means that layer wires do not touch each other and are in contact only with the core. Friction between wires and core, and eventually between wire and wire, is assumed to be high enough to prevent any relative slip. Interlayer pressure effect and contact deformations are also neglected. According to rod theory, generic load generates in wires traction as well as bending and twisting. Only small deformations are allowed, therefore equilibrium equations are written in the undeformed state. Wire material is isotropic and linearly elastic defined, it is described by Young modulus E and Poisson's ratio ν .

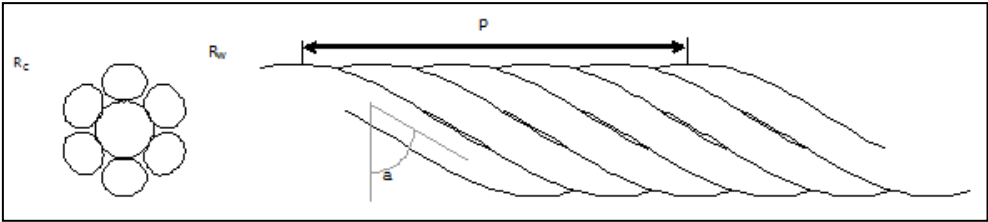


Fig.3.7: Cross section and front of a 6+1 straight strand

Constitutive Assumption

Method introduced by Costello found on helical rod models approach, that ensures a detailed evaluation of strand sensitivity to geometrical and wire material parameters, in terms of linear elastic response; such method is chosen because of low complexity of adopted structure in a way to get a reliable model for strand design. Loads on structure, with regard to tensile load F , torque M_t and bending M_b , are, thus, associated to strand deformations, in terms of elongation ϵ , torsion ϕ and curvature χ . Relation is based on definition of wires helix angle α , their cross sectional

dimension R_w , core dimension R_c and isotropic wire material elastic constants. Survey focuses on elastic strand response, this is the reason for neglecting any non conservative phenomenon, such as friction, wire flattening and plasticity. However, Utting and Jones (*Utting and Jones, 1987*) set specific attention on interwire friction and wire contact deformations in case of small deformation in a strand, they verified low influence of such effects on the global strand behaviour. Moreover, Nawrocki and Labrosse (*Nawrocki and Labrosse, 2000*) performed a research about inter-wire contacts based on finite element model; results demonstrated that rolling and sliding have no influence on overall mechanical response. In addition it is shown that pivoting between external wires and core leads axial strand displacement; moreover comparison with experimental data suggests to consider pivoting as free. Such remarks permit to describe strand kinematics through the degrees of freedom of the core. Is then possible to describe global deformation by three measures: strand axial deformation

$$\varepsilon = \frac{L - L_0}{L_0}, \quad (3.3)$$

strand torsion defined as twist angle per strand unit length,

$$\phi = \frac{\Delta\Theta}{L_0}, \quad (3.4)$$

and strand bending

$$\chi = \frac{1}{\rho}, \quad (3.5)$$

where L_0 and L refer respectively to strand length in initial and stressed configuration, $\Delta\Theta$ is the relative torsion between two strand cross sections at L distance around centreline, and ρ is the centreline curvature.

Costello wire rope's theory (*Costello, G., 1990*) specifically computes Poisson's ratio effect, it leads to draw completely strand geometry deformed configuration. In this frame work, such procedure reveals to be the most reliable to deal with linear steps modelling. In the next section hypothesis of large deformation is introduced, and a non linear numerical procedure able to generate an equivalent homogenized solid cylinder starting from generic straight strand constitutive parameters is proposed.

Single wire kinematics

Axial and torsional load on strand cause deformations in external wires leading from previous to a new helical configuration. By constitutive remarks, is possible to link strand deformations to effective deformations in the wires in terms of curvature, twist increment and strand axis elongation. Let s be the arc length along centreline of a generic external wire, it is considered, in the follow, helix arc length $s = 2k\pi r_h / \cos \alpha$ in the position along the centreline where bending moment on strand is coincident with \mathbf{x}_1 axis of the *principal torsion-flexure* local frame, see Figure 1. Thus, according to the general thin theory of Love (Love, A.E.H., 1944), the kinematics of a rod and, hence for this particular case of a generic wire, are fully defined by four parameters:

$$\varepsilon_w = \varepsilon - \frac{\Delta\alpha}{\tan \alpha} \quad (3.6)$$

that is the wire deformation along its axis;

$$\Delta\kappa_w = \frac{2\sin \alpha}{2 + \nu_w \cos^2 \alpha} \cos\left(\frac{\cos \alpha}{r_h} s\right) \chi \quad (3.7)$$

that is the component of curvature variation in the wire related to \mathbf{x}_1 direction in the local wire coordinate system, where ν_w is Poisson's ratio of the wire, it is set $\kappa_w = 0$ for undeformed configuration;

$$\Delta\kappa_w' = -\frac{2\sin \alpha \cos \alpha}{r_h} \Delta\alpha + \frac{\nu_c R_c \varepsilon + \nu_w R_w \varepsilon_w}{r_h} \frac{\cos^2 \alpha}{r_h} - \frac{2\sin \alpha}{2 + \nu_w \cos^2 \alpha} \sin \alpha \sin\left(\frac{\cos \alpha}{r_h} s\right) \chi \quad (3.8)$$

i.e. the component of curvature variation in the wire related to \mathbf{x}_2 direction in the local wire coordinate system, where ν_c is Poisson's ratio of the core;

$$\Delta\tau_w = \frac{1 - 2\sin^2 \alpha}{r_h} \Delta\alpha + \frac{\nu_c R_c \varepsilon + \nu_w R_w \varepsilon_w}{r_h} \frac{\sin \alpha \cos \alpha}{r_h} + \frac{2\sin \alpha}{2 + \nu_w \cos^2 \alpha} \cos \alpha \sin\left(\frac{\cos \alpha}{r_h} s\right) \chi \quad (3.9)$$

that represents torsional variation in the wire along wire axis. Helix angle increment $\Delta\alpha$ and axis wire elongation ε_w are related to global strand deformation, ε and ϕ , through position:

$$\phi = \frac{\varepsilon_w}{\tan \alpha} - \Delta\alpha + \frac{\nu_c R_c \varepsilon + \nu_w R_w \varepsilon_w}{r_h \tan \alpha} \quad (3.10)$$

which is the relation that accounts coupling effect between torsion and elongation on strand axis, (Costello, G., 1990).

In three of the five equations that describe wire kinematics, (3.7) - (3.9), terms appear that are directly related to strand curvature χ . Such terms are periodic on strand pitch, through arc length measure s . They derive from a treatise on pure bending of a simple straight strand performed by Costello, that is based, again, on rod's mechanics theory. Specifically, deformations on helical wires generated by strand curvature χ , are obtained through a linearization of the equilibrium equations permitted by position $\nu_f = 0$. However such simplification seems to generate results with good approximation for every Poisson's ratio values, Costello (Costello, G., 1990). Small deformations, are imposed, in terms of $|\Delta\alpha| \ll 1$, where α is the helix angle, in radiant. Starting from wire deformations, for both core and external wires, beam theory allows to evaluate wire response.

Constitutive equation

By projecting wires reactions on strand axis, external strand loads can be computed. Hence, globally, for a simple straight strand, loads - axial force F , torque M_t and bending moment M_b - are related to strand deformations - axial strain ε , twist angle per strand unit length ϕ , and curvature χ . It results in axial-twisting coupling and can be represented, in matrix form, through position:

$$\begin{bmatrix} F \\ M_t \\ M_b \end{bmatrix} = \begin{bmatrix} F^\varepsilon & F^\phi & 0 \\ M_t^\varepsilon & M_t^\phi & 0 \\ 0 & 0 & M_b^\chi \end{bmatrix} \begin{bmatrix} \varepsilon \\ \phi \\ \chi \end{bmatrix} \quad (3.11)$$

Is worth to observe that, in such frame theory, symmetry in the axial-twisting coupling matrix is not preserved. By a global point of view axial-twisting coupling is intended as an helical arranged material property, in a way that: considering a tensile load applied on a structure pivoting on its helix axis, it reacts with elongation plus torsion, this is the case, for example, of a weight hanging from a rope, while in case rotation is denied structure is subject to elongation and torque, e.g. lift cables, among others; if an elongation is imposed on pivoting helix axis it reacts through a tensile force and torsion, whereas tensile force and torque are generated if rotation is not allowed, e.g.

platform mooring cables; same relations are involved for boundaries condition involving torque applied or rotation imposed on strand axis.

Sensitivity parameters

Notable aspects of kinematics of the single helical wire are shown in the next by meanings of proposed model. The most decisive geometrical parameter in a simple straight strand design is by far the wire twisting angle α . It defines in which part axis loads have to be split among intrinsic wound wire reactions, in terms of local tensile force, torque and bending moment. Indeed, ratio between core radius and external wire radius also largely influences mechanical behaviour, nevertheless the reason can be yet readdressed to α parameter as helix pitch definition highlights:

$$p = 2\pi R_c + R_w \tan \alpha \quad (3.12)$$

In Figure 3.8, colored curves depict effect of helix angle in a single wire wound counter clockwise around a cylinder, subject to load on its axis. In a generic strand, core participates in system mechanical behaviour. As first analysis, in a way to enhance weight of twisting on wire response, core is modelled as a solid cylinder and its influence is not computed, in this sense the core represents a geometrical constrain. With reference to a generic wire employed in simple straight strand cables, material is supposed isotropic, homogeneous and linearly elastic. Such initial strand configuration, say it B_0 , is supposed stress free. Helical wire kinematics can be completely described in the *principal torsion-flexure* local system, trough axial wire elongation $\Delta\varepsilon_w$, helix curvature variations $\Delta\kappa_w$, $\Delta\kappa'_w$ and wire torsional variation $\Delta\tau_w$. Is worth to note that in case no bending is applied on strand, curvature κ_w in direction of local axis \mathbf{x}_1 remains null in every section.

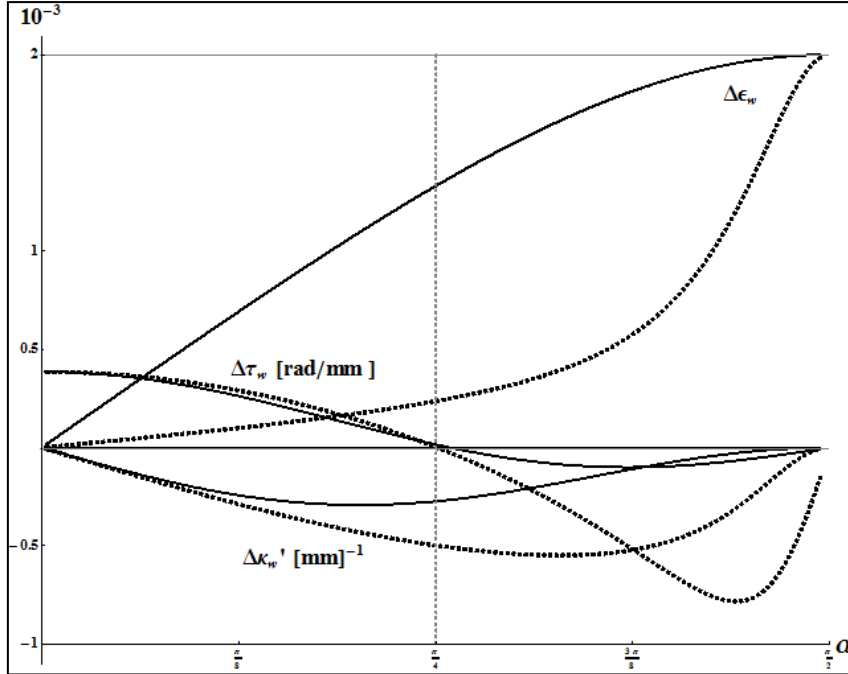


Fig. 3.8:

In many applications strand cables are employed as reinforcing fibres or rope systems, the related model boundary conditions prescribes no rotation on strand axis and torque reaction that acts on every strand cross section; however strand wire kinematics is investigated also in case of free strand rotation, i.e. no torque in every cross section. In 3.8 are highlighted results related to a defined case, specifications are in the caption. A small elongation $\bar{\varepsilon}$ is applied to the strand, continuous lines refer to completely fixed end condition $\varepsilon = \bar{\varepsilon}$, $\phi = 0$, while dashed ones to free rotation condition $\varepsilon = \bar{\varepsilon}$, $M_t = 0$. Curves span in the range of helix angle value $\alpha \in 0, \pi/2$. Although effective low limit is $\alpha = \arctan\left[\frac{R_w}{\pi R_c + \pi R_w}\right] > 0$, it is possible to interpret model response for $\alpha \rightarrow 0$, that means to consider the wire wrapped on a flat circle path. In such condition, axial load on strand works exclusively on wire torsion, such torsion is positive for counter clockwise helix wire deformation. Whereas, on the other range end, $\alpha \rightarrow \pi/2$, wire tends to acts as a straight rod, it means that the imposed load is totally projected on wire axis. For other configurations, helix curvature variation $\Delta\kappa'_f$ is also involved. Load on strand axis can cause positive or negative wire torsion variation. Let helix angle $\alpha_{\Delta\tau=0}$ define strand configuration in which strand axial load is characterized by no torsion on wire axis, its value depends

on relation between Poisson's ratio in the core and wire materials. For this specific single wire analysis it results $\alpha_{\Delta\tau=0} = \pi/2$. Thus, in case of $\alpha < \alpha_{\Delta\tau=0}$, wire helical path shows low pitch-radius ratio, therefore torsion contributes to strand elongation through coils spreading. On the other hand, for stretched wires path, i.e. $\alpha > \alpha_{\Delta\tau=0}$, an opposite torsion in sign, negative in counter clockwise helical wire, works to unwind the helix tending to straight the wire configuration. Strand elongation enhances wire elongation, despite other wire deformations, as much as α value increases. Such effect is higher in axial traction applied test, and enhances for higher R_w/R_c ratio values.

Non-linear Costello's model

Linear relation (3.11) furnishes a useful method to comprehend wire properties in a strand. Indeed following Costello approach, by prescribing small helix angle variation, it is possible to correlate strand deformation and small loads. To predict simple straight strand performances under large loads, a nonlinear quasi-static numerical approach has followed. It develops through linear load steps, each load increment is applied on undeformed configuration since strand geometry is updated before next step will execute. By computing for each linear step the Poisson ratio effect, which is at the base of **Costello's** mechanics of strand, the load effects on strand geometry are considered, even in terms of wire transverse contraction. Equilibrium equations are thus written for the deformed state.

Numerical Procedure

Procedure divides loads in a number of steps small enough to satisfy $|\Delta\alpha| \ll 1$ condition for helix angle variation. Take in account the previously presented strand wire analytical model, let B_0 its starting geometrical initial configuration; when it is subjected to small loads, rod's theory provides to calculate axial wire elongation $\Delta\epsilon_{w0}$, helix curvature variation $\Delta\kappa_{w0}$ and wire torsional variation $\Delta\tau_{w0}$, is thus possible to define a new deformed strand wire geometry B_1 , where helical pitch $p_{w1} = p_{w0} (1 + \Delta\epsilon_{w0})$, curvature variation $\Delta\kappa_{w1} = \kappa_{w0} + \Delta\kappa_{w0}$ and torsion $\Delta\tau_{w1} = \tau_{w0} + \Delta\tau_{w0}$. By following same linear approach, one more admissible load step will produce on geometry B_1 another deformed configuration, say it B_2 , where a further load step is allowed. Strand wire in generic B_i configuration reacts under i^{th} load step, although it is directly related to B_i initial condition it brings the effects of the sum of all previous

steps. Step by step strand traction loads on wire can be computed as sum of related loads in each previous single step, while axial and torsional deformation results in $\varepsilon_i = \sum_{j=1}^i \varepsilon_j \frac{p_j}{p_0}$ and $\phi_i = \sum_{j=1}^i \phi_j \frac{L_j}{L_0}$. Procedure keeps on until prescribed total load is achieved.

Helical wire non-linear behavior

In the follow, numerical process is implemented to draw non linear behaviour of a single wire wrapped around a core under large elongation along the strand axis.

Material and filament arrangement used in pervious analysis, i.e. B_0 initial configuration, are used; the influence of initial helix angle $\alpha_0 \in \left] 0, \frac{\pi}{2} \right[$ is investigated.

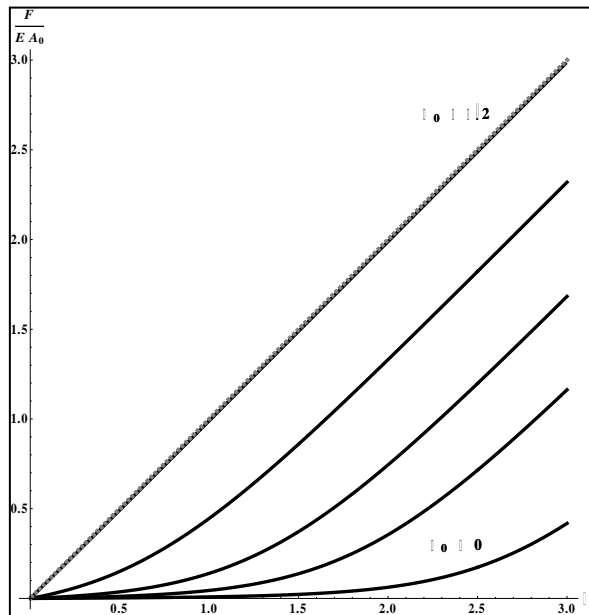


Fig. 3.9a

Figure 3.9a shows, for each i^{th} load step, force F_w on wire in \mathbf{e}_3 strand axis direction, versus strand \mathbf{e}_3 axis strain ε . Values are normalized respect axial stiffness in straight wire configuration, $E \cdot A_0 = E \cdot 2\pi R_w^2$. Investigations are made under axial displacement load, avoiding strand rotation; reacting torsional moment M_t , therefore, occurs, Figure 3.9b.

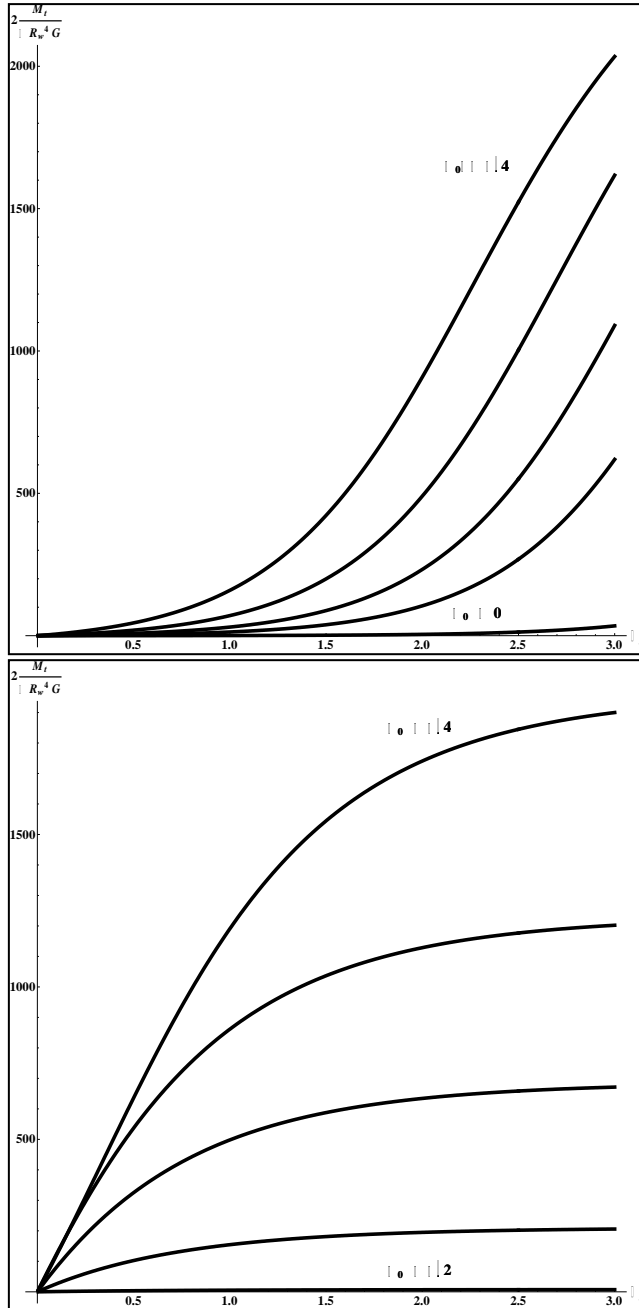


Fig. 3.9b

Helix angle sensitivity highlights a wire behaviour closer and closer to straight wire configuration, as much as $\alpha_0 \rightarrow \pi/2$. While for $\alpha_0 \rightarrow 0$ helical arrangement provides lower \mathbf{e}_3 axis stiffness and a typical toe region appears for low values of the axial deformation ε . In any case, while deformation rises, global axial stiffness increases and tends to the value of the local axial stiffness of the straight wire; moreover curves tends to become parallel, it happens because of large elongations mean higher helix angles, fact that leads to straight wire response.

Meso scale level: Equivalent trigonal cylindrical model

Numerical procedure exposed before, allows to describe the non linear elastic behaviour of each wire in a strand starting both from geometrical strand configuration and isotropic material properties of its components. Substantially is possible to predict overall strand mechanical performance in the whole elastic region, throughout simple measuring of few parameters. For a simple straight strand, which consists of one straight core and a single external layer of surrounding helical wires made of same isotropic material, only five parameters are needed: they are defined by measuring core radius, external wire radius, helix angle or pitch and two isotropic material constants. Thus it is possible to rise to an higher scale level, both form geometric and constitutive point of view. We are able, indeed, to model complex heterogeneous strand arrangement as a solid cylinder, which is equivalent to the strand in terms of overall mechanical response, constitute of homogeneous non linear elastic material.

Trigonal Material Assumption

In a way to count axial-twisting coupling effect, a material model with trigonal symmetry is chosen to define homogenized material. The classification of types of linear material symmetries by the number and orientation of the normals to the planes of material symmetry is fully equivalent to the crystallographic method using group theory. The trigonal crystal system has exactly one plane of reflective symmetry. For an easier treatise we introduce now a cylindrical reference system $\mathbf{r}, \boldsymbol{\theta}, \mathbf{z} \in \mathbf{R}^3$, with \mathbf{z} axis coincident to \mathbf{x}_3 axis in the global coordinate system. Trigonal elastic symmetry retains, in its canonical symmetry system, cross-elastic constants connecting normal stresses (strains) to shear strains (stresses) and vice versa. In the 6 by 6 matrix of elastic coefficients these cross-elastic constants appear in the lower left and upper right 3 by 3 submatrices. A representation for the elastic compliance matrix in the Voigt notation for a material with trigonal symmetry is

$$\begin{matrix}
\varepsilon_{zz} \\
\varepsilon_{\theta\theta} \\
\langle \varepsilon_{rr} \rangle_e \\
\varepsilon_{z\theta} \\
\varepsilon_{zr} \\
\varepsilon_{\theta r}
\end{matrix}
=
\begin{bmatrix}
C_{11} & C_{12} & C_{13} & C_{14} & 0 & 0 \\
C_{12} & C_{22} & C_{23} & C_{24} & 0 & 0 \\
C_{13} & C_{23} & C_{33} & C_{34} & 0 & 0 \\
C_{14} & C_{24} & C_{34} & C_{44} & 0 & 0 \\
0 & 0 & 0 & 0 & C_{55} & C_{56} \\
0 & 0 & 0 & 0 & C_{56} & C_{66}
\end{bmatrix}
\cdot
\begin{matrix}
\sigma_{zz} \\
\sigma_{\theta\theta} \\
\langle \sigma_{rr} \rangle_e \\
\sigma_{z\theta} \\
\sigma_{zr} \\
\sigma_{\theta r}
\end{matrix}
\quad (3.13)$$

An interesting aspect of trigonal symmetry is the symmetry-breaking character of the cross-elastic constant C_{14} . It is directly related to out of diagonal terms in axial-coupling relation introduced before (3.11). They depends on helix wire angle α ; when it tends to $\pi/2$ system shows no coupling and the compliance matrix (3.13) becomes that for hexagonal or transversely isotropic symmetry, i.e. $C_{14} = 0$. Homogenized conservative linear elastic material behaviour prescribes symmetry of compliance matrix. Thus, to use results computed through relation (3.11) equality $F^\varepsilon = M^\phi_t$ need to be satisfied. Numerical model based on Costello theory does not ensure such symmetry, therefore only symmetrical part of axial-twisting matrix coupling is used to perform strand monoclinic homogenization, basing on relation:

$$\begin{bmatrix}
F^\varepsilon & F^\phi & 0 \\
M^\varepsilon_t & M^\phi_t & 0 \\
0 & 0 & M^\chi_b
\end{bmatrix}
=
\begin{bmatrix}
F^\varepsilon & \frac{F^\phi + M^\varepsilon_t}{2} & 0 \\
\frac{F^\phi + M^\varepsilon_t}{2} & M^\phi_t & 0 \\
0 & 0 & M^\chi_b
\end{bmatrix}
+
\begin{bmatrix}
0 & \frac{F^\phi - M^\varepsilon_t}{2} & 0 \\
-\frac{F^\phi - M^\varepsilon_t}{2} & 0 & 0 \\
0 & 0 & 0
\end{bmatrix}
\quad (3.14)$$

Evaluation of neglecting antisymmetric part is computed on helix angle variation trough the evaluation of ratio:

$$\eta_s = \frac{F^\varepsilon - M^\phi_t}{F^\varepsilon + M^\phi_t} \quad (3.15)$$

For generic strand arrangement η_s ratio tends to zero for external wires in the strand that get more and more straight, ratio between core and filament radii does not affect such behaviour, while ratio between core and filament Poisson ratios tends to improve negligibility of antisymmetric part, as much as it assumes lower values. However, in the common technological applications helix angles have values high enough to allow,

with good approximation, to neglect antisymmetric part of the strand constitutive matrix (3.11).

Parametric compliance constants

To completely describe conservative mechanical behaviour of monoclinic homogenized material, it is necessary to evaluate each single constant in the compliance matrix (3.13); numerical model introduced above is able to furnish such kind of information. Parametric expression of each constant is formulated in terms of strand parameters (i.e. $R_c, R_w, \alpha, E, \nu_w, \nu_c$), by stress and strain measures based on following relations:

$$\langle \sigma_{zz} \rangle = \frac{F}{A}, \quad \langle \sigma_{z\theta} \rangle = \frac{2M_t}{\pi R_t^4} r \quad (3.16)$$

$$\langle \varepsilon_{zz} \rangle = \varepsilon, \quad \langle \varepsilon_{\theta\theta} \rangle = \langle \varepsilon_{rr} \rangle = \frac{\varepsilon R_c \nu_c + R_f \nu_f}{R_c + R_f}, \quad \langle \varepsilon_{z\theta} \rangle = \phi \cdot r \quad (3.17)$$

where F and M_t are axial force and torsional moment on strand and ε and ϕ are axial strand deformation and torsional angle on unit length, related through relation (3.11); R_c, ν_c and R_w, ν_w represent filament radius and Poisson ratio in the core and in the external filament respectively, R_t and r are total and generic local strand radius. Is worth to observe that, because of non symmetry of Costello approach, relation $C_{14} \neq C_{41}$ occurs. Such terms are the only elastic constants that depend on radial position in the cross section of the homogenized cylindrical strand, indeed it is possible to write:

$$C_{14} r = \frac{\langle \varepsilon_{z\theta} \rangle}{\langle \sigma_{zz} \rangle} = \frac{A \cdot \phi \cdot r}{F} \quad (3.18)$$

and

$$C_{41} 1/r = \frac{\langle \varepsilon_{zz} \rangle}{\langle \sigma_{z\theta} \rangle} = \frac{\pi R_t^4 \cdot \varepsilon}{2M_t \cdot r} \quad (3.19)$$

The previous consideration of antisymmetric part of axial coupling matrix (3.14) leads to define C_{14} constant in (3.13) as $C_{14}^s = \frac{C_{14} + C_{41}}{2}$, in a way to preserve

conservativeness of homogenized material. In the follow, details of monoclinic compliance constants calculation are presented:

$$\begin{aligned}
C_{11} &= \frac{\langle \varepsilon_{zz} \rangle}{\langle \sigma_{zz} \rangle} = \frac{A \cdot \varepsilon}{F}; C_{12} = C_{21} = \frac{\langle \varepsilon_{\theta\theta} \rangle}{\langle \sigma_{zz} \rangle} = C_{13} = C_{31} = \frac{\langle \varepsilon_{rr} \rangle}{\langle \sigma_{zz} \rangle} = \frac{A \cdot \varepsilon}{F} \cdot \frac{R_{c0} \nu_c + R_{w0} \nu_w}{R_{c0} + R_{w0}}; \\
C_{14} &= \frac{\langle \varepsilon_{z\theta} \rangle}{\langle \sigma_{zz} \rangle} = \frac{A \cdot \phi \cdot r}{F}; C_{41} = \frac{\langle \varepsilon_{zz} \rangle}{\langle \sigma_{z\theta} \rangle} = \frac{\pi R_t^4 \cdot \varepsilon}{2M_t \cdot r}; \\
C_{24} = C_{42} &= \frac{\langle \varepsilon_{\theta\theta} \rangle}{\langle \sigma_{z\theta} \rangle} = C_{34} = C_{43} = \frac{\langle \varepsilon_{rr} \rangle}{\langle \sigma_{z\theta} \rangle} = \frac{\pi R_t^4 \cdot \varepsilon}{2M_t \cdot r} \cdot \frac{R_{c0} \nu_c + R_{f0} \nu_f}{R_{c0} + R_{f0}}; C_{44} = \frac{\langle \varepsilon_{z\theta} \rangle}{\langle \sigma_{z\theta} \rangle} = \frac{\pi R_t^4 \cdot \phi}{2M_t};
\end{aligned} \tag{3.20}$$

where loads - axial force F , torque M_t and bending moment M_b - are related to strand deformations - axial strain ε , twist angle per strand unit length ϕ , and curvature χ by linear position (3.11). Homogenized non linear behaviour is derived by the load steps procedure exposed in the previous section.

Macro scale level: cord-rubber structure

We base present survey on mechanics of the simple straight strand; once properties for the trigonal equivalent cylinder are defined, (3.20), we are ready to implement its non linear elastic behaviour by meanings of Finite Element Method (FEM). Homogenization technique furnishes the overall response for the heterogeneous media; in such method local information is lost in a way to gain a more manageable model. Similarly, in a finite element approach, the trigonal equivalent cylinder gives the great advantage of using very few elements to realize strand models, even if it computes a large amount of wires disposed on multi scale arrangement (Multi Layered Strand). In the follow we present a FE model of a reinforcing fibre, it is made of two simple strands twisted together, non linear response is investigated as well as trigonal effects in a cord-rubber composite.

Description of the procedure for building-up the cord

In cord composites, trigonal effect takes place over different scales. We look now at the macro scale behaviour of a cord. Specifically a double simple strand is investigated. Such kind of reinforcing fibre consists of two 6+1 wires strands wrapped together with a lay angle α_f , Figure 3.10, strands are modeled by their equivalent cylinders, see previous section. System presents, thus, the intrinsic trigonality of each simple strand at micro scale level, and the trigonal effect due to double helical strand arrangement at meso scale level.

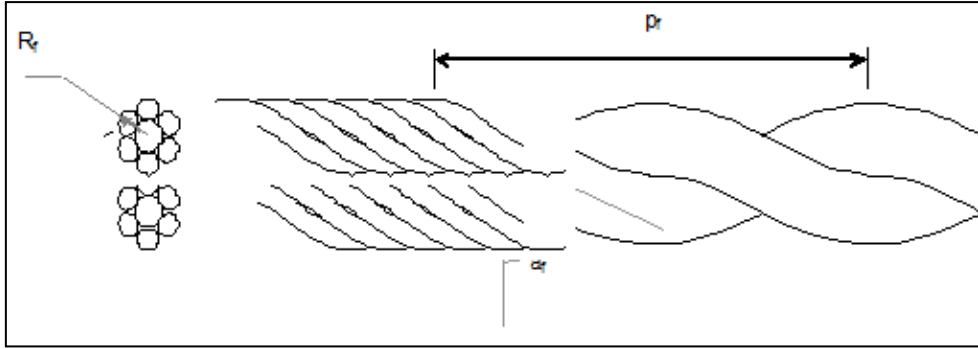


Fig. 3.10:

A parameter based procedure has been developed to realize the model of twisted cord. Ansys[®] batch mode allows to vary parametrically the geometries of the reinforcing fibre, i.e. single strand radius R_f and lay angle α_f , as well as load conditions and finite elements meshing size. Method starts with the automatic generation of the volume of the cord. In a way to avoid elements geometric degeneracy during the meshing process, fillet lines are used to merge the elliptical cross section of the two strands; value of the fillet radius is mesh size depending. A cylindrical reference system $\mathbf{r}, \boldsymbol{\theta}, \mathbf{z} \in \mathbf{R}^3$ is now considered, with \mathbf{z} axis coincident to cord axis. Merged area is then linearly extruded along $\boldsymbol{\theta}$ and \mathbf{z} axes by \bar{z} and $\bar{\theta}$ length values, providing that $\bar{z}/\bar{\theta} = \tan \alpha_f$ and $\bar{\theta} \ll 2\pi$, Figure 3.11; value of the length of extrusion is mesh size depending. The volume corresponds to two slices of cylinder of radius R_f with the axes tangent to the strand helical paths. Homogenized trigonal material properties for each one of the simple strands (3.13) are defined by considering a local frame cylindrical reference system $\mathbf{r}_s, \boldsymbol{\theta}_s, \mathbf{z}_s \in \mathbf{R}^3$, with \mathbf{z}_s axis coincident to the axis of the extruded cylinder. Indeed the elastic constants for the equivalent cylinder are introduced referring to the local reference system. The same extrusion is realized starting from the double ellipses cross section of the cord at $\mathbf{z} = \bar{z}$ generated before. Material properties are defined again referring to local cylindrical system of the new created slices of cylinder. Extrusion and material properties assignment goes on until a cord volume geometry of length p_f is obtained, where p_f is the cord twisting pitch.

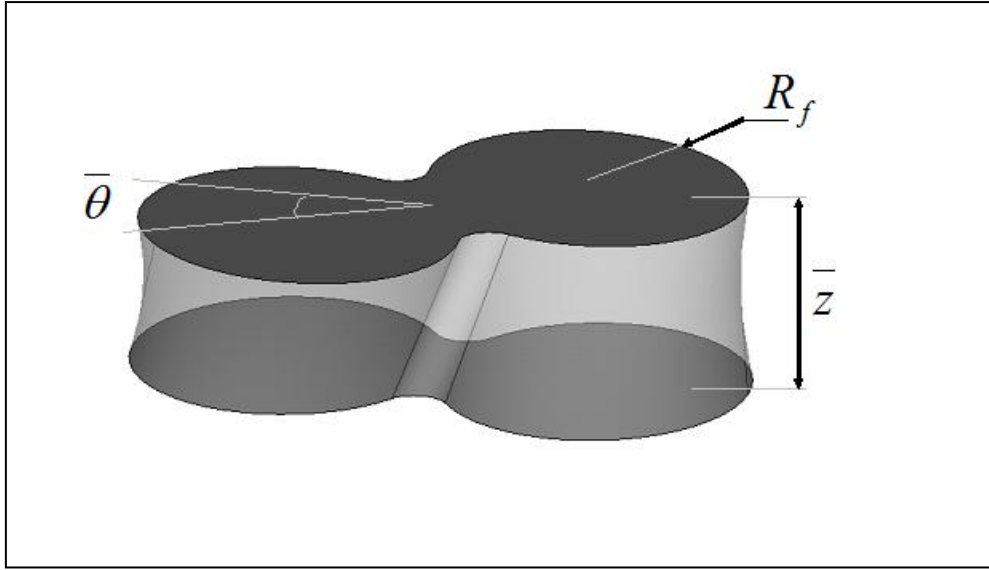


Fig.3.11:

Numerical simulations of the mechanical response of twisted cord-rubber composite

Preliminarily finite element analyse on cord model are performed, in a way to observe the effects of the trigonality at the meso scale level, i.e. double homogenized strands twisted together. Using the Ansys[®] software is realized an automatic procedure to mesh the model with three-dimensional, 8-node brick elements, Figure 3.12. A complete pitch length of the cord is realized and non linear elongation test are performed, both for fixed end condition and free rotation condition. Finite element non linear analyses perform by linear sub step; same procedure used for non linear Costello's approach is adopted. Axial deformation on the cord is applied in a number of steps high enough to ensure that condition on helix angle of the simple strands $|\Delta\alpha| \ll 1$ is preserved. At the end of each step cord reactions are evaluated and material properties and cord geometries, i.e. R_f and p_f , are updated. In force of single step linearity is then possible to write:

$$F_i = \sum_{j=1}^i F_j \quad (3.21)$$

$$M_{ii} = \sum_{j=1}^i M_{ij} \quad (3.22)$$

where i is the number of the i^{th} load step, and F_i and M_{ii} are the relative cord reaction forces, in terms of axial force and torque.

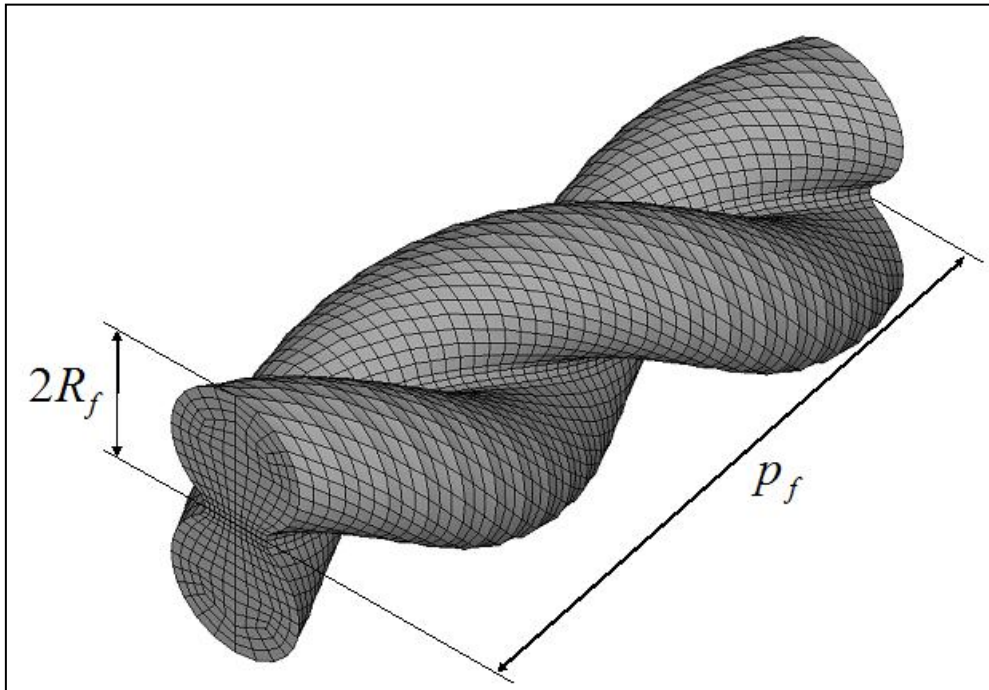


Fig. 3.12:

FEM Simulation and results

As stated before, twisted cords exhibit axial-torsion coupling due to its structural nature. This trigonal effect is due on one hand by the microstructural organization of internal filament and on the other by helical macroscale shaped.

Several authors have investigated the aforementioned coupling effect in cord-rubber composites by analytical and numerical procedures. *Kocak S. and Pidaparti RM.* (2000) have developed a finite-element model, that integrates a solid rubber element and a twisted cord element, which takes into account coupling effects of various deformations. They investigate the influence of cord shape on the load-deformation characteristics. Similar approach was used to evaluate the effect on the cord-rubber interface stresses distribution (*Pidaparti et al., 2001*).

In this paragraph the influence of twisted cord microstructure, on the mechanical response of composite, will be investigated through as FE approach; whereas the role of helical shape of cord will be neglected. Twisted cord behavior is based on numerical result of monoclinic compliance constants for trigonal cord obtained from the procedure discussed in the latter section. In fact starting from non-linear Costello's model and assuming small helix angle variation $|\Delta\alpha| \ll 1$, the numerical method allows to obtain for each small $\Delta\alpha^{i-th}$ the matrix constants C_{ij}^{i-th} of anisotropic response.

In order to validate the present approach a three-dimensional FE model, which consists in the trigonal "equivalent cylindrical" cord, reminiscent of trigonality, embedded in solid rubber matrix, has been developed.

The efforts spent to develop the analytical procedure, allow to simplify the geometry of model and bring numerical difficulties down, avoiding the use of advanced features of 3D CAD modeling (*Pidaparti et al.*, 2001).

To perform the finite element analysis on the homogenized and simple cylindrical cord-rubber models, the FE models were developed using the ANSYS® software. Finite element meshing of cord and rubber were done with three-dimensional, 8-node, brick element (SOLID185), that it also has mixed formulation capability for simulating deformations of nearly incompressible and fully incompressible hyperelastic materials.

Next, the finite element models were assigned the material properties: Mooney Rivlin hyperelastic form has been used to characterize the constitutive behavior of rubber matrix in both models; isotropic elastic constants were used to characterize the simple cylindrical cord; while the anisotropic constants C_{ij}^{i-th} for trigonal behavior have been invoked to setup the behavior of the homogenized cylindrical cord.

FE non linear analysis were performed under axial loading, considering for each load step the same axial displacement (taking into account that $|\Delta\alpha^{i-th}| \ll 1$) used for analytical procedure.

As first consideration the affect of trigonality on the mechanical response was analyzed comparing the response of a composite models with a simple isotropic cylindrical cord. As shown in the picture, the anisotropic behavior of cord reinforcement affect the response of composite: an axial-torsion coupling is highlighted (cfr Figure 3.13 *up*).

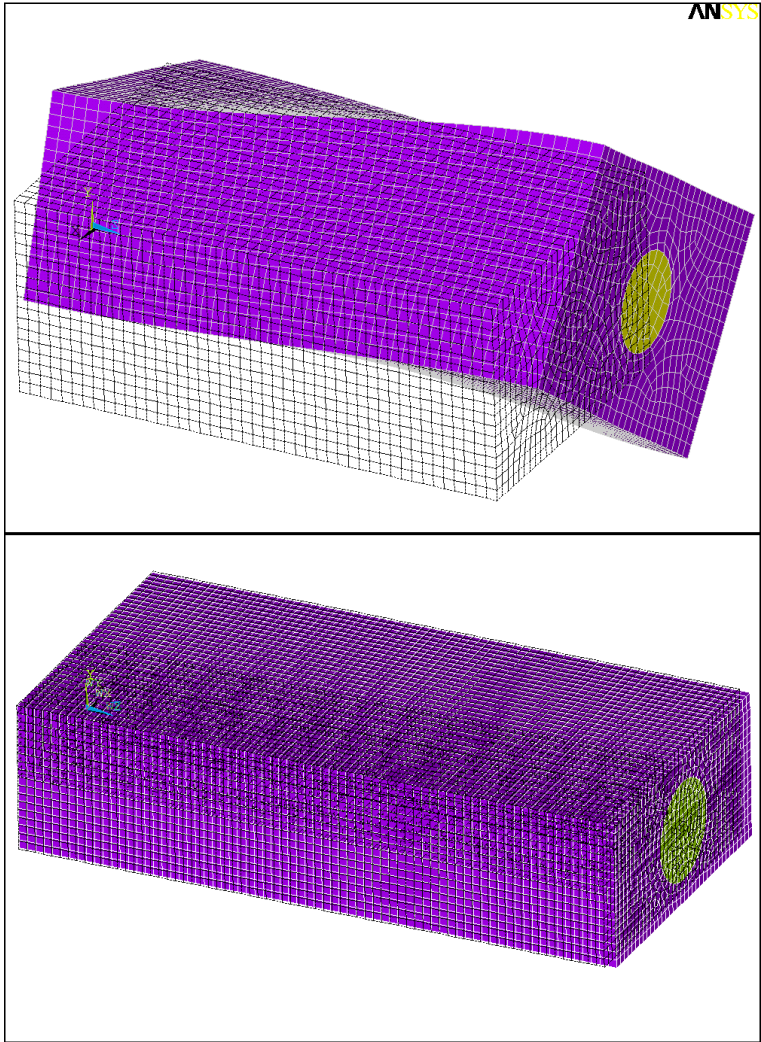


Fig. 3.13 Tensile-torsion coupling effect with the trigonal cord (*up*) and simple tensile behavior in isotropic case

Next step is to evaluate the amplitude of shear stress $\sigma_{r\theta}$, due to trigonal cord, at the cord-rubber interface, considering that in the case of isotropic cylindrical cord no shear stress arises at the interface, and the influence of its tensile-twisting behavior into the rubber matrix.

The picture highlights the no-zero stress values in the cord reinforcement and on its external surface, where the trend emphasizes the tension that grows inside the rope.

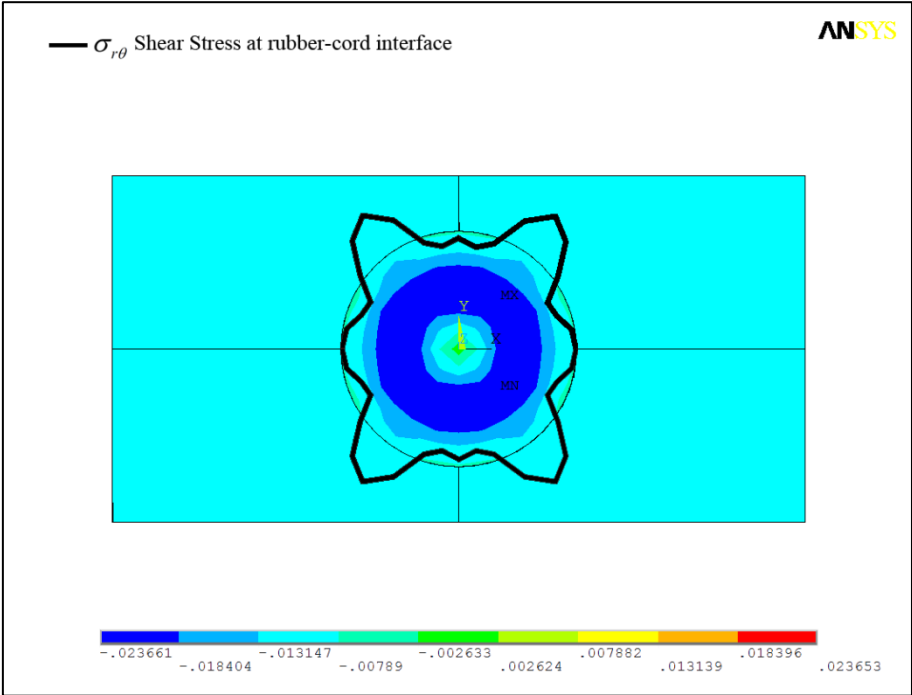


Fig. 3.14: Shear stress into the reinforcement and on the cord-rubber interface (black line)

The interface shear stresses is transferred into the surrounding rubber matrix As we can see the distribution of tension isosurfaces gives an idea on how this behavior expands inside into the matrix (cfr. Figure 3.14)

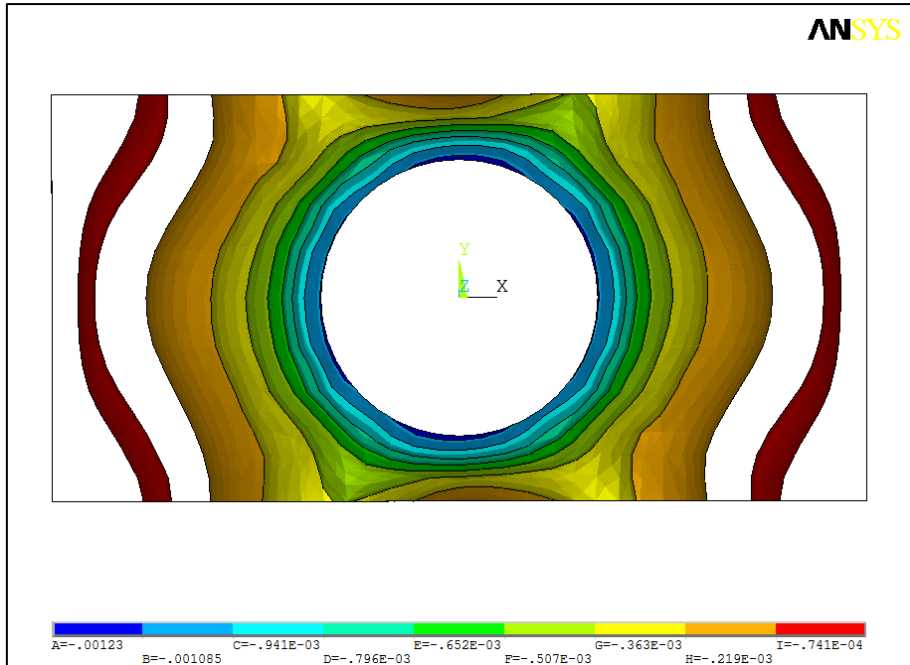


Fig. 3.15 Tension isosurfaces distribution into the rubber matrix

Title: A sensitivity analyses on fiber density

As state before, the use of fiber reinforced composite materials has found in recent years continually increasingly interest in design process of structures and structural elements encountered in engineering practice. The full advantages of such materials are obtained when fibers are distributed and oriented optimally with respect to the assumed objective behavior measure in the optimization process under actual loading conditions of the structure (*Dems K, 1996*). Mostly, to fulfill the optimal behavior of a certain structure and its loads, can modify some parameters of structural material, such as fiber plies thickness, fiber density, shape and orientation, stacking sequence etc. In this paragraph a study conducted to evaluate the effect of fiber density on rubber compound stress field is discussed. The model showed is based on the cord-rubber composite presented in the latter paragraph, where an anisotropic cylindrical cord is embedded by hyperelastic rubber matrix.

The sensitivity analysis has conducted on a specimen size fixed, where the reinforcement change in number (from 2 to 4 fibers). The results showed below refer to similar tensile boundary conditions.

The tensile-torsional coupling effect, due to anisotropical behavior of fibers, is highlighted by deformed shape of the three specimens taken into account (cfr figure 3.16),

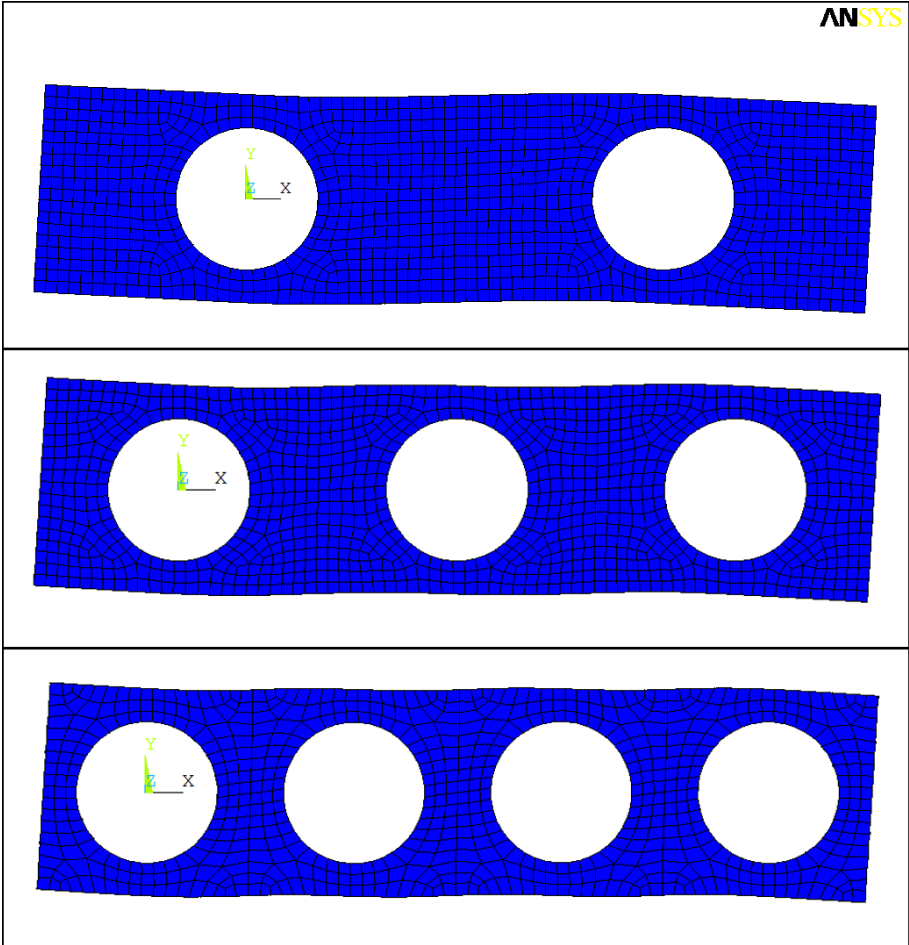


Fig.3.16 :

As already mentioned, the trigonal behavior of cord increases the stress field of rubber for the presence of transferred shear stress $\sigma_{r\theta}$. The first important result is represent in the picture below (cfr. Figure 3.17), where the distribution of cited stress, on the

mid plane of specimen, is plotted; and as we can see the stress gradients in the matrix increase with the increasing of fiber density.

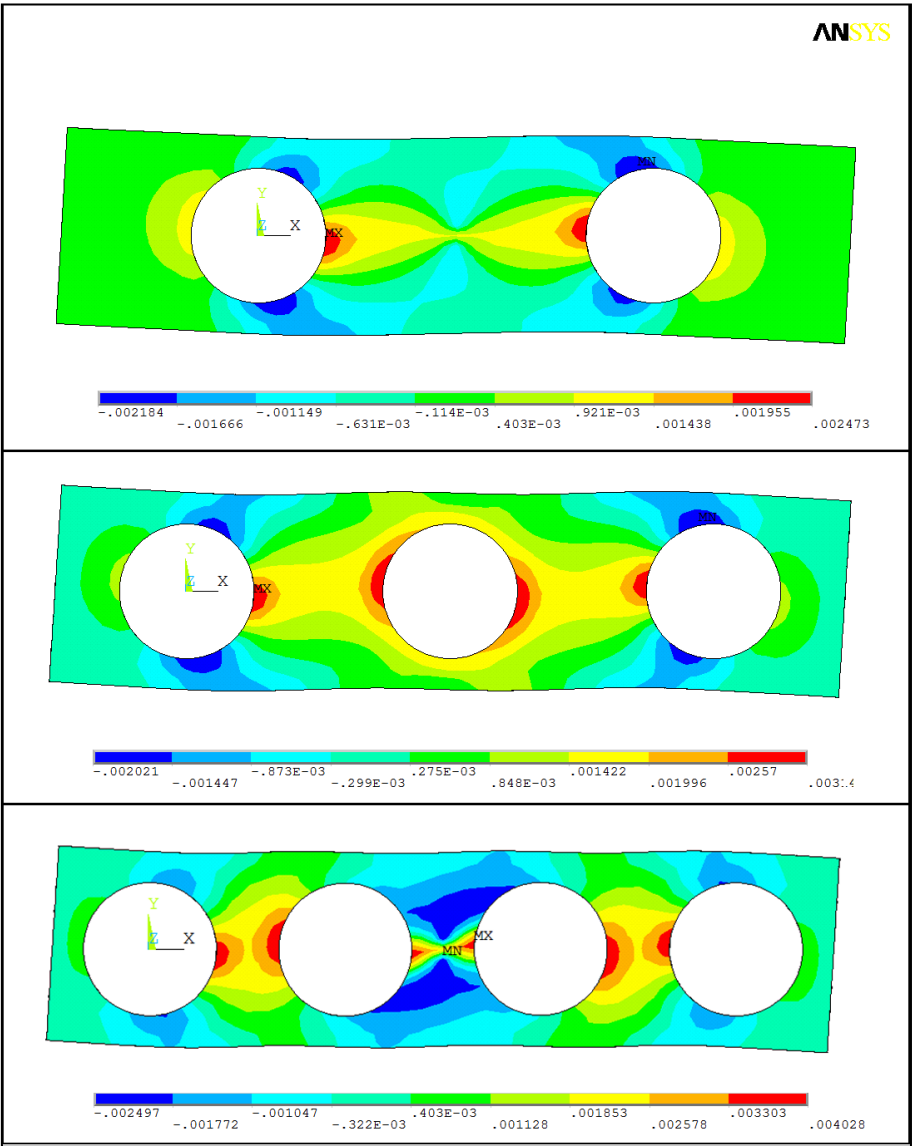


Fig. 3.17:

From the point of view of material strength the presence of high unexpected stresses value may lead to an increased risk of rubber fracture, particularly under cyclic loading.

To evaluate the affect of trigonal behavior of cords on the structure, the ratio between $\sigma_{r\theta}$ and σ_z , where the last ones are due to the stretch in load direction, is evaluated in the inter-fiber matrix space. As showed below (cfr. Figure 3.18) the $\frac{\sigma_{r\theta}}{\sigma_z}$ increases; in particular in the second and third case the shear stress values are greater than σ_z .

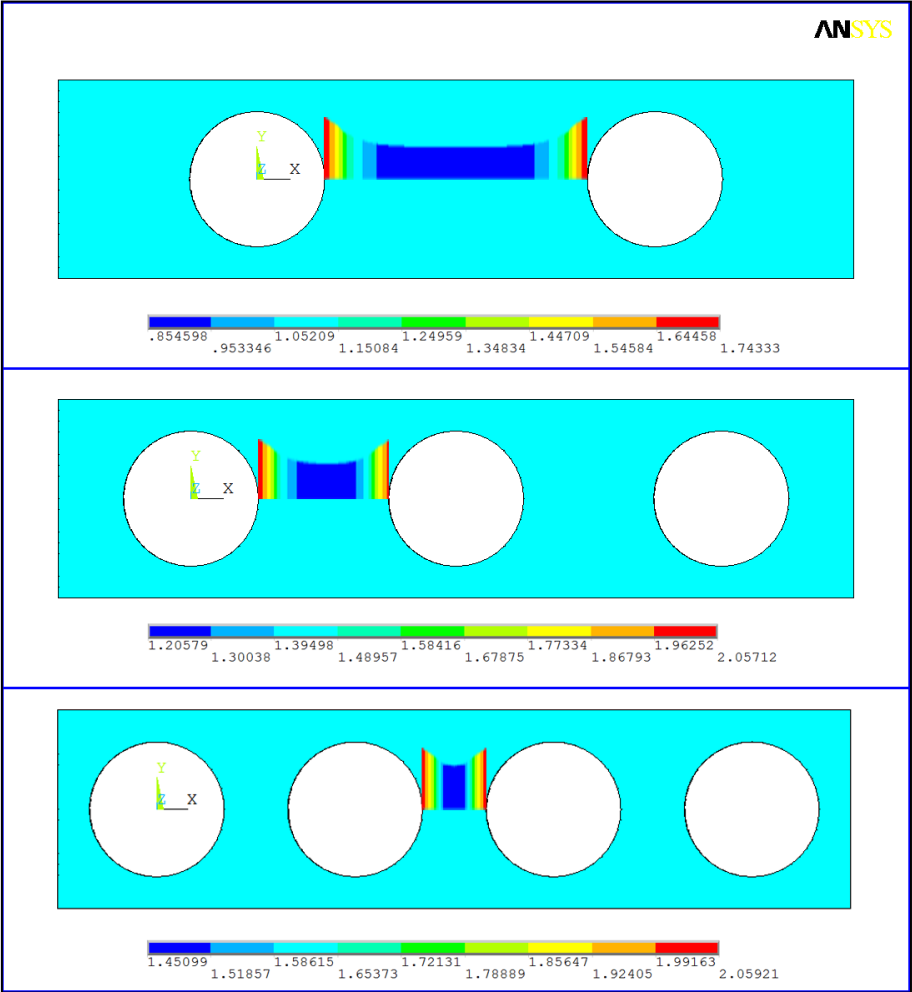


Fig. 3.18:

Conclusion

In this chapter the behavior of non-linear elastic cord-rubber composites has been investigated. The modeling activities, both analytical and Finite Elements Method (FEM) have been used to simulate and predict the tensile-torsional behavior of twisted cord embedded in a rubber matrix. The efforts spent to developed the analytical model

for twisting cables, allow us to simplify the numerical model and relative analyses introducing an homogenized constitutive behavior of cord. In particular, our attention is focused on two main results: the tension-twisting response of composite, and influence of fiber density on unexpected stress distribution due to the microstructural anisotropic behavior of cord. The results confirm that this multi-scale approach can be a good basis to characterize the complex behavior of pneumatic tire.

References

- Beach D and Schroeder J, An Overview of Tire Technology. Rubber World, 222 (6) 44-53 (2000)
- Clark, Composite theory applied to elastomers, University of Michigan (1989)
- Costello, G., (1990) Mechanical models of helical strands, Applied Mechanics Reviews, 50, 1-14
- Dems K., (1996) Sensitivity analysis and optimal design for fiber reinforced composite disks, Structural optimization 11,178-186
- Love, A E. H., (1944) A treatise on the mathematical theory of elasticity, 4th ed., New York: Dover Publications, Chapter XVIII-XIX, 381-426
- Luo, Chou, Proc. R. Soc. Lon. A 429, 569 (1990)
- Nawrocki, A., Labrosse, M., (2000) A finite element model for simple straight wire rope strand, Computer and Structures, 77, 345-369
- Payne et al., Rubb. Chem. & Techn. 44, 440 (1971)
- Pidaparti et al., Comp. Struc. 24, 291 (1993)
- Pidaparti et al., Comp. Struc. 34, 361 (1996)
- Pidaparti et al., Comp. Struc. 34, 361-369 (1996)
- Pidaparti et al., Comp. Struc. 52, 287 (2001)
- Pidaparti et al., Jour. Comp. Mat. 26 (2), 152 (1992)
- Sen A.K. (2008) Coated Textiles: principles and applications. Taylor & Francis. CRC Press.
- Shield and Costello, Jour. Appl. Mech. 61, 1-8 (1994)
- Shield and Costello, Jour. Appl. Mech. 61, 9-15 (1994)
- Utting, W., Jones, N., (1987a) Response of wire rope strands to axial tensile loads. Part I: Experimental results and theoretical predictions, International Journal of Mechanical Science, 29 (9), 605-61

- Utting, W., Jones, N., (1987b) Response of wire rope strands to axial tensile loads. Part II: Comparison of experimental results and theoretical predictions, International Journal of Mechanical Science, 29 (9), 621-36
- Walter, Patel, Rubb. Chem. & Techn. 52, 710 (1979)
- Walter, Rubb. Chem. & Techn. 51, 524 (1978)

Equation Chapter (Next) Section 1

CHAPTER IV

MECHANICAL RESPONSE OF FOOD PACKAGING POLYMERIC BI-LAYER FILMS UNDER HIGH PRESSURE

Introduction

In the last years considerable efforts have been spent on the mechanical behaviour of materials constituted by the coupling of different thin layers, with particular attention focused on delamination phenomena, interfacial failure and overall stiffness and strength of multi-layer films. A technological application where these issues are notably relevant is that of Novel Processing (NP) treatments of packaged food, recently introduced to improve safety, quality and shelf-life of foodstuff. In this framework, mechanical performances and structural integrity of multi-layer flexible polymer films used to package food remain a main concern. Among NPs, High Pressure Processing (HPP) is steadily gaining as a food preservation method that also preserves natural sensory and nutritional attributes of food with minimal quality loss. Packaged foods, processed by using this technique, maintain most of their original texture and nutritional qualities, additionally exhibiting an extended shelf-life. HPP applies high pressure (typically in the range of over a time frame of the order of minutes) to packaged foodstuff in order to significantly reduce the number of microorganisms as well as to deactivate enzymes by mechanically-induced mechanisms [1]. High pressure loads are exerted on packaged foodstuff by means of a pressurized confining fluid imprisoned in a vessel. The process consists of a preliminary heating of both confining fluid and packaging, followed by adiabatic pressurization. Typically high pressure pasteurization is performed at an initial temperature of while sterilization is conducted at higher initial temperature . Since the adiabatic pressurization process determines a monotonic increase of the initial temperature, the actual treatment temperature depends on the maximum attained pressure, with temperature rise. [2].

A suitable choice of a multi-layer packaging for HPP has to be performed in such a way that the treatment process does not affect package integrity as well as its functional properties. As a consequence, the packaging material and design should prevent irreversible deformation phenomena induced by high pressure and severe stress regimes. [3].

Literature experimental results highlight that several types of multilayer films are inappropriate for HPP due to the occurrence of delamination phenomena. In particular, bi-oriented PET/PP bilayer films as well as multilayer structures including aluminium foils or metalized layers show this type of failure mechanisms. [4]. These phenomena are expected to depend on the features of the materials employed to build up the multilayer structures and, in particular, on the thermo-mechanical properties of the coupled components forming the overall packaging structure.

From the mechanical standpoint, HPP can indeed kindle interfacial stresses between the different elements of multilayer structures as a result of the high pressure loading exerted by the pressure transmitting fluid, thus inviting delamination and extensive detachment phenomena. The mechanical analysis of multilayer systems under severe pressures generally requires to consider large displacements, deformation-induced and intrinsic film anisotropy and non linear stress-strain relationships, as well as visco-elastic and plastic responses. Also, special attention should be given to properly model bonding conditions at the layers interfaces taking into account cohesion and friction by means of ad hoc constitutive assumptions for the adhesives. Additional efforts are needed to overcome numerical difficulties arising from the strong difference between the characteristic (in-plane) size of the material – generally of the order of centimetres – and films thicknesses (of the order of tens of microns) that may lead to sometime insurmountable computational costs or very onerous in silico simulations aimed to determine interfacial stress and stress singularities between thin films [5].

Moreover, difficulties are also encountered when the mechanics of thin films is approached following an analytical way. In fact only a limited amount of scientific contributions furnish exact solutions to problems involving the mechanical response of these composite materials under specific load conditions. In this framework, Bufler [6] developed a rational method for the analysis of arbitrarily laminated elastic, isotropic or transversely isotropic hollow spheres under internal and/or external pressure, obtaining exact solutions and homogenized elastic moduli by using the Transfer Matrix Method. Ding and Chen [7,8], on the base of the three-dimensional Theory of Elasticity, investigated the non-axisymmetric free vibrations of isotropic spherical shells submerged in a compressible fluid medium, determining their natural frequencies, and Jiang et al. [9] studied the dynamic response of layered hollow spheres in closed form. Semi-analytical solutions constructed by invoking asymptotic methods are given by Lebon et al [10] for analysing some non-linear soft thin layers, while other literature efforts have been aimed to estimate indentation response of thin hard films on soft substrates [11], making reference to hypotheses of special (i.e. spherical) symmetry conditions.

Motivated by the scientific and practical interest in the mechanical response of polymeric thin films utilized for food packaging, this work intends to investigate on the mechanisms governing the delamination phenomena observed experimentally in multilayer films during HPP, in order to pave the way for optimal design of packaging structures. To make this, both analytical and Finite Element (FE) analyses of the process of HP treatment of pouches made of multilayer films and containing tap water have been performed. The results suggest that the development of inter-laminar normal and shear stresses as well as increase of stress fields within the constituents due to their differences in elasticity, i.e. Young moduli and Poisson ratios of the films, can be actually traced as responsible for localized delamination and failure phenomena.

In particular, in the present work experimental results of laboratory tests performed to obtain the stress-strain and thermal dilation properties of some polymeric films (PP, PET, OPA and PA) involved in the realization of multilayer food packaging, are firstly described and discussed in details.

Successively, in the framework of anisotropic linear elasticity, two preliminary ad hoc analytical solutions are constructed coherently with the experimental findings, making reference to simpler situations evoking the real case of the bi-layer food packaging under high pressure. Then, sensitivity analyses have been performed in order to analytically estimate inter-laminar shear stresses at the film interfaces and their magnitude with respect to specific geometrical and mechanical parameters, that is the ratios between elastic moduli and thicknesses of the coupled polymeric layers. In particular, a first analysis has been conducted under the hypothesis of plane-strain of the bi-layer film and a solution related to spatially varying load applied orthogonally to both the film sides has been found to simulate the effect of the high pressure on the compressive stress state developing inside the materials. As a result, the influence of pressure gradients, mechanical parameters and thicknesses of the coupled films on the inter-laminar shear stresses has been explored through sensitivity analyses, by demonstrating at the end that a best film coupling (measured as minimum ratio between inter-laminar shear and maximum stresses) can be obtained if is minimized the percentage difference between homogenized stiffness of the bi-layer material and the Young modulus of the basic film, PP in the specific case. The second exact solution is instead obtained for investigating the response of a multi-layer hollow cylinder filled by incompressible water and subject to external pressures and to a “spurious” bending regime which perturbs the symmetry so kindling inter-laminar shear stresses. The attention has then been focused on the variation of inter-laminar shears with the radius of the object, in order to predict the effects of the curvature of

the bi-layer film due to deformation-induced wrinkling or geometrical shape on the stress regime.

Both the above mentioned solutions have been used as a guidance for interpreting the results of the subsequently performed FE numerical simulations where both nonlinear behaviour of the materials and large displacements have been taken into account. Furthermore, a faithful modeling of the whole food package shape has been considered and the stresses within the polymeric layers are determined with respect to three different actual film couplings (PP/PET, PP/OPA and PP/PA), also experimentally investigated. In particular, the outcomes of two groups of FE-based analyses are presented. The first set of simulations has been focused on a sensitivity analysis aimed to determine the relation between stress fields and film elastic moduli ratios corresponding to differently coupled films. The second non-linear FE analysis has been conducted with respect to the sole PP/PET bi-layer, with the main interest in detecting possible wrinkling phenomena due to local strain gradients induced by severe pressures, ranging from 100 to 250 MPa.

The comparison of experimental evidences (i.e. film deformation and interfacial failure phenomena found in food-packages tested under high pressures) with numerical results is finally shown, highlighting a very good agreement between FE-based predictions and the actual response of the materials and also confirming the theoretical results which suggested to couple films with close mechanical properties to avoid failure. As a consequence, finally, on the basis of the mechanical analyses and the experimental findings, a rough heuristic measure of the “best coupling” in terms of lowest likelihood of interfacial failure is introduced and defined.

Experimental findings and problem statement

Capability of multilayer polymer films to withstand high pressure pasteurization and sterilization treatments was assessed by realizing pouches containing a food stimulant (tap water and small solid carrots) and submitting them to HP treatment similar to those performed on industrial scale. In particular, bilayer films were obtained by laminating commercial plastic films, i.e. cast polypropylene (PP), bioriented polyethyleneterephthalate (PET), bi-oriented polyamide (OPA) and cast polyamide (PA). Lamination was performed on industrial machines using several kinds of standard polyurethanic adhesives for food packaging applications. Three types of bilayer films were investigated, that is PET/PP, OPA/PP and PA/PP. In all cases the inner layer of the pouches (i.e. the one in contact with tap water) was PP, to guarantee the sealability of the package. Due to the production process, the four polymer films used to realize the bilayer structures are oriented, thus exhibiting a transversely

isotropic thermo-mechanical behavior. As a consequence, in the following, ‘machine direction’ or ‘longitudinal direction’ (L) and ‘transverse direction’ (T) are respectively parallel and orthogonal to the main axis of the film reel (which, in turn, corresponds to the main axis of the production equipment). All the polymers used in this study are semicrystalline and present crystalline, well ordered, domains surrounded by amorphous regions.

Pouches were obtained by sealing the three sides of a folded bi-layer film with a custom built heat sealing equipment. Heat sealing was performed by hot-bar welding, at a heat-seal bar temperature of 110-120°C, under an applied pressure of 4 atm (a force of 400N applied on a 150mmx10mm surface) exerted for 1-2s. Before sealing the fourth side of the pouches, they were filled with the selected food simulant and air was removed from the head space by vacuum pumping. The filled pouches were then subjected to high pressure treatments, performed in a pilot scale high pressure / high temperature unit at Wageningen UR (University and Research centre) - Food & Biobased Research, in Wageningen, The Netherlands. Typically, pressure can be built up to 700 MPa in 24 s.

Two types of HP treatments have been performed on pouches: pasteurization and sterilization. Tap water has been used as pressurizing medium. Sterilization was performed at three different pressures: 200, 500 and 700 MPa. Pasteurization was instead performed with a similar procedure, but at room temperature.

The performed tests indicate that all the three bilayer films are able to withstand the pasteurization treatment without displaying any evident mechanical failure. However, PET/PP pouches displayed evidence of localized delamination (see figures 4.1 a and b) after HP sterilization, with both food stimulants used, over the whole investigated pressures range. No delamination after HP sterilization was instead observed, even at 700 MPa, in the case of PA/PP (see figure 4.1 c) and was barely present in the case of OPA/PP (see figure 4.1 d), for both food simulants.

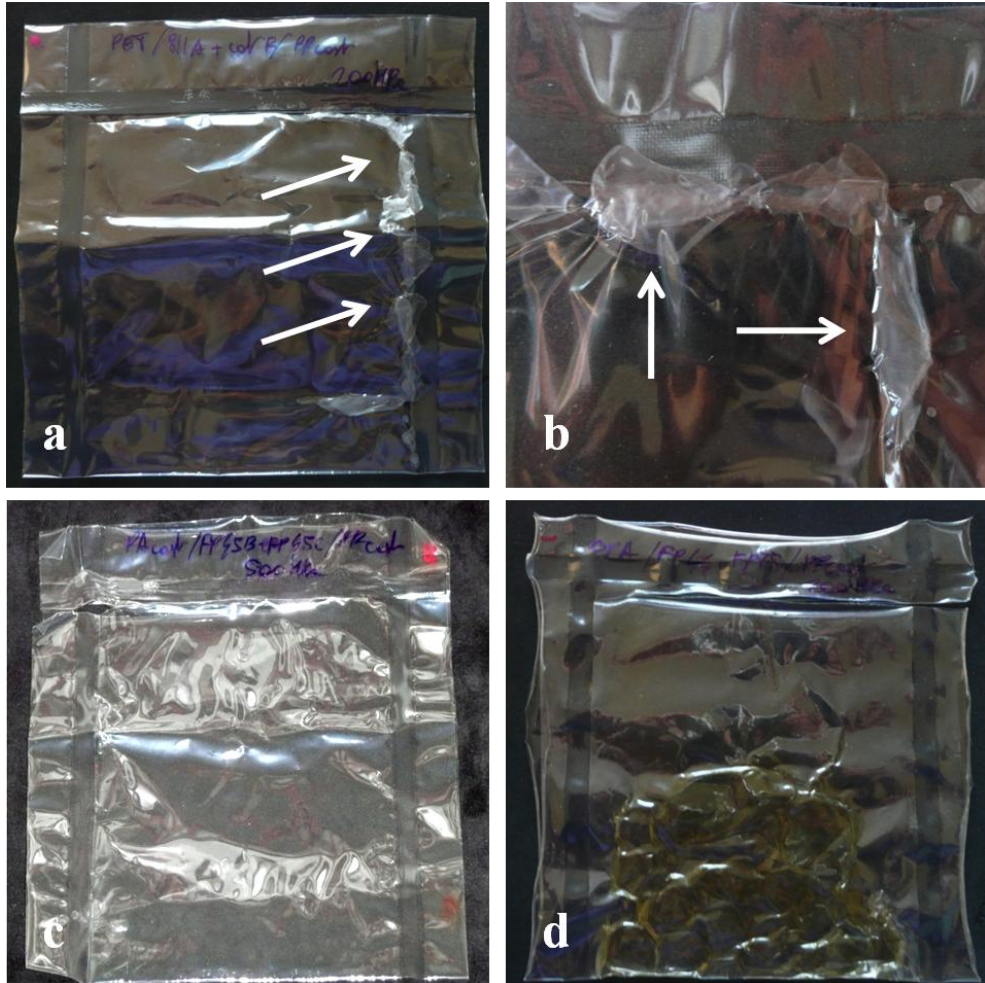


Figure 4.1. a) picture of a PET/PP pouch after HP sterilization treatment @200MPa (food stimulant: tap water), arrows indicating regions of delamination; b) detail of a delaminated region in PET/PP pouch with arrows highlighting the delamination zones; c) picture of a PA/PP pouch after HP sterilization treatment @500MPa (food stimulant: tap water); d) picture of a OPA/PP pouch after HP sterilization treatment @700MPa (food stimulant: solid carrots).

Since several phenomena occurring during sterilization treatment for PET/PP structures, due to difference in the thermal expansion coefficients of the two materials; differences in the mechanical behavior of the two films making up the multilayer structure (i.e. stiffnesses in the elastic regime) and in their dependence on temperature and pressure; several experimental tests on materials are been made to understand their affect.

For example the linear dilatational behavior of the four types of single layer films was determined experimentally in the L, T and 45° directions in the temperature range 20 ÷ 120 °C of interest in HP treatments, to understand the effect of film thermal

properties. To evaluate the effect of mechanical behavior of the single films, experimental mechanical tests was performed at 25 and 100 °C at atmospheric pressure in the three main directions. Stress-strain curves were obtained for elongational deformation determining the values of Young modulus in the elastic regime. The measured values are summarized in tables 1a,b.

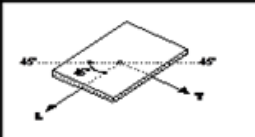
It is evident from the tables that, at 25°C, the values of the moduli for PP are close to those of PA. Differences are, instead, significant when comparing PP with OPA to become even more relevant for the case of PET. When considering the values of the moduli at 100°C, the largest differences are still found for the PP/PET coupling, while both PA and OPA display values of moduli which are close to those of PP.

Average values for the Young moduli, \bar{E} , of the bi-layer films, also reported in Tables 1a,b, have been calculated in each direction by assuming the rule of mixtures, according to the following equation:

$$\bar{E} = E_{PP} \frac{l_{PP}}{l_{TOT}} + E_i \frac{l_i}{l_{TOT}}$$

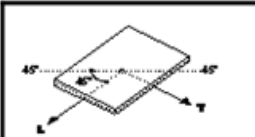
where E_{PP} and l_{PP} indicate, respectively, modulus and thickness of PP film, E_i and l_i represent, respectively, modulus and thickness of the film coupled to PP to form the bi-layer film and l_{TOT} is the total thickness of the multi-layer structure (thickness of the adhesive layer being assumed negligible). It is worth noticing that, for processing reasons, films are always laminated by matching the machine direction of the two layers.

Examination of results reported in tables 1a,b suggest that a possible cause for delamination might be related to differences in mechanical behavior. This conjecture will be deeply discussed and supported in following sections dealing with analytical and numerical simulations.



			PET [12μm]			OPA [15μm]			PA [20μm]		
			L	T	45	L	T	45	L	T	45
			2940	2750	2640	2240	2000	2350	660	780	785
PP [50μ m]	L	380	870			810			460		
	T	300		770			690			435	
	45	345			790			810			470

Table 1a. Young moduli at 25°C determined for the four films in the three main directions. Small sized fonts refer to the modulus of the single film, while large sized fonts refer to the bi-layer structures.



			PET [12μm]			OPA [15μm]			PA [20μm]		
			L	T	45	L	T	45	L	T	45
			2900	2700	1400	1400	520	140	200	155	170
PP [50μ m]	L	170	700			450			180		
	T	120		620			210			130	
	45	170			410			165			170

Table 1b. Young moduli at 100°C determined for the four films in the three main directions. Small sized fonts refer to the modulus of the single film, while large sized fonts refer to the bi-layer structures.

Evaluation of the effect of pressure on T_g is generally investigated by performing high pressure dilatometric experiments on molten polymers. Temperature is decreased at a controlled rate isobarically evaluating the change of specific volume. The molten state of the samples, insures that the state of stress in the material is a uniform, isotropic compression. T_g is marked by a change in slope of the specific volume vs T curve.

Similar tests have been performed also on the polymers used in this study by means of a high pressure dilatometer (GNOMIX, Boulder CO, USA), in which a hydrostatic pressure is applied to the sample by means of a confining fluid (mercury, in this case), but the outcome of those results are not reported in this work.

To evaluate the effect of mechanical strength of adhesive layer, several adhesives with different mechanical properties, where used to realize the three laminates, but it was observed that HP sterilization treatments resulted always in the delamination of only PET/PP structures, whatever was the adopted adhesive.

In conclusion, the experimental findings and the physical interpretation of the possible causes of failure support the hypothesis that the difference in delamination behavior

among the three investigated bi-layer structures can be mainly ascribed to the mismatch between the mechanical moduli of the two laminated films. As a consequence, the following sections are aimed at demonstrating, by rigorous arguments, the role played by the mechanical properties of the polymer films in determining different level of interlaminar stresses which act as driving force for delamination failure.

Sensitivity analyses and qualitative results based on exact solutions

Based on the above illustrated findings and the corresponding physical interpretation, it can be inferred that the delamination phenomenon is mainly determined by differences in mechanical properties of coupled films.

As a matter of fact, interfacial stresses responsible for delamination may result from the combination of both normal and shear stresses. Since high pressure applied on the bi-layer structure induces prevalent compressive normal stress fields at the interface, it is expected that delamination is determined only by shears.

With the aim of performing a sensitivity analysis to detect the influence of mechanical and geometrical factors on the occurrence of interfacial shear stresses, two analytical solutions have been constructed in which the role played by film curvature, load distribution and differences in elastic moduli is investigated.

In particular, the first analytical solution refers to the simple case of a rectangular bi-layer film where self equilibrated and spatially varying pressures are applied at the top and bottom sides of the composite sheet. The closed-form elastic solution is here determined in order to highlight the influence of the spatial gradients of the pressure – which can locally appear – on the interfacial stresses, accounting for differences in thicknesses and elastic moduli of the coupled materials.

The second exact solution treats instead the problem of a bi-layer hollow cylinder filled by an incompressible fluid, say water, under the combined action of external pressure and bending. This solution has the aim of simulating the ideal case of a food package filled by a fluid and loaded by high pressure, perturbed by a bent regime that kindles inter-laminar shear stresses across the films. The effects on the stress field of the radius of the ideal cylindrical package and of the bending deformation are analysed, to evoke the real case where local changes of curvature of the bi-layer film are induced by wrinkling phenomena. As in the first solution, the role played by the different stiffness of the films on the interfacial shear stresses is examined.

These analyses are of help in supplying a qualitative guidance to understand the effect of mismatch in geometrical and mechanical properties on the shear stress development in the actual situation of a food package under HP. The complex stress regime arising

in the case of real multi-layer packages can be indeed envisaged as a combination of the simpler ideal situations described through the exact solutions. However, large deformations, non-linear effects and real food package geometrical complexity will be considered in Section 4. of the present work, where Finite Element based numerical simulations and comparison with experimental results will be performed.

Two-layer film with spatially varying pressure symmetrically applied on the top and bottom sides

Let us assume a Cartesian coordinate system $\{0, x_1, x_2, x_3\}$ and consider a bi-layer film constituted by two rectangular thin sheets made of different linearly elastic orthotropic materials, perfectly bonded at the interface which lies on the $x_1 - x_2$ plane. Let w and $2L$ be the width and the length of the bi-layer film, measured along the x_2 and x_1 directions, respectively, and denote with t^+ and t^- the thicknesses of the constituent films placed at the top and bottom positions with respect to the plane $x_3 = 0$.

If self-equilibrated – and symmetrically distributed with respect to the $x_2 - x_3$ plane – pressures act on both top and bottom sides of the object as follows

$$p^\pm(x_1) = \mp p e^{-\alpha x_1}, \quad \forall x_1 \in [0, L], \quad x_3 = \pm t^\pm \quad (4.1)$$

p being the maximum pressure and $\alpha \in \mathbb{R}^+$ a parameter governing the spatial gradient of the load, the solution of the elastic problem can be searched in plane-strain in the form

$$u_1^\pm(x_1, x_3) = -\frac{C_{55}^\pm \phi_{,11}^\pm + 2C_{33}^\pm \phi_{,33}^{(i)\pm}}{2C_{13}^\pm + C_{55}^\pm}, \quad u_2^\pm = 0, \quad u_3^\pm(x_1, x_3) = \phi_{,13}^\pm \quad (4.2)$$

where commas denote differentiation, $\phi^\pm(x_1, x_3)$ is an unknown displacement-potential function and C_{ij}^\pm represent the elastic coefficients, in contracted Voigt notation, of the orthotropic films whose planes of material symmetry are assumed be coincident with the planes of the Cartesian reference frame. However, under the hypothesis of isotropy of both the materials and by invoking the geometrical compatibility conditions

$$2\varepsilon_{ij}^\pm = u_{i,j}^\pm + u_{j,i}^\pm \quad (4.3)$$

the nonzero strain components take the form

$$\varepsilon_{11}^{\pm} = -\frac{\mu^{\pm}\phi_{,111}^{\pm} + 2\mu^{\pm} + \lambda^{\pm} \phi_{,331}^{\pm}}{\mu^{\pm} + \lambda^{\pm}}, \quad \varepsilon_{33}^{\pm} = \phi_{,331}^{\pm}, \quad \varepsilon_{13}^{\pm} = \frac{\lambda^{\pm}\phi_{,113}^{\pm} - 2\mu^{\pm} + \lambda^{\pm} \phi_{,333}^{(i)}}{2\mu^{\pm} + \lambda^{\pm}} \quad (4.4)$$

and the corresponding not vanishing stresses are

$$\begin{aligned} \sigma_{11}^{\pm} &= 2\mu^{\pm}\varepsilon_{11}^{\pm} + \lambda^{\pm}(\varepsilon_{11}^{\pm} + \varepsilon_{33}^{\pm}), & \sigma_{22}^{\pm} &= \lambda^{\pm}(\varepsilon_{11}^{\pm} + \varepsilon_{33}^{\pm}), & \sigma_{33}^{\pm} &= \\ &= 2\mu^{\pm}\varepsilon_{33}^{\pm} + \lambda^{\pm}(\varepsilon_{11}^{\pm} + \varepsilon_{33}^{\pm}), & \sigma_{13}^{\pm} &= 2\mu^{\pm}\varepsilon_{13}^{\pm} \end{aligned} \quad (4.5)$$

with elastic coefficients in the eq (4.2) reduced to

$$\begin{aligned} C_{33}^{\pm} &= 2\mu^{\pm} + \lambda^{\pm}, & C_{13}^{\pm} &= \lambda^{\pm}, & C_{55}^{\pm} &= 2\mu^{\pm}, & 2\mu^{\pm} &= \\ &= E^{\pm} / (1 + \nu^{\pm}), & \lambda^{\pm} &= \nu^{\pm}E^{\pm} / [(1 + \nu^{\pm})(1 - 2\nu^{\pm})] \end{aligned} \quad (4.6)$$

in which E^{\pm} and ν^{\pm} represent the Young moduli and the Poisson ratios, respectively. In the absence of body forces, by virtue of the eqs. (4.2), (4.5) and (4.6), the equilibrium implies that the potential $\phi^{\pm}(x_1, x_3)$ must be bi-harmonic, i.e.

$$\sigma_{ij,j}^{\pm} = 0 \Rightarrow \nabla^4 \phi^{\pm}(x_1, x_3) = 0 \quad (4.7)$$

Based on the form of the applied pressures (4.1), the solution can be then found by separating the variables, thus obtaining

$$\phi^{\pm}(x_1, x_3) = \varphi(x_1) \times \psi(x_3) = e^{-\alpha x_1} \times [(A^{\pm} + B^{\pm}x_3) \cos \alpha x_3 + (C^{\pm} + D^{\pm}x_3) \sin \alpha x_3] \quad (4.8)$$

where the Eulero's formulas have been employed and $\{A^{\pm}, B^{\pm}, C^{\pm}, D^{\pm}\}$ represent eight coefficients to be determined by imposing the following interfacial and boundary conditions

$$\begin{aligned} x_3 = \pm t^{\pm} &\rightarrow \sigma_{33}^{\pm} = -p e^{-\alpha x_1}, & \sigma_{13}^{\pm} &= 0 \\ x_3 = 0 &\rightarrow \sigma_{33}^{+} - \sigma_{33}^{-} = 0, & \sigma_{13}^{+} - \sigma_{13}^{-} &= 0, & u_1^{+} - u_1^{-} &= 0, & u_3^{+} - u_3^{-} &= 0 \end{aligned} \quad (4.9)$$

The equations (4.9) constitute a linear algebraic system of eight equations in the eight unknowns $\{A^{\pm}, B^{\pm}, C^{\pm}, D^{\pm}\}$ and can be thus solved in closed form, as well as numerically.

When these solutions are specialized to bi-layer films characterized by PA, PET and OPA all coupled with a PP sheet, it is possible to investigate how the stress fields

parametrically change with a measure, denoted with δE , of the percentage differences in mechanical properties of the component layers defined as follows

$$\delta E \equiv \left| \bar{E} - E_{PP} \right| \times E_{PP}^{-1} \quad (4.10)$$

where \bar{E} is the standard Voigt homogenized Young modulus of the bi-layer film and E_{PP} is the PP Young modulus.

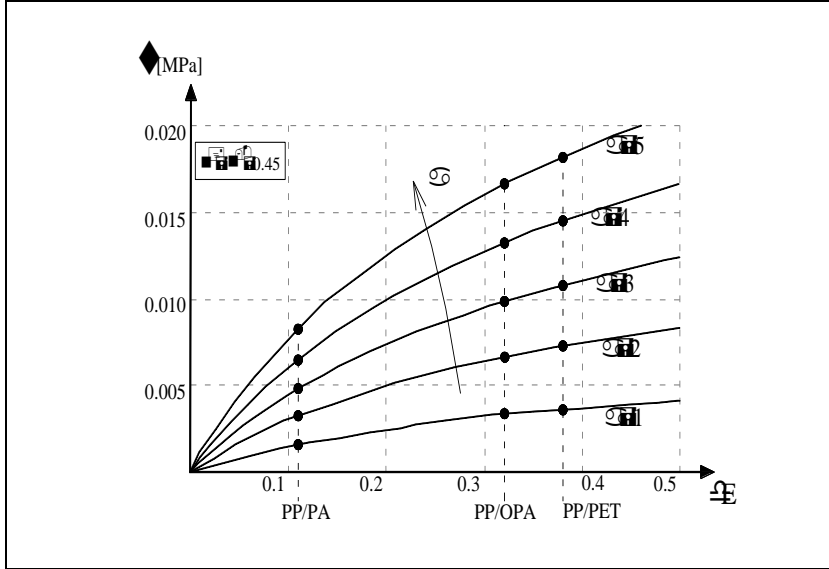


Fig. 4.2a: normalized maximum shear stress versus δE

Figures 4.2a and 4.2b show the normalized maximum shear stress, $\tau \equiv p^{-1} \times \max_{x_i \in [0, L]} \{\sigma_{13}\}$, versus δE , evidencing how interlaminar shear stress monotonically increases with δE . This trend is also confirmed for values of the pressure gradient greater than zero, at a prescribed value of Poisson ratios of the two coupled films (see Figure 4.2a) and for different ratios of the Poisson moduli, ν^+ / ν^- , at a vanishing average pressure gradient (see Figure 4.2b).

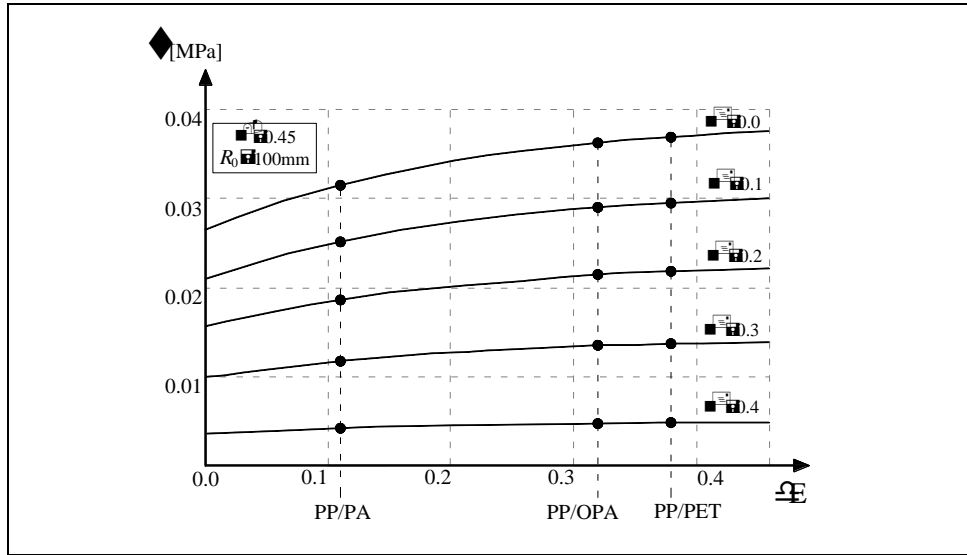


Fig. 4.2b

It is worth to highlight that the lowest value of the interlaminar shear stress is always attained in the case of PP/PA coupling, in this way confirming the experimental findings anticipated in Section 2.

Spurious bending in a bi-layer hollow cylinder filled with water and subject to external pressure

In a cylindrical coordinate system $\{r, \vartheta, x_3\}$, let us consider an object constituted by two cylindrical homogeneous and isotropic perfectly bonded hollow phases with axis x_3 , filled by an incompressible fluid and subjected to combined external uniform pressure and bending moment applied at the ends. The linearity of the problem allows to search the solution by invoking the superposition principle, that is writing the displacement as the sum of the axis-symmetrical solution – i.e. external pressure, p^+ , acting on confined water – and that related to the sole bending moment, M . Coherently with the above introduced notations, the outer and the inner films of the bi-layer structure will be denoted with the apex “+” and “–”, respectively, and the displacement, strain, stress and elastic components referred to the cylindrical reference frame. The geometry of the problem is then completely described by the radius at the interface between the constituent layers, R , and by the outer and inner radii, $R^+ = R + t^+$ and $R^- = R - t^-$, t^\pm being the thicknesses of the external and internal layers, respectively.

External Pressure and incompressible fluid filled the compound hollow cylinder

In linear isotropic elasticity, it has been demonstrated that axis-symmetrical solutions can be all derived by the Love's function [Love], also in case of multi-layer objects [Fraldi et al]. By invoking these results, the displacement field for a two-phase hollow cylinder subjected to uniform inner and outer pressures, the inner pressure being exerted by the incompressible fluid, can be written for both the layers as

$$u_r^\pm = A^\pm r + B^\pm r^{-1}, \quad u_\vartheta = 0, \quad u_3 = \varepsilon x_3 \quad (4.11)$$

where $\{A^\pm, B^\pm, \varepsilon\}$ are coefficients to be determined by means of the boundary conditions

$$\begin{aligned} r = R^- &\rightarrow 2u_r^- = -\varepsilon R^-, & r = R^+ &\rightarrow \sigma_{rr}^+ = -p^+ \\ r = R &\rightarrow \sigma_{rr}^+ - \sigma_{rr}^- = 0, & u_r^+ - u_r^- &= 0 \end{aligned} \quad (4.12)$$

$$\int_0^{2\pi} \left(\int_{R^-}^R \sigma_{33}^- r dr + \int_R^{R^+} \sigma_{33}^+ r dr \right) d\vartheta = F,$$

where F is the axial force resultant at the object bases and the first equation at the left side in (4.12) representing the incompressibility of the water, if second order and higher terms of deformation are neglected. Thus, by virtue of (4.11), compatibility equations (4.3) in cylindrical coordinates give

$$\begin{aligned} \varepsilon_{rr}^\pm &= u_{r,r}^\pm = A^\pm - B^\pm r^{-2}, & \varepsilon_{\vartheta\vartheta}^\pm &= r^{-1} u_r^\pm = \\ &= A^\pm + B^\pm r^{-2}, & \varepsilon_{33}^\pm &= u_{3,3}^\pm = \varepsilon, & \varepsilon_{\vartheta 3}^\pm &= \varepsilon_{r3}^\pm = \varepsilon_{r\vartheta}^\pm = 0 \end{aligned} \quad (4.13)$$

and, from (4.13), the constitutive equations for isotropic materials furnish the stresses

$$\sigma_{ij}^\pm = 2\mu^\pm \varepsilon_{ij}^\pm + \delta_{ij} \lambda^\pm \text{tr} \boldsymbol{\varepsilon}^\pm, \quad i, j \equiv \{r, \vartheta, 3\} \quad (4.14)$$

where δ_{ij} is the Kronecker delta, $\text{tr} \boldsymbol{\varepsilon}^\pm = (\varepsilon_{rr}^\pm + \varepsilon_{\vartheta\vartheta}^\pm + \varepsilon_{33}^\pm)$. It is easy to verify that the stresses (4.14) automatically satisfy the equilibrium equations at the left in (4.7), written in cylindrical coordinates. Moreover, it is worth to notice that, independently from the differences in terms of elastic moduli between the two films, eqs. (4.13) and (4.14) lead to find

$$\sigma_{\vartheta 3}^\pm = \sigma_{r3}^\pm = \sigma_{r\vartheta}^\pm = 0 \quad (4.15)$$

and thus no inter-laminar shear stresses occur for the sole presence of pressures in the object. However, a little amount of imperfection of the cylinder geometry or of the loads might perturb the symmetry of the problem, thus kindling inter-laminar shear stresses. This event is taken into account below by analyzing the response of the bi-layer cylinder under the action of a “spurious” bending.

Bending moment acting on the object ends

In the case of uniform bending moment the geometry of the object without \mathcal{G} -boundaries implies the absence of free terms in \mathcal{G} for displacements, stress and strain fields, which have to additionally be single-valued and continuous functions and hence exhibit periodicity on \mathcal{G} . Inspired by the St. Venant solutions and considering the symmetry condition due to the bending moment M acting, without loss of generality, on the $\mathcal{G} = \pi/2$ plane, it is therefore natural to seek a general solution of the problem by assuming for each layer the displacements in the following form:

$$\begin{aligned}
 u_r^\pm &= \sum_{k=0}^3 f_k^\pm(r) x_3^k \sin \mathcal{G} = \left[f_0^\pm(r) + f_1^\pm(r) x_3 + f_2^\pm(r) x_3^2 + f_3^\pm(r) x_3^3 \right] \sin \mathcal{G} \\
 u_g^\pm &= \sum_{k=0}^3 g_k^\pm(r) x_3^k \cos \mathcal{G} = \left[g_0^\pm(r) + g_1^\pm(r) x_3 + g_2^\pm(r) x_3^2 + g_3^\pm(r) x_3^3 \right] \cos \mathcal{G} \\
 u_3^\pm &= \sum_{k=0}^3 h_k^\pm(r) x_3^k \sin \mathcal{G} = \left[h_0^\pm(r) + h_1^\pm(r) x_3 + h_2^\pm(r) x_3^2 + h_3^\pm(r) x_3^3 \right] \sin \mathcal{G}
 \end{aligned} \tag{4.16}$$

where $\{f_k^\pm(r), g_k^\pm(r), h_k^\pm(r)\}$ represent twelve unknown functions. If $\mathbf{u}^\pm \equiv \{u_r^\pm, u_g^\pm, u_3^\pm\}$, μ^\pm and λ^\pm are the Lamé moduli, $\text{div} \mathbf{u}^\pm = u_{r,r}^\pm + r^{-1} u_r^\pm + r^{-1} u_{g,g}^\pm + u_{3,3}^\pm$ is the divergence of the displacement field and $\nabla^2 = \partial/\partial r^2 + r^{-1} \partial/\partial r + r^{-2} \partial/\partial \mathcal{G} + \partial/\partial x_3^2$ represents the Laplace differential operator, the displacements (4.16) have to obey the Navier-Cauchy equilibrium equations

$$\begin{cases}
 \mu^\pm \nabla^2 u_r^\pm - 2r^{-2} u_{g,g}^\pm - r^{-2} u_r^\pm + \mu^\pm + \lambda^\pm \text{div} \mathbf{u}^\pm_{,r} = 0 \\
 \mu^\pm \nabla^2 u_g^\pm + 2r^{-2} u_{r,g}^\pm - r^{-2} u_g^\pm + \mu^\pm + \lambda^\pm r^{-1} \text{div} \mathbf{u}^\pm_{,g} = 0 \\
 \mu^\pm \nabla^2 u_3^\pm + \mu^\pm + \lambda^\pm \text{div} \mathbf{u}^\pm_{,3} = 0
 \end{cases} \tag{4.17}$$

This implies that the unknown functions $\{f_k^\pm(r), g_k^\pm(r), h_k^\pm(r)\}$ must satisfy a system of twelve differential equations, whose solution – through some ordinary algebraic

passages – can be found in closed form and the displacements (4.16) rewritten more explicitly as follows

$$\begin{aligned}
u_r^\pm &= \left[U_0^\pm \log r - U_1^\pm r^{-2} + U_2^\pm - U_3^\pm + U_4^\pm x_3 + U_5^\pm x_3^2 + U_6^\pm + U_7^\pm r^2 \right] \sin \vartheta \\
u_\vartheta^\pm &= \left[U_0^\pm \log r + U_1^\pm r^{-2} + U_2^\pm + U_3^\pm + U_4^\pm x_3 + U_5^\pm x_3^2 + U_8^\pm - U_6^\pm r^2 \right] \cos \vartheta \\
u_3^\pm &= - U_4^\pm + 2U_5^\pm x_3 r \sin \vartheta
\end{aligned} \tag{4.18}$$

from which strains and stresses can be finally derived by using the eqs. (4.3) and (4.14), respectively, finding $\sigma_{r3}^\pm = \sigma_{\vartheta 3}^\pm = 0$. U_i^\pm are coefficients among which there are the relations

$$U_3^\pm = \frac{\lambda^\pm + \mu^\pm}{2(3\lambda^\pm + \mu^\pm)} U_0^\pm, \quad U_8^\pm = \left(\frac{3\lambda^\pm + 5\mu^\pm}{\lambda^\pm - \mu^\pm} \right) U_7^\pm, \quad U_6^\pm = \frac{\lambda^\pm}{2(\lambda^\pm + \mu^\pm)} U_5^\pm \tag{4.19}$$

and to be determined by imposing the following boundary conditions on the cylindrical surfaces

$$\begin{aligned}
r = R, \quad \forall i \equiv \{r, \vartheta, 3\} &\quad \rightarrow \quad u_i^+ = u_i^-, \quad \sigma_{ri}^+ = \sigma_{ri}^- \\
r = R^\pm \equiv R \pm t^\pm, \quad \forall i \equiv \{r, \vartheta\} &\quad \rightarrow \quad \sigma_{ri}^\pm = 0
\end{aligned} \tag{4.20}$$

and the integral ones at the object extremities

$$\begin{aligned}
\int_0^{2\pi} \left(\int_{R^-}^R \sigma_{3i}^- r dr + \int_R^{R^+} \sigma_{3i}^+ r dr \right) d\vartheta = 0, \quad \int_0^{2\pi} \left(\int_{R^-}^R \sigma_{\vartheta 3}^- r^2 dr + \int_R^{R^+} \sigma_{\vartheta 3}^+ r^2 dr \right) \sin \vartheta d\vartheta = 0 \\
\int_0^{2\pi} \left(\int_{R^-}^R \sigma_{33}^- r^2 dr + \int_R^{R^+} \sigma_{33}^+ r^2 dr \right) \sin \vartheta d\vartheta = M, \quad \int_0^{2\pi} \left(\int_{R^-}^R \sigma_{33}^- r^2 dr + \int_R^{R^+} \sigma_{33}^+ r^2 dr \right) \cos \vartheta d\vartheta = 0
\end{aligned} \tag{4.21}$$

FE simulations of actual food package under high pressure and comparison with experimental evidences

The analytical solutions presented in Section 3. supply information about possible interfacial shear stresses responsible of delamination failure arising in presence of high pressure applied on simple geometry and load cases, by assuming linear elasticity and infinitesimal strain regimes. Although this simplified approach is able to provide an insight on the material parameters governing the mechanical behaviour of bi-layer structures by exploiting sensitivity analyses, the actual behaviour is generally more complex because of large deformations and possible constitutive non-linearities.

In particular, with the aim of determining the role played by both large deformation and non-linear elasticity, some Finite Element (FE)-based numerical simulations have been performed taking also into account the real shape of the food-package. The FE analyses have been all conducted by using the commercial code ANSYS®.

Two sets of numerical simulations have been carried out.

The first set examines three different cases, respectively constituted by the coupling of PP/PET, PP/OPA and PP/PA films involved in the food package. These three non linear FE analyses have been aimed to explore the sensitivity of the stress field in the polymeric layers to the increase of the external pressure under the hypothesis of incompressibility of the packaged water.

The second simulation is a non linear FE analysis performed accounting for both large displacements and non linear stress-strain relationships and it has instead been focused on the sole PET/PP food package, with the scope of finding wrinkling phenomena in the polymeric films as a consequence of severe pressure regimes and bulk deformability of the water.

These numerical results are finally compared with the experimental evidences. In particular the first group of analyses highlight a significant non-linear increase of interfacial shear stresses with the pressure in the case of PET/PP bi-layer film, in accordance with the test results which indicated that this type of coupling was the most prone to delamination failure.

FE analyses of the PP/PET, PP/OPA and PP/PA food packages under increasing pressures

A custom-made ANSYS® environment macro has been developed to perform parametric analyses varying the thicknesses of the two coupled polymeric films, the characteristic sizes describing the overall package shape, the elastic moduli and the non linear stress-strain curves obtained from experiments for each layer. Also the sole

part of the model in the positive eighth has been considered caused by the symmetry of the geometry, boundary conditions and loads (see Figure 4.3, left).

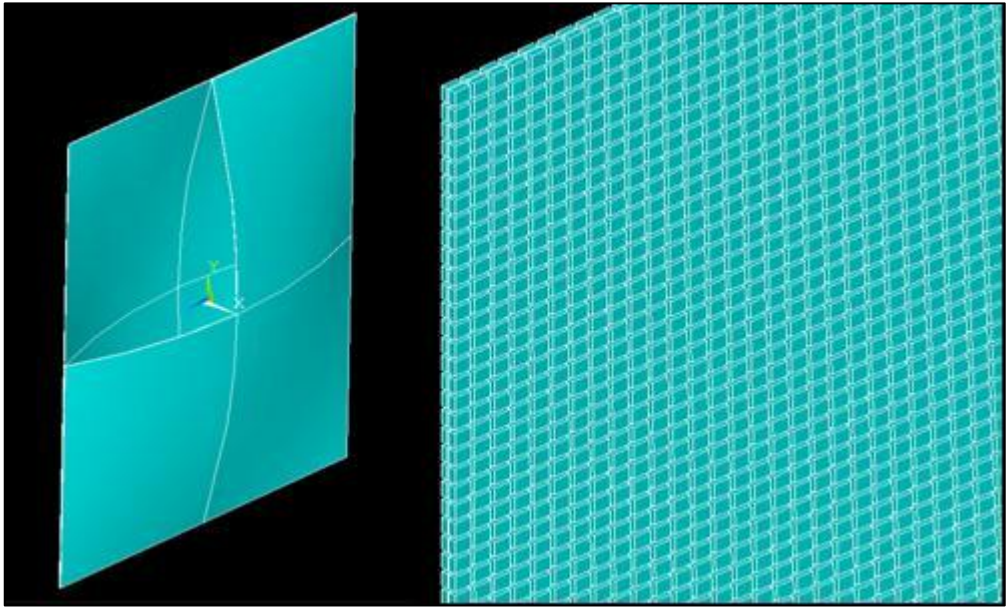


Fig. 4.3. FE computational model: the isometric view of the food package model (*left*) and a detail of the mesh adopted for the two coupled polymeric films (*right*).

In this first group of analyses, achieved in large displacements and strains, the fluid inside the package has been assumed incompressible and the polymeric films isotropic and elastic (see Table 1.). In addition, due to the high geometrical ratio between overall dimension of the object and film thicknesses, the mesh has been generated with a varying number of brick elements (SOLID185, non linear eight nodes element with three degrees of freedom at each node), ranging from 40,000 to about 100,000 elements as a function of the specific case studied. Also, special attention has been also given to the element size ratios and regularity, in order to expect a good result accuracy and avoid numerical errors in terms of energy due to the geometrical distortion of the elements (see Figure 4.3, right). The boundary conditions are established in terms of symmetry constraints applied along the model sides belonging to the three planes defined by the Cartesian reference frame and by means of applied external pressure $p \in [0, 250MPa]$. This three analyses (PP/PET, PP/OPA and PP/PA) have been conducted in large displacements, following the pressure increase by means of a step-by-step procedure. The results are collected in the Figures 4.4, 4.5 and 4.6, where it is highlighted the membranal stress increases within each layer and the interfacial shears.

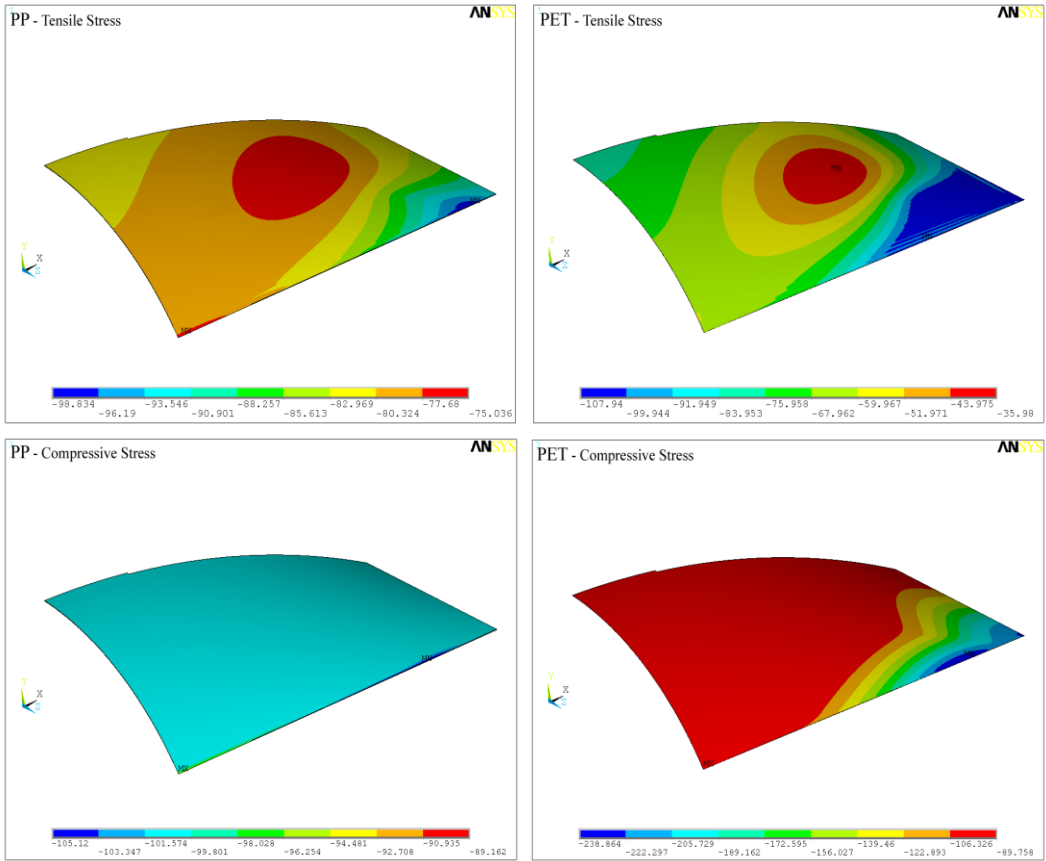


Fig. 4.4. FE analysis of the PP/PET film coupling: comparison between tensile (*top*) and compressive (*bottom*) stresses within PP (*left*) and PET (*right*) polymeric layers.

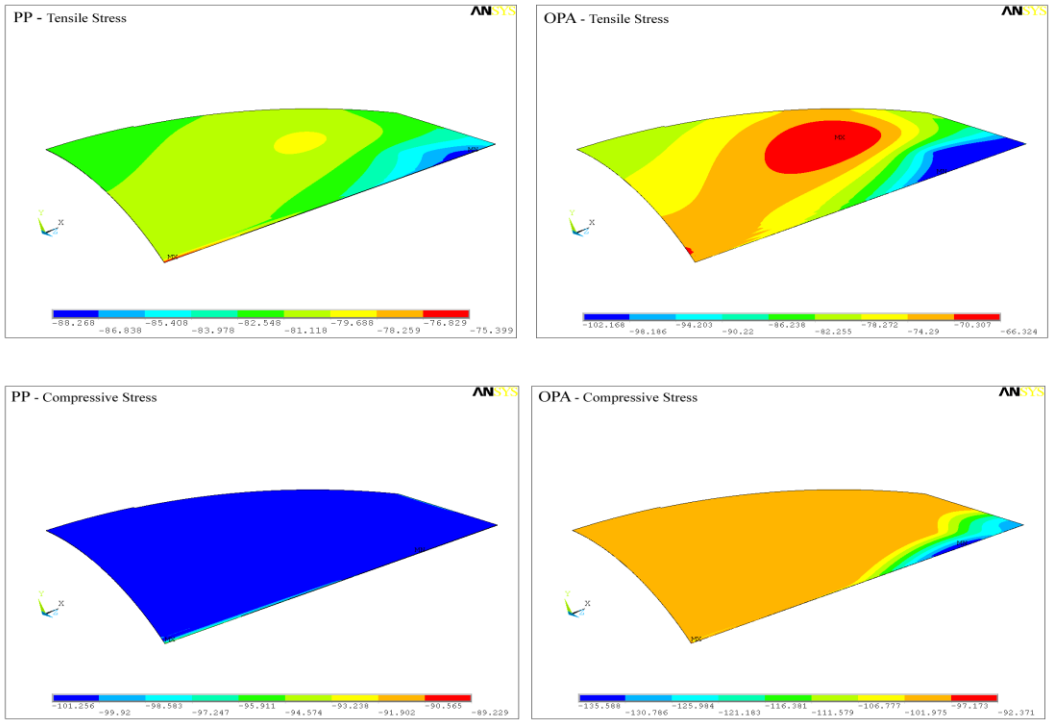


Fig. 4.5. FE analysis of the PP/OPA film coupling: comparison between tensile (*top*) and compressive (*bottom*) stresses within PP (*left*) and OPA (*right*) polymeric layers.

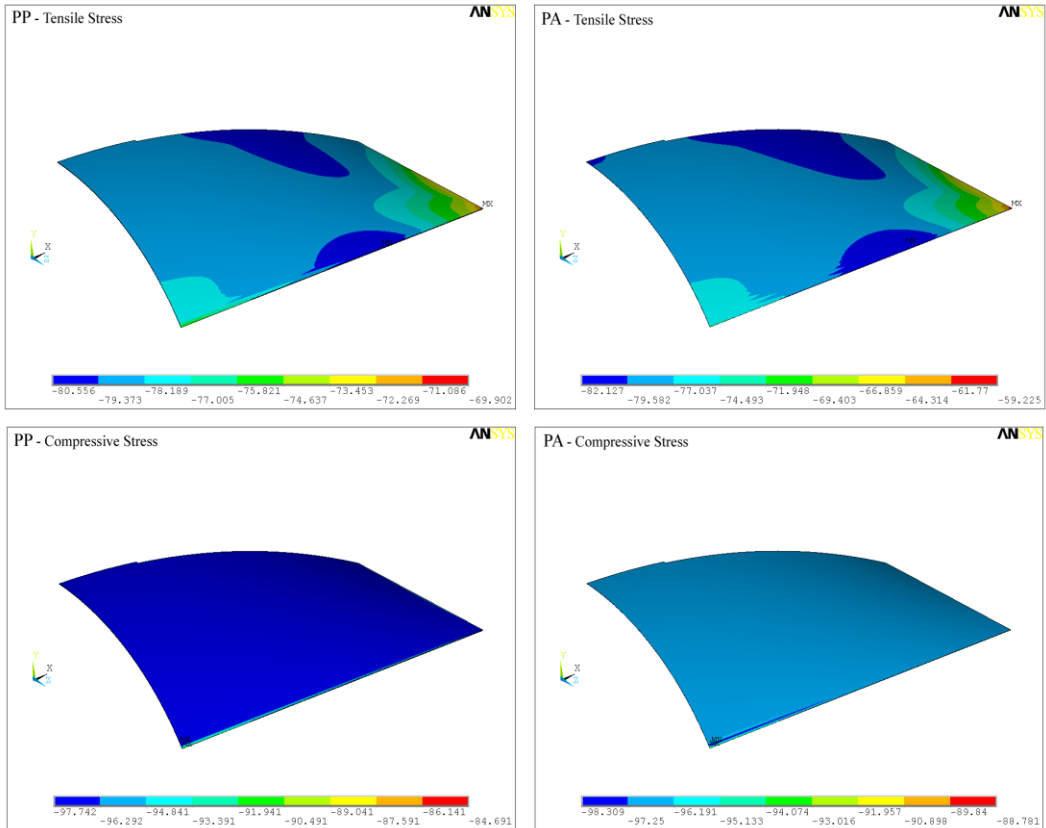


Fig. 4.6. FE analysis of the PP/PA film coupling: comparison between tensile (*top*) and compressive (*bottom*) stresses within PP (*left*) and PA (*right*) polymeric layers.

The numerical results from the FE analyses confirm the experimental evidence on the base of which the PP/PA coupling seems to be the one that minimizes both the peaks of stresses within the films and the interfacial stresses for two different values of the applied pressure (50 and 100 MPa). This is summarized in the histograms reported in the figures 4.7, 4.8 and 4.9, where is clearly shown a significant increase of stress in all the films coupled with the PP layer, with maximum magnitudes in PET, intermediate in OPA and minimum in PA.

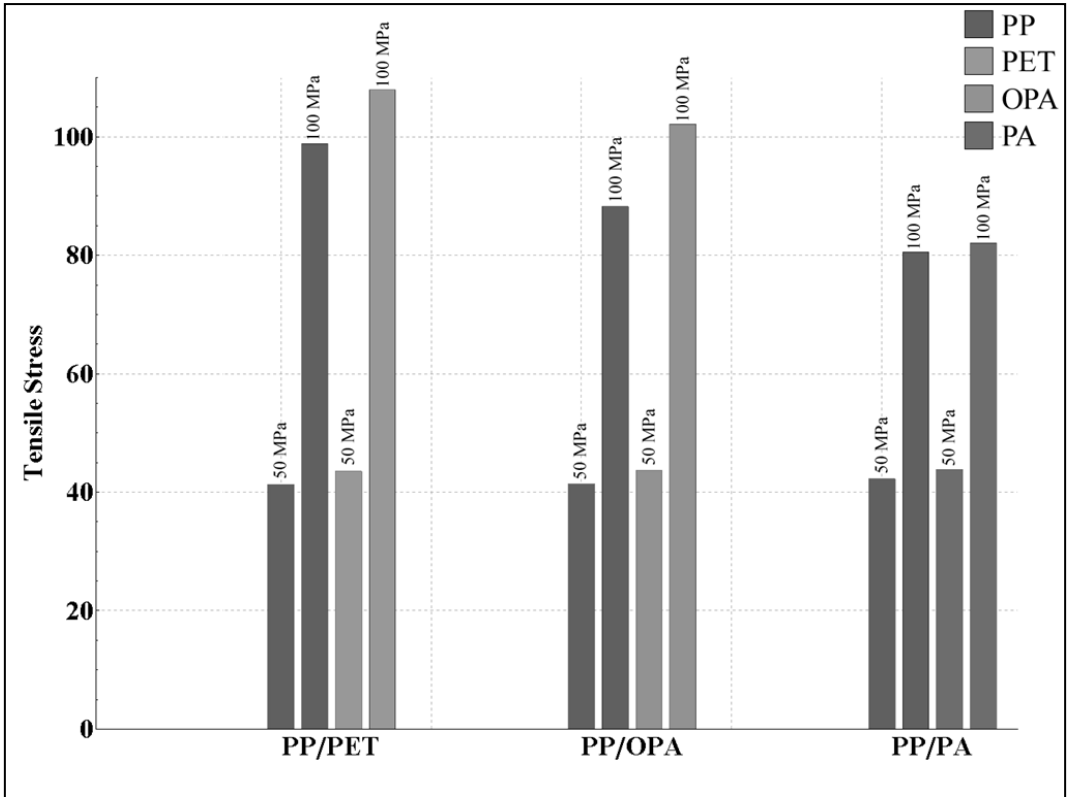


Fig. 4.8. Tensile stresses registered in the three cases analysed: it can be observed that, in the passage from pressures of 50 to 100 MPa, the maximum increase is registered within the PET layer.

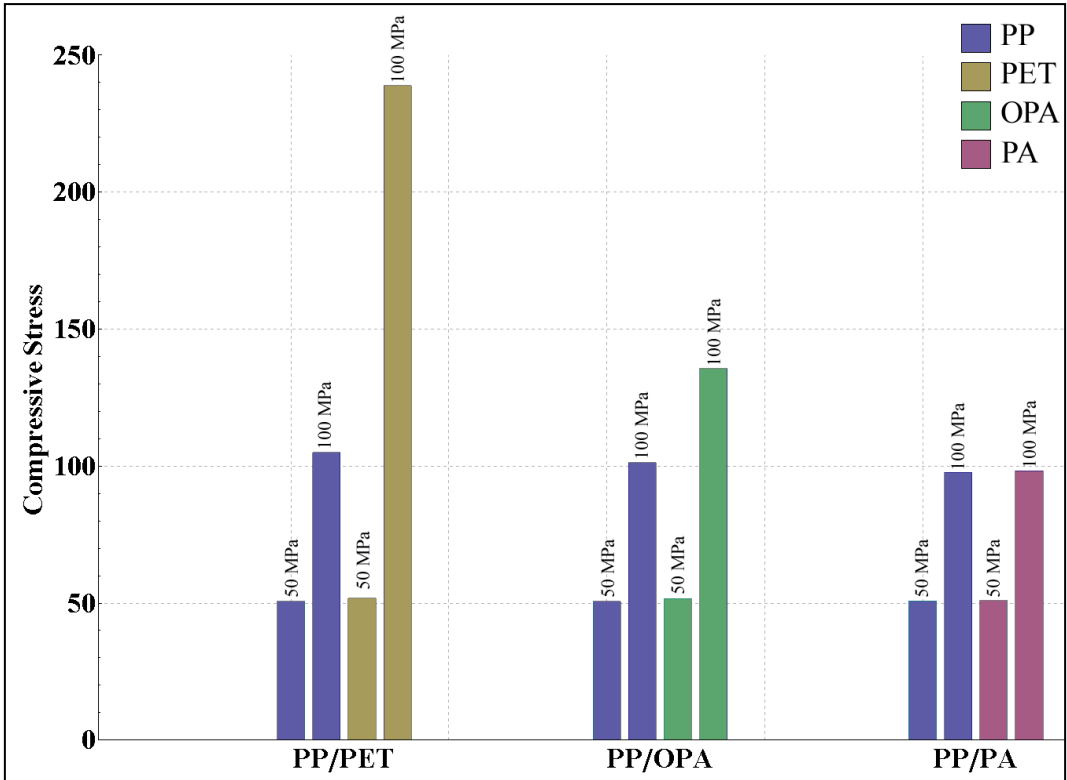


Fig 4.9 Compressive stresses registered in the three cases analysed: it can be observed that, in the passage from pressures of 50 to 100 MPa, the maximum increase is also here registered within the PET layer.

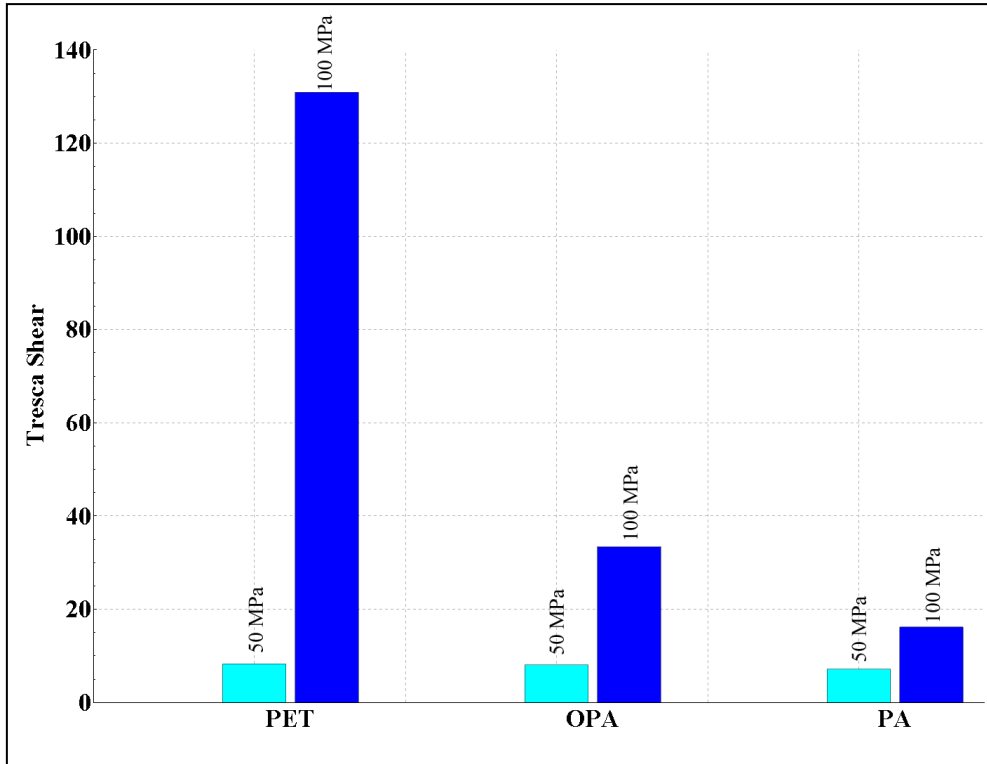


Fig4.10. Tresca stress peaks in the three cases analysed: in the passage from pressures of 50 to 100 MPa a very significant increase of the Tresca stress can be observed within the PET film in the case of PP/PET coupling.

Wrinkling effects and strain gradients in PP/PET food packages under severe pressures

In order to investigate the mechanical response under severe pressures of the food package constituted by PET-PP coupled films – this being the case in which the experiments have shown the most important delamination and interfacial failure phenomena – a specific non-linear FE analysis has been performed. The polymeric layers are modelled as non linearly elastic and the water filled the package is assumed to be compressible and obeying the Tait equation.

A step-by-step procedure controlled by an *ad hoc* arch-length method has been utilized for following the kindle and the evolution of deformation gradients within the polymeric films as a consequence of the pressure increase; the analysis have been conducted in static regime, therefore without considering possible effects due to the time-dependent mechanical response of the materials and, finally, visco-elasticity of the polymeric films, velocity of the increasing pressure, as well as coupling of thermal and fluid-dynamic phenomena have been neglected in the present study.

The results show the stress and strain distribution in the package and highlight two main evidences. The first one is related to the stress concentration phenomena appearing at the boundary of the model, where the films of the opposite sides of the package match. There, it is possible to observe peaks of both shear and maximum tensile stresses and micro-bending deformations in proximity of the object boundary (see Figure 4.11).

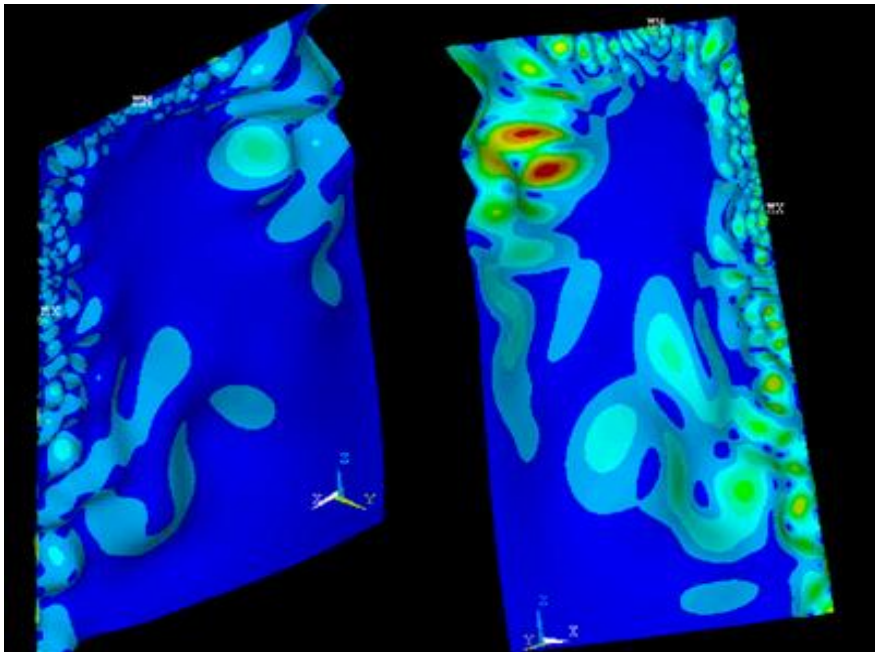


Fig. 4.11. Results of the Finite Element analysis in terms of maximum stresses on the external (*left*) and internal (*right*) layer surfaces. Note the peak of stresses (*red regions*) and the localized micro-bending phenomena in proximity of the object boundary.

The other relevant aspect is exhibited at the interface between the two films, where – due to the presence of significant shear stresses distributed along specific patterns – possible delamination phenomena could start up. Actually, strong deformation gradients seem to appear as localized effects around the welding zones, that is where the opposite sides of the package match (Figure 4.12).

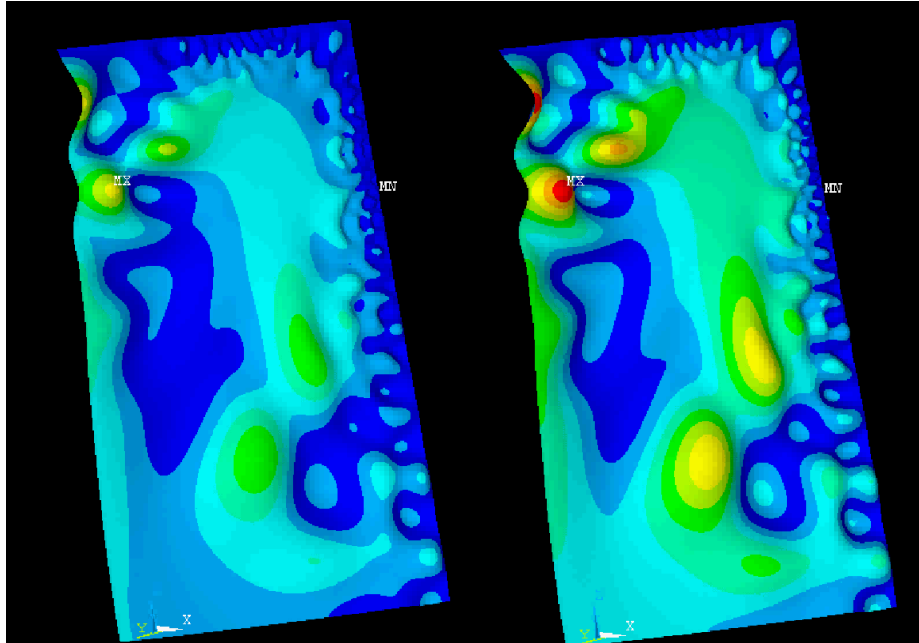


Fig. 4.12 Parallel to the plane of symmetry (left) and total (right) displacements highlighting the deformation gradients around the welding zones.

Conclusion

In the present study, several ways have been followed to approach the problem of analysing the mechanical response of polymeric bi-layer food packages filled with water and subject to high pressures.

Experiments have been made on each constituent film (i.e. PP, PET, OPA and PA) separately – to characterize the single stress-strain behaviours – and on the coupled films, when they have been utilized for building the food packages.

Results from analytical solutions and numerical simulations have all suggested that interlaminar shear stresses grow if the difference in Poisson ratios among the coupled films is significant. In addition, sensitivity analyses have demonstrated that the coupling of PP with too much stiffer polymeric films (PET and OPA) produces an overloading of the material, kindling huge increases in terms of membrane stresses in PET and OPA. Moreover, a *rough* estimate of the goodness of the film coupling has been also proposed

The above mentioned results – obtained by means of theoretical predictions and FE simulations – have substantially confirmed the experimental evidences that highlighted very limited damage phenomena for the PP/PA food packages tested.

Finally, the last non linear FE-based analyses have been focused on the possibility to find – numerically – the strain gradients and wrinkling modes that experiments had

shown in case of PP/PET couplings. This has been actually obtained by means of the last numerical simulations, with surprising similarities in deformation shapes emerging from the comparison between the FE and the laboratory results. Figures 4.13, 4.14 and 4.15 well illustrate this good agreement, showing how the obtained results well fit the appearing of delamination phenomena around the joint regions – that is where the opposite sites of the package match – as well as the regions where localized deformation gradients occur.

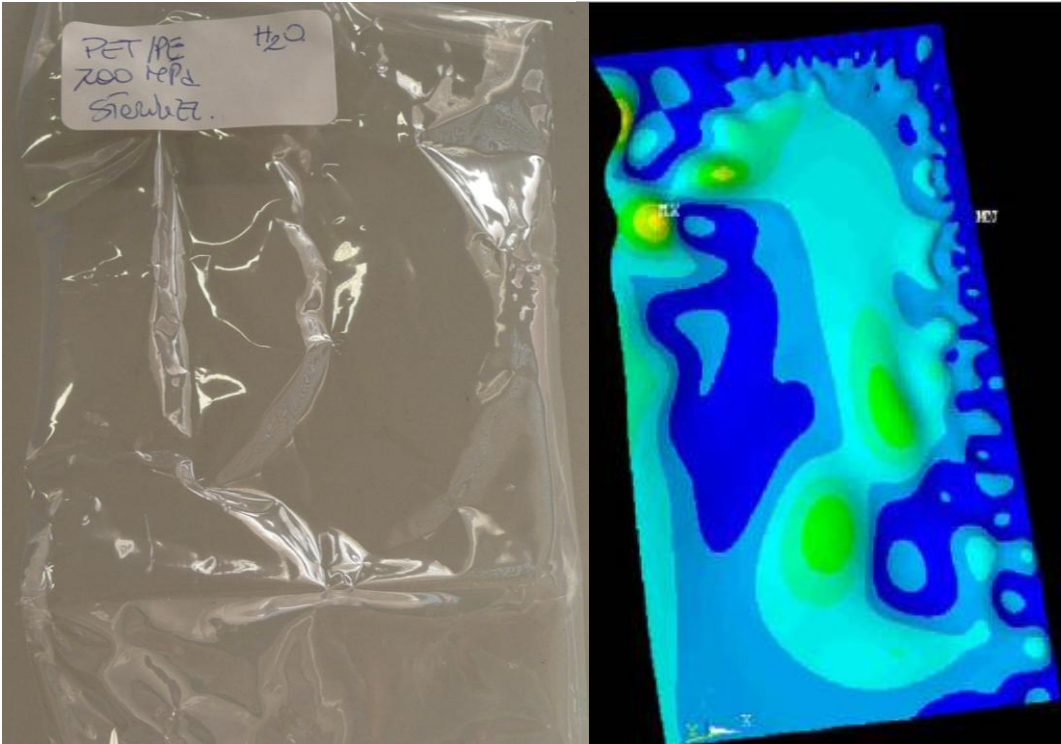


Fig. 4.13: Comparison between experiment and FE analysis: the qualitative distribution of deformation patterns is evident.

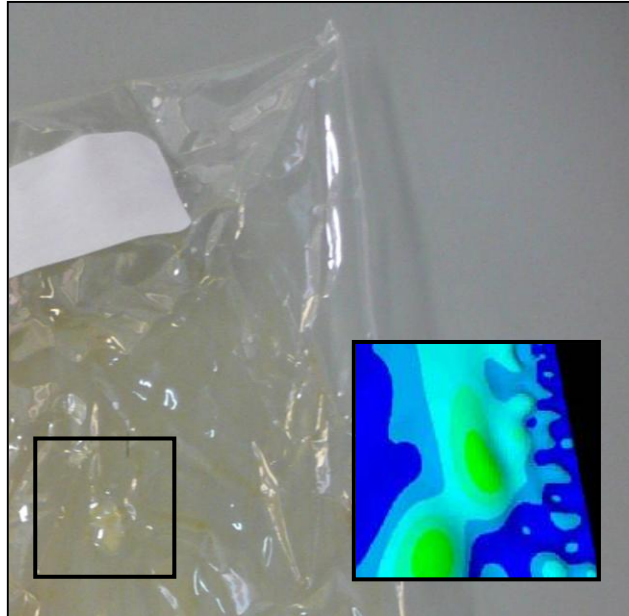


Fig. 4.14. Comparison between experiment and FE analysis: similarity in terms of localized delamination phenomena.

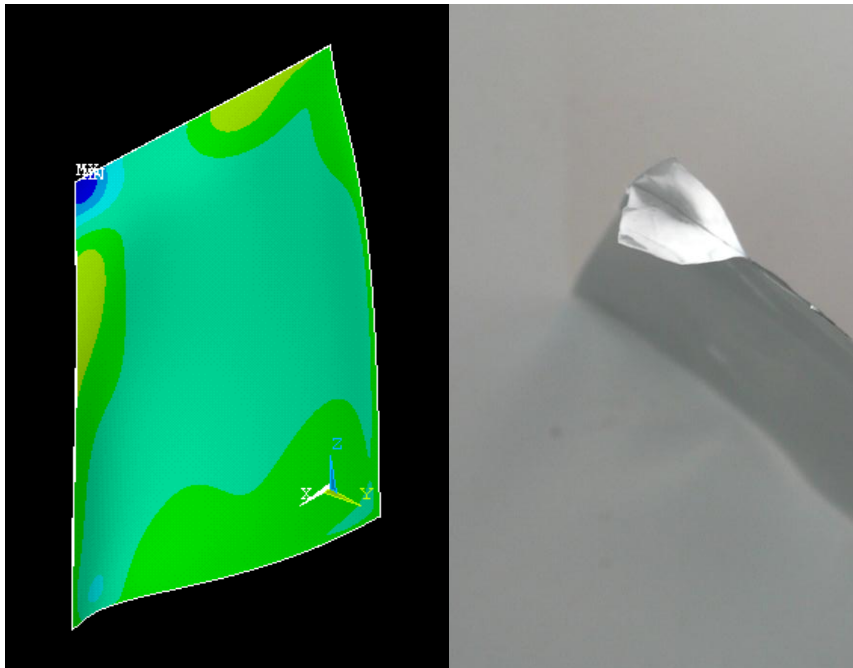


Fig. 4.15. Comparison between experiment and FE analysis: the region in blue (left) predicts high concentrations of interlaminar shear stresses, producing delamination (experiment, right). [Valutare se eliminare questa immagine trattandosi di alluminio...]

Reference

- [1] Alpas, H., Kalchayanand, N., Bozoglu, F., & Ray, B. Interactions of high hydrostatic pressure, pressurization temperature and pH on death and injury of pressure-resistant and pressure-sensitive strains of food-borne pathogens. *International Journal Food Microbiology*, 2000 vol. 60, pages 33–42;

Alpas, H., Kalchayanand, N., Bozoglu, F., Sikes, A., Dunne, C. P., & Ray, B. Variation in resistance to hydrostatic pressure among strains of food-borne pathogens. *Applied and Environmental Microbiology*, 1999 vol. 65, pages 4248–4251]

Baluy R, Heremans K, Masson P (eds). *Colloque INSERM/John Libbery*: London, 1992; pages 469–479;

Deplace G and Mertens B. The commercial application of high pressure technology in food processing industry. In *High Pressure and Biotechnology*,

Farkas D and Hoover GD. High pressure processing: kinetics of microbial inactivation for alternative food processing technologies. *Journal of Food Science (Supplement)* 2000 vol. 65 pages 47–64;

Neil HM. *Food Technol.* 1999; vol 53 (4) pages 86–90;

- [2] Ting E, Balasubramaniam VM and Raghubeer E., *Food Technol.* 2002; 56: 31–35

- [3] Caner C., Hernandez R.J., Pascall., M.A. (2000) Effect of High-pressure Processing on the Permeance of Selected High-barrier Laminated Films, *Pack. Tech. and Sci.* 13, 183-195;

Caner, C., Hernandez, R.J., Harte, B.R. (2004) High-pressure processing effects on the mechanical, barrier and mass transfer properties of food packaging flexible structures: a critical review, *Pack. Tech. and Sci.* 17, 23–29.

- [4] Caroline Morris, Aaron L. Brody and Louise Wicker (2007) *Non-Thermal Food Processing/Preservation Technologies: A Review with Packaging Implications*; *Pack. Tech. and Sci.*, 20, 275-286;

M J Galotto, P. A Ulloa, D. Hernández, F. Fernández-Martín (2008) “Mechanical and Thermal Behaviour of Flexible Food Packaging Polymeric Films Materials

under High Pressure/Temperature Treatments”, , Packaging technology and Science, 21, 297-308R

- [5] Takahashi, M., Shibuya, Y., Numerical analysis of interfacial stress and stress singularity between thin films and substrates, Mechanics Research Communications, 24, 597-602, 1997.
- [6] Bufler, H., The arbitrarily and the periodically laminated elastic hollow sphere: exact solutions and homogenization, Archive of Applied Mechanics, 68, 579-588, 199
- [7] Ding, H. J., Chen, W. Q., Natural Frequencies of an elastic spherically isotropic hollow sphere submerged in a compressible fluid medium, Journal of Sound and Vibration, 192, 173-198, 1996.
- [8] Chen, W. Q., Ding, H. J., Free vibration of multi-layered spherically isotropic hollow spheres, International Journal of Mechanical Sciences, 43, 667-680, 2001.
- [9] Jiang, H., Young, P. G., Dickinson, S. M., Natural frequencies of vibration of layered hollow spheres using exact three-dimensional elasticity equations, Journal of Sound and Vibration, 195, 155-162, 1996.
- [10] Lebon, F., Rizzoni, R., Ronel-Idrissi, S., Asymptotic analysis of some non-linear soft thin layers, Computer and Structures, 82, 1929-1938, 2004.
- [11] Vanimisetti Sampath R., Narasimhan, R., A numerical analysis of spherical indentation response of thin hard films on soft substrates, International Journal of Solids and Structures, 43, 6180-6193, 2006.